UNIVERSITÀ DEGLI STUDI DI PADOVA

DIPARTIMENTO DI INGEGNERIA INDUSTRIALE

TESI DI LAUREA MAGISTRALE IN INGEGNERIA CHIMICA E DEI PROCESSI INDUSTRIALI

Comparative study of the endothermic catalytic reaction of Methane Dry Reforming, in a fixed bed reactor, with microwave heating vs. conventional heating

Relatore:

Chiar.mo Prof. Paolo Canu

Laureando:

Francesco Esposito

ANNO ACCADEMICO 2021/2022

Riassunto

Le reazioni fortemente endotermiche, caratterizzate da valori fortemente positivi di ΔG_R^0, determinati dalla elevata stabilità dei reagenti, richiedono elevati dispendi energetici per poter avvenire, a causa dell'ostacolo posto dalla termodinamica. Tra questi processi si annovera la reazione di Dry Reforming, nella quale il metano è convertito assieme all'Anidride Carbonica a Syngas (una miscela di varie proporzioni di Idrogeno e Monossido di Carbonio), mediante un processo catalitico che si svolge a temperature di 800-1100°C. L'elevata temperatura richiesta per l'attivazione di questo processo è tipicamente ottenuta in fornaci dalla combustione di combustibili fossili; questa modalità di riscaldamento sfutta i fenomeni di conduzione e convezione per trasferire calore al letto catalitico. Ciò comporta, tuttavia, la formazione di inevitabili gradienti termici tra la parete ed il centro del letto catalitico (che riducono l'efficienza del processo), oltre che all'emissione di gas serra generati dalla combustione di carburanti fossili. Lo scopo del lavoro sviluppato in questa tesi è focalizzato sull'investigazione di un metodo alternativo di riscaldamento, che sfrutta l'irraggiamento mediante microonde per riscaldare il letto catalitico e permettere quindi l'attivazione della reazione. Per raggiungere questo scopo, è stato modificato un forno a microonde domestico di fascia medio-bassa. La tecnologia del riscaldamento a microonde è ampiamente diffusa nell'ambito domestico, ed i suoi molteplici vantaggi sono noti da tempo alla comunità scientifica; la stessa diffusione non è stata però raggiunta a livello industriale, a causa di problematiche non secondarie nell'implementazione di questa tecnologia, tra le quali assume un ruolo prominente il controllo termico del letto.

La campagna sperimentale volta all'investigazione della reale efficacia del riscaldamento a microonde è consistita in due parti principali. Durante la prima fase, il problema del controllo termico è affrontato, investigando tre possibili soluzioni; l'utilizzo di pirometri ad infrarosso, di termometri ad aria, e di comuni termocoppie metalliche. L'ultima soluzione si è rivelata migliore, pur richiedendo alcune accortezze volte a preservare l'integrità della sonda immersa nella cavità del forno a microonde. Una volta definita la strategia di controllo termico, è stato possibile avviare la seconda fase della campagna sperimentale, inerente la costruzione del setup sperimentale e la valutazione delle performances del riscaldamento a microonde, comparando i risultati ottenuti con il metodo di riscaldamento convenzionale. Questo ha permesso di determinare la fattibilità del riscaldamento a microonde applicato a reazioni catalitiche gas-solido endotermiche.

Abstract

Highly endothermic reactions, characterized by highly positive values of ΔG_R^0 determined by the stability of reactants, are very energy intensive processes due to the obstacle posed by thermodynamic features of the reacting system. Among these processes there's the reaction of methane reforming, where methane is converted into syngas (a mixture of Hydrogen and Carbon Monoxide) through a catalytic process operated at temperatures ranging from 800 to 1100°C. High temperature required for activation of the reaction are usually obtained in furnaces, through combustion of fossil fuels; this heating strategy exploit both conduction and convection for transferring heat to the catalyst. However, this imply the presence of unavoidable temperature gradients between the walls and bed (which reduces the process efficiency), and the emission of greenhouse gasses due to the combustion process. This thesis work aim to investigate alternative heating strategies, exploiting radiation through microwaves, to heat the catalyst and therefore activate the reaction. Microwaves were generated by a common household microwave oven, which was modified and characterized in previous thesis works. Microwave heating is nowadays a very diffuse technology in domestic contexts, and its advantages are well known by the scientific community; the same diffusion is not achieved, however, in industrial contexts, due to various problems which has still to be solved, among which thermal control of the system is a primary obstacle.

The experimental campaign performed, required to investigate the real efficiency of microwave heating, was divided in three main sections. First, the problem of temperature control was addressed, by investigating features of three different solutions; an infrared pyrometer, an air thermometer and, finally, thermocouples. The last control strategy turned out to be more efficient, even if particular cautions were required to make it properly work, due to the presence of metallic components immersed in the electromagnetic field. Then, the second part of the work was focused on the evaluation of the system's performances, and on the comparison of these performances with those obtained with conventional heating systems. This work was used to determine the feasibility of microwave heating applied to endothermic gas-solid chemical processes.

Contents

List of Figures . . . . . **vii**

List of Tables . . . . . **ix**

List of Symbols . . . . . **x**

Introduction **1**

1 State of the art of microwave heating **5**
1.1 Microwave heating 7
1.1.1 Microwaves in the EM spectrum 7
1.1.2 History 8
1.1.3 Microwave generators 8
1.1.4 Microwave oven applicators 11
1.1.5 Microwave-material interactions 12
1.1.6 MW effects on reacting systems 14
1.1.7 Mathematical description of dielectric properties 15
1.1.8 Frequency and Temperature dependence 18
1.1.9 Penetration Depth 19
1.1.10 Temperature measurements during Microwave processing: the significance of thermocouple effects [47] 21
1.2 Literature survey on Syngas catalytic production via Methane Dry reforming with Microwaves 23
1.2.1 Thermodynamic equilibrium framework 23
1.2.2 J. Chaouki, S. Hamzehlouia, S.A. Jaffer [23] 24
1.2.3 B. Fidalgo, A. Domìnigues, J.J. Pis, J.A. Menéndez [19] . . . 27
1.2.4 X. Zhang, C.S.M. Lee, D.M.P. Mingos, D.O. Hayward, [64] . . 29
1.2.5 A. Ramirez, J.L. Hueso, M. Abian, M.U. Alzueta, R. Mallada, J. Santamaria [49] 31
1.2.6 K. Sato, H. Luo, M. Miyakawa, M. Nishioka [50] 33
1.2.7 S. Sharifvaghefi, B. Shirani, M. Eic, Y. Zheng [51] 36
1.2.8 I. de Dios Garcìa, A. Stankiewicz, H. Nigar [14] 39
1.3 Literature survey on Syngas catalytic production via Methane Steam reforming with Microwaves 42
1.3.1 D. Czylkowski, B. Hrycak, M. Jasinki, M. Dors, J. Mizeraczyk [13] 42
1.3.2 N.M. Alawy, G.H. Pham, A. Barifcani, M.H. Nguyen, S.Liu [4] 44

2 Materials and Methods 46
2.1 Feed section 47
2.1.1 Mass flow meters 47
2.1.2 Pressure trasducer 48
2.2 Reaction section 49
2.2.1 Vibratory sieve shaker 49
2.2.2 Reactor and Fittings 50
2.2.3 Microwave heating system 52
2.2.4 Conventional heating system 54
2.3 Measurement section 55
2.3.1 Gas Chromatograph 56
2.3.2 FTIR Spectrometer 58
2.3.3 Condenser 59
2.3.4 Wattmeter 59
2.3.5 Air thermometer 60
2.3.6 Thermocouples 61
2.3.7 Radiation Pyrometer 62
2.4 Programs 63

3 Experimental Results 64
3.1 Temperature measurement 64
3.1.1 Air thermometer 64
3.1.2 Non-contact methods 75
3.1.3 Thermocouples 78
3.2 Experimental setup 88
3.2.1 Thermocouple diameter 88
3.2.2 Particle size 91
3.2.3 Catalyst loading 93
3.2.4 Temperature distribution in the bed 95
3.2.5 Power drops on the electric line 98
3.2.6 Position of the catalytic bed in the cavity 99
3.2.7 Gas Hourly Space Velocity (GHSV) 99
3.3 Comparative study of Methane Dry reforming 100
3.3.1 Thermodynamic equilibrium study 100
3.3.2 Temperature policy 104
3.3.3 Comparison of MDR by heating technologies 106

Conclusions 118

List of Figures

1 Set of products that can be obtained from Syngas [34]. 2

1.1 Difference between MW (left) and conventional (right) heating [44]. . 6
1.2 The Electromagnetic spectrum [21] 8
1.3 Typical aspect of a continuous wave magnetron (a), and a schematic cross-sectional view of the magnetron cavity [21] 9
1.4 Schematic view of a high-power klystron [38] 10
1.5 Representation of the EM field distribution in single-mode and multimode applicators [26]. 12
1.6 Different polarization mechanisms [21]. 14
1.7 Loss angle representation on the $(\varepsilon'_r, \varepsilon''_r)$ plane [26]. 17
1.8 Complex permittivity and loss factor of various powders [26]. 17
1.9 Effect of temperature and frequency on dielectric properties of $\beta-SiC$ having particle size of 530 nm [56]. 19
1.10 Comparison of T measurement techniques during MW processing [47]. 21
1.11 Contour lines of the EM field nearby the thermocouple tip (left) and calculated relative absorbed power density along the axial direction of the thermocouple, from the tip to the sample boundary [47]. 22
1.12 Equilibrium compositions of all the species, included solid carbon [23]. 24
1.13 Experimental setup for the MW heating fluidized bed reactor.[23]. . 25
1.14 Temperature profiles of the solid catalyst surface, bed bulk and gas under MW heating [23]. 26
1.15 Selectivity of Syngas products plotted vs reactant conversions, parametric in temperature [23]. 27
1.16 Schematic diagram of the experimental setup [19]. 28
1.17 Effect of heating mode on the MDR reaction. Labels as in table 1.4[19]. 28
1.18 Conversions of Carbon Dioxide (left) and Methane (right) at different temperatures for MW heating, conventional heating and the theoretical thermodynamic value, for the catalytic system $Pt(8\%)/CeO_2(20\%)/\gamma-Al_2O_3$[64]. 30
1.19 Selectivity as H_2/CO ratio over temperature, for the catalytic system $Pt(8\%)/CeO_2(20\%)/\gamma - Al_2O_3$ [64]. 31
1.20 Input, absorbed and reflected power as function of temperature [64]. . 31
1.21 Influence of contact times on the Isobutane CODH reaction under conventional (left) and MW (right) heating. [49]. 32

1.22 Comparative catalytic performance in isobutane CODH: (A, B) selectivity o products and isobutane conversion (solid green dot) at 625°C and 675°C; (C) selectivity-conversion plots (dashed lines represents equal yields); (D) evaluation of selectivity to isobutylene at different temperatures for equivalent conversion levels of isobutane. [49]. . . . 33
1.23 Schematic diagram of the MW reactor system. 34
1.24 Comparison between components concentrations as function of temperature for MW-assisted Methane Steam reforming (left) and conventional heating (right) [50]. 35
1.25 Comparison between components concentrations as function of temperature for MW-assisted Methane Dry reforming (left) and conventional heating (right) [50]. 35
1.26 Thermo-gravimteric analysis of the catalyst used in the study [50]. . . 36
1.27 Schematic representation of both MW (**a**) and conventional (**b**) heating systems. [51]. 36
1.28 Performance of different catalytic systems in terms of CH4 conversion (left) and CO2 conversion (right) [51]. 37
1.29 Performance of different catalytic systems in terms of H_2/CO ratio [51]. 38
1.31 Performances of conventional and microwave heating, for different catalytic systems, in terms of reactor energy efficiency and reactant conversions [51]. 38
1.30 Comparison between conventional heating, microwave heating and equilibrium conditions for (a) methane conversion, (b) CO_2 conversion and (c) H_2/CO ratio. [51]. 39
1.32 Catalytic performance of Ni/SiC at 800°C in terms of CH_4 and CO_2 conversions (left), H_2/CO product ratio and power consumption (right) for the MDR process [14]. 40
1.33 Influence of the ratios of CO_2/CH_4 in the conversions of CH_4, CO_2 (left) and supplied microwave power input and H2/CO ratio (right) [14]. 41
1.34 Influence of the space velocity on the conversion of CH_4 (left) and CO_2 (right). [14]. 41
1.35 Scheme of the experimental setup used by the authors [13]. 42
1.36 Influence of the absorbed MW power (up) and CO_2 flowrate (down) in the H_2 production flowrate and energy yield (left), and CH_4 conversion and concentration H_2 (right). [13]. 43
1.37 Effect of the inlet steam concentration on the Methane conversion (a), Selectivity to H_2 and CO (b), Yield to H_2 and CO (c) and on the H_2/CO ratio (d) [4]. 44
1.38 Effect of the total feed flowrate on (a) Conversion of CH_4, CO_2, (b) Selectivity of the process to H_2 and CO [4]. 45
1.39 Effect of the total feed flowrate on (c) Yields of Hydrogen and CO, (d) H_2/CO ratio [4]. 45

2.1 Schematic representation of the experimental setup. 46
2.2 Bronkhorst mass flow meter. 48

2.3 Honeywell Pressure Trasducer MPX5500DP and its scheme. 49
2.4 Vibratory sieve shaker used for sieving the grind SiC and Catalyst. . 50
2.5 Fittings used to prevent leakages from the reactor 50
2.6 Reactor used for the reaction. A type K thermocopule control the bed temperature. 51
2.7 Internal components of the Microwave oven. 52
2.8 Setup of the Microwave heating reaction system. 53
2.9 Scheme of the experimental setup of the MW oven; (left) front view, (right) top view. 54
2.10 Electrically heated oven. 55
2.11 Configuration of the GC. 56
2.12 Gas chromatograph used to analyse the gaseous mixture. 57
2.13 IRTracer-100. 58
2.14 Condenser (right) and its internal structure (left) [35]. 59
2.15 Technical drawing of the air thermometer [43]. 60
2.16 Calibration of the air thermometer performed in previous thesis works [43]. 61
2.17 Electric circuit of a thermocouple [**?**]. 61
2.18 Types of thermocouples, depending on the relative position of hot junction and sheath: (top) exposed, (centre) insulated and (bottom) grounded. 62
2.19 The radiation pyrometer. 63

3.1 Schematic diagram of the temperature calibration. 66
3.2 Schematic diagram of the pressure calibrations. 66
3.3 Calibrations of the air thermometer. Red line is referred to the temperature calibration; the blue line refer to the pressure calibration. 67
3.4 Test performed to check the air temperature calibration. 68
3.5 Temperature profiles of the type-k thermocouple (yellow line), the pressure-calibrated thermometer (blue line) and the temperature-calibrated thermometer (red line). 68
3.6 Temperatures of the thermocouple (blue line) and thermometer (red line) vs time at different immersion depths. Thermometer immersed for 1/4 (**A**), 1/2 (**B**), 3/4 (**C**), 3/4 with insulation (**D**). 70
3.7 Errors between the two temperature probes vs time at different immersion depths. Thermometer immersed for 1/4 (**A**), 1/2 (**B**), 3/4 (**C**), 3/4 with insulation (**D**) 71
3.8 Temperature profiles of the type-k thermocouple and the temperature-calibrated thermometer. Heating rates of 10°C/min (left) and 25°C/min (right). 72
3.9 Scheme of the test used to determine the influence of heating rates. . 72
3.10 Temperature profiles of the thermocouple and air thermometer. . . . 73
3.11 Melted probe; In the points where glass melted, SiC granules were included in the structure.. 73
3.12 Scheme of the test used to compare the temperature measured by the air thermometer and the metallic thermocouple. 74

3.13 Temperature profiles of the air thermometer and the metallic thermocouple (top). Zoom of the air thermometer's temperature profile (bottom). 74
3.14 IR reflectance spectrum of Quartz. 76
3.15 Spectral emissive Power of a black body. 76
3.16 Schematic diagram of temperature measurement arrangement using the IR pyrometer. 77
3.17 Structure of a FO temperature sensor. 78
3.18 Scheme of the test with a metallic and a ceramic thermocouple. . . . 80
3.19 Results of the test with two thermocouples of different sheath materials. 81
3.20 Scheme of the forces acting on electrons (red dots) on flat (top) and curved (bottom) surfaces. 82
3.21 Behaviour of dielectric properties (top) and Penetration depth (bottom) for SiC as function of temperature. Data from *Sugawara et al.* [56] 83
3.22 Calculated attenuation factor for SiC as function of temperature. . . 84
3.23 Normalised electric field intensity for various temperatures, obtained from the fitting procedure. 85
3.24 Scheme of the test. 85
3.25 Results of the test. 87
3.26 Scheme of the test, with three thermocouples located at 2, 4, 8 cm from the cavity bottom. 88
3.27 Result of the two tests performed with type-K thermocouples with 1/16 in diameter. 89
3.28 Result of the two tests performed with type-K thermocouples with 1/8 in diameter. 90
3.29 Scheme of the test performed to determine influence of the SiC granulometric class. 91
3.30 Temperature profiles of the tests performed with SiC of granulometric class of 1 mm (left) and 0.1 mm (right) 92
3.31 Temperature profiles of the tests performed with SiC of granulometric class of 1 mm (left) and 0.1 mm (right), with metallic and ceramic thermocouples. 93
3.32 Scheme of the test used to determine the relation between catalyst loading and voltage. 94
3.33 Relation between catalyst loading and voltage recorded by the multimeter (left); total catalyst mass is 1.61 g. Relation between catalyst mass and voltage (right). 95
3.34 Temperature profiles of test #2. 97
3.35 Temperature profiles of test #3. 97
3.36 Temperature differences between the controlling thermocouple and the other two. 97
3.37 Temperature profiles of the test at 700°C for 2 hours (top); temperature differences between the controlling thermocouple (middle) and the other two. 98
3.38 Relative position of the catalytic bed and waveguide. 99

3.39 Comparison between equilibrium calculations of different software and different conditions. 102
3.40 Comparison between equilibrium calculations from literature ([41], left) and the one calculated for this thesis work (right). The equilibrium composition includes all the species, including water and solid Carbon. 102
3.41 Equilibrium compositions of all the gaseous non-condensible species. . 103
3.42 Equilibrium conversion of Methane and Carbon Dioxide. 103
3.43 Number of moles of the gas and solid phases as function of temperature. The initial number of moles is reported as dashed line.. 104
3.44 Temperature policy of the test under MW heating. 105
3.45 Zoom of the 900°C isotherm. 105
3.46 Temperature policy of the test under Conventional heating. 106
3.47 Gas-phase compositions as a function of temperature. 107
3.48 Condensed water at the oven outlet in the MW heating system. . . . 108
3.49 Time profiles of the dry gas from the reactor in the MW heating system. 108
3.50 Time profiles of the dry gas from the reactor in the Conventional heating system. 109
3.51 Conversions of reactants: CH_4 on the right, CO_2 on the left. 109
3.52 Selectivity of Hydrogen and Carbon Monoxide with respect to different reactants. 110
3.53 Selectivity-Conversion plot. 110
3.54 Ratio of Hydrogen to Carbon Monoxide at different temperatures, for both heating systems. 111
3.55 Time profiles of CO, CO_1 for the TPO tests for both heating systems (top: conventional heating test; bottom: microwave heating test). . . 112
3.56 Error on Carbon as function of temperature. 114
3.57 Typical profile of pressure drops for both heating systems. 115
3.58 Instantaneous power and cumulated energy profiles of both tests. . . 116
3.59 Relation between magnetron temperature and instantaneous power. . 117

List of Tables

1.1 List of dielectric properties for common materials 18
1.2 Reaction mechanism for Dry reforming of methane suggested in [41]. . 24
1.3 Terms of the energy balance [23]. 26
1.4 Conditions of the experimental campaign [19]. 29
1.5 Conditions of the experimental campaign [64]. 29
1.6 Conditions of the experimental campaign. 34

2.1 Composition of the feed mixture used in the experiments. 47
2.2 Operating parameters for the gas feed used in both tests. 47
2.3 Composition of the JM's catalyst Katalco 25-4™ 51
2.4 Characteristic of the components used in the oven. 53
2.5 MW oven dimensions and lengths. 54
2.6 Watlow heater characteristics. 55
2.7 Thermal conductivity of gasses involved in the separation [36]. . . . 56
2.8 Method developed for the GC analysis. 57
2.9 Wavenumbers for CO and CO_2. 59
2.10 Volumes of the air thermometer. 60
2.11 Programs used to monitor the variables of interest 63

3.1 Thermal conductivities of some materials. 71
3.2 Skin depth of some metallic materials [48]. 80
3.3 Evolution of the EM field with depth 83
3.4 Comparison of the calculated and measured temperature of the thermocouple inside the bed. 86
3.5 Features of the tests where three thermocouples were immersed in the SiC bed. Granulometric class of SiC used is >1 mm. 90
3.6 Voltage recorded at various catalyst loadings. 94
3.7 Conditions of the tests; the controlling thermocouple is highlighted in bold character. The bed is composed of only SiC. 96
3.8 Conditions used to determine the equilibrium concentration with *NASA-CEA* and *Cantera*. Cut-off species concentration is only present in *NASA-CEA*. 101
3.9 Conditions of the equilibrium calculations with *NASA-CEA*. 101
3.10 Isotherm durations for the test under MW heating. 105
3.11 Isotherm durations for the test under conventional heating. 106
3.12 Operating parameters used in both tests. 107
3.13 Operating parameters used for both TPO. 112
3.14 Total amount of carbon, as determined by the TPO. 113

3.15 Total amount of carbon, scaled on test duration and catalyst mass. . 113
3.16 Comparison of Carbon deposited from the TPO and from the Error balances, for both heating systems. Results expressed in mg. 114
3.17 Power required by both heating systems. 115
3.18 Power required by the accessory components of the MW oven. 115

List of Symbols and Acronyms

Greek letters	**Meaning**
α	Attenuation factor
β	Phase factor
δ	Loss angle
ε	Dielectric permittivity
ε_0	Free space permittivity ($\varepsilon_0 = 8.854 \times 10^{-12}\ F/m$)
ε^*	Relative complex dielectric permittivity ($\varepsilon^* = \varepsilon' - j\varepsilon''$)
$\varepsilon',\ \varepsilon'_r$	Real part of complex dielectric permittivity (dielectric constant)
$\varepsilon''_d,\ \varepsilon''_e,\ \varepsilon''_a,\ \varepsilon''_{MW}$	Dipolar, electronic, atomic, and Maxwell-Wagner loss factors
ε''_{eff}	Loss factor (imaginary part of complex dielectric permittivity)
λ'_0	Wavelength in free space
μ	Magnetic permeability (or viscosity)
μ^*	Complex magnetic permeability ($\mu^* = \mu' - j\mu''$)
μ'	Real part of complex magnetic permeability
μ''	Imaginary part of complex dielectric permeability
ρ	Charge density (or density)
σ	Electric conductivity (or hoop tensile strength)
ω	Angular frequency ($\omega = 2\pi f$)
ω_i	Mass fraction of component i ($\omega_i = m_i/m_{tot}$)
Latin letters	**Meaning**
$\boldsymbol{B}$	Magnetic induction field
Bou	Boudouard reaction
C_1	First Plank's constant ($C_1 = 3.742 \cdot 10^8\ \mu m^4 \cdot W \cdot m^-2$)
C_2	Second Plank's constant ($C_2 = 1.439 \cdot 10^4\ \mu m \cdot W$)
$\boldsymbol{D}$	Electric displacement field
$D_{1/2}$	Half power density depth
d_p	Particle diameter
D_p	Penetration depth
$\boldsymbol{E}$	Electric field
EOS	Equation of state
EM	Electro-magnetic
f	Frequency
GC	Gas Chromatograph
GHSV	Gas Hourly Space Velocity
$\boldsymbol{H}$	Magnetic field
IR	Infrared radiation
j	Imaginary unit ($j = \sqrt{-1}$)
$\boldsymbol{J}$	Vector current density
k_e	Couloumb's constant ($k_e = 8.98 \cdot 10^{-9}\ N \cdot m^2 \cdot C^{-2}$)
L	Spectral emissive power
MC	Methane cracking
MDR	Methane Dry reforming

Latin letters	**Meaning**
MSR	Methane-Steam reforming
MW	Microwave
P	Power
PI	Process Intensification
RWGS	Reverse Water-gas shift
RM	Reverse methanation
SiC	Silicon Carbide
$\tan(\delta)$	Loss tangent ($\tan(\delta) = \varepsilon''_{eff}/\varepsilon'$)
T	Temperature
TPO	Temperature Programmed Oxidation
TPR	Temperature Programmed Reduction
WGS	Water-Gas shift
W	Watt

Introduction

Sustainability is nowadays a central topic in all fields of human development. In 1987 the UN Commission on Environment and Development defined *sustainable development* as "meeting the needs of the present without compromising the ability of future generation to meet their own needs" [10]. Since then governments, NGOs, industry, and society, have considered how to best achieve it from their own standpoints. To the chemical and process industry it is demanded to produce increasingly larger quantities of chemical products, as to satisfy the needs of a growing population, while reducing its environmental impact and resource consumption. Clearly, this fact posed huge challenges, related to the optimization of existing processes; however, it also gave it new stimuli, which led to the definition of a new field of sustainable industrial practices, collectively known as Green Chemistry and defined by a set of 12 principles. In particular, the sixth principle focus on energy consumption; "Energy requirements of chemical processes should be recognised for their environmental and economic impacts, and should be minimized" [11]. Strategies through which energy minimization is implemented are defined by the emerging field of Process Intensification (PI), one of the most promising development paths for chemical process industries [37]. PI aim to drastically improve equipment and process efficiency by improvements in four different fields; the spatial, thermodynamic, functional, and temporal ones. Of particular interest is the thermodynamic domain; to minimize energy wastes, energy should be transferred in the right form, in the required amount, at the required moment, and at the required position. Fulfilment of these requirements assures that energy consumption is optimized [58]. This concept of PI is particularly important when highly energy-intensive processes are considered; in the chemical industry, those typically involve highly endothermic reactions, where high temperatures are required to activate the reaction. One of such processes is Methane Dry Reforming (MDR), where Methane and Carbon Dioxide reacts on a suitable catalyst at 800-1100°C to produce Syngas (synthesis gas, a mixture of Hydrogen and Carbon Monoxide in various proportions), in a complex mechanism involving several reactions. Methane dry reforming reaction can be written as

$$CH_4 + CO_2 \leftrightarrows 2CO + 2H_2 \qquad \Delta H_R^0 = 247.3\ kJ/mol \tag{1}$$

Syngas has particular relevance in the chemical industry, not only because of its direct applications (as fuel, reducing agent, building block for more complex molecules like hydrocarbons, methanol, etc., as shown in figure 1), but also because it is suitable for the development of an Hydrogen-based economy, being the precursor of methanol, a chemical platform species from which many different chemicals can be

obtained. The dry reforming reaction use as feedstock chemicals two of the most diffuse greenhouse gasses, converting them into high value-added chemicals.

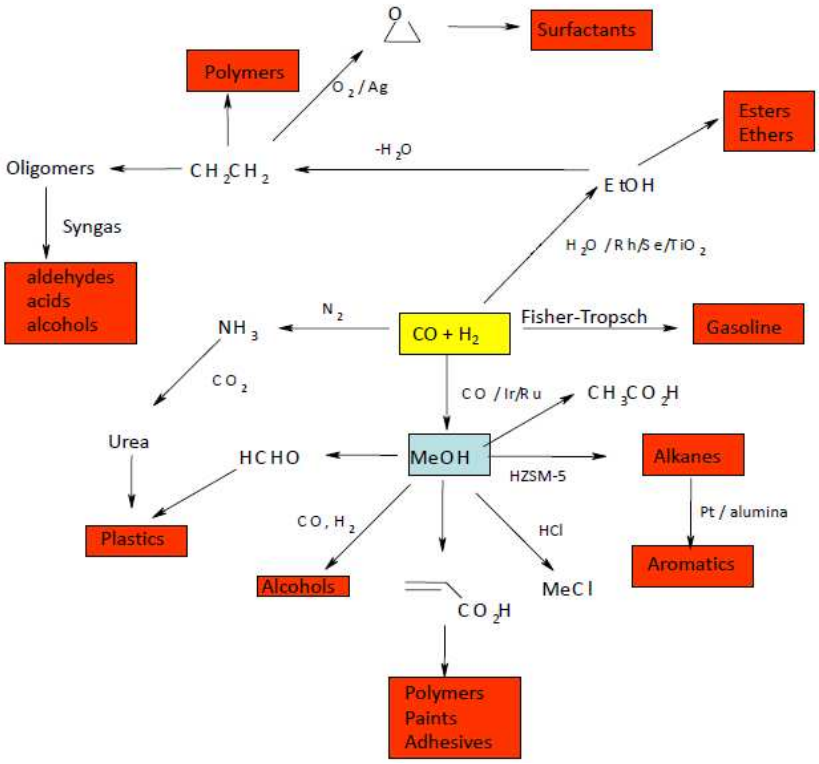

Figure 1: Set of products that can be obtained from Syngas [34].

In addition this technology, if correctly implemented, would offer a convenient way to convert a low energy density fuel like methane, into liquid products such as longer chain hydrocarbons via the Fischer-Tropsch process, characterized by a much higher energy density. The MDR process produce Syngas having a ratio $H_2/CO \simeq 1$; for the Fischer-Tropsch process this is a serious advantage, due to the reduction of power requirements of the process [42]. Infrastructures for liquid fuel transportation already exists; instead, the one for natural gas has still to be developed. In addition, the dry reforming reaction allow to convert two of the most impactful greenhouse gasses into added-value products, with evident environmental benefits.

Energy required to perform the MDR reaction is usually supplied via conventional heating, in which a series of tubular catalytic fixed bed reactors are placed into furnaces; flames, generated by the combustion of non-renewable fuels, heat up the external surface of reactors, so that heat is then transferred to the internal section of the pipe, reaching the catalyst surface where the reaction takes place. The involved heat transfer mechanisms are therefore conduction and radiation. However, such reactor arrangement produces important radial temperature gradients; since the reaction absorb lots of heat, due to the very high ΔH_R^0, the central part of the fixed bed reactor will experience lower temperatures, leading to lower catalyst activity, and thus non-uniform reaction rates through the pipe cross-section. In the end, this results in lower reactant conversions, energy efficiency and selectivity

[18]. In addition, heat is transferred not only to the catalyst, where it is needed to activate the reaction, but also to the gas and to the walls of the reactor; as a consequence, not all the energy supplied by flames is used by the reactor.

Such problems can be avoided by exploiting different heat transfer mechanism, other than conduction. Rradiation using Microwaves (MW) has gained huge interest in recent years, because of the possibility of transporting energy directly on the catalyst surface, without energy losses due to heat dispersions as in conventional heating systems. Radiative heating using MW is a well-developed technology nowadays. MW ovens are commonly available on the market, and their price is typically low; MW-assisted organic synthesis has become a reality in the past two decades, allowing to perform highly selective reactions while significantly reducing the time required for heating steps [31]. In addition, gasses are not susceptible of MW dielectric heating; in catalytic systems, large temperature gradients will be created between gas and solid catalyst. The catalyst surface may be at temperatures hundreds of degrees higher than the gas, leading to the inhibition of secondary reactions that typically take place into the gas phase, which are nowadays a challenging problem to be overcome in order to obtain high Syngas purity. However, an extensive implementation of this technology in the chemical industry is still missing, due to the lack of understanding on the mechanisms through which MW heating affects the reactions.

This thesis work aims to contribute to filling this gap of knowledge, by applying the concept of microwave heating to the MDR reaction. It completes previous thesis works, carried out in the dept. of Industrial Engineering at the University of Padova, where a commercial oven was modified, characterized and modelled. From the mathematical modelling procedure, promising results were obtained (in terms of reactant conversions, Hydrogen yields and selectivity, and energy consumption), but experimental validation of such results were still missing, and will be addressed in this work. The most significant performance indices of the lab-scale MDR process are determined, as to obtain quantitative proof of the real feasibility of MW heating applied to gas-solid endothermic catalytic reactions. The structure of this work is divided as follows:

1. In the first chapter the state of the art of MW heating technology is described; the concept of MW heating, its advantages and disadvantages, and the actual challenges that needs to be overcome to achieve large-scale diffusion in the chemical industry are introduced. Some research works are also reported, with particular focus to the MDR reaction.

2. In the second chapter materials and methods used for this thesis work are described; the main equipment used, as well as the working principles and structure are reported in detail.

3. The last chapter is dedicated to the description of results obtained in the experimental campaign carried out in the laboratories. Three main areas of interest were investigated: a reliable temperature measurement strategy under MW heating; a discussion about the development of the experimental setup for

MW heating; finally, the performances obtained in both conventional and MW heating systems are discussed.

Chapter 1

State of the art of microwave heating

Most chemical processes require at least one step where materials are heated. Conventionally, this heating step is carried out in heat exchangers, if temperatures are moderate, or in furnaces, if temperatures are very high. Heat exchangers are capable of operating at temperatures, as high as 500°C, when using molten salts; at higher temperatures, furnaces have to be used. The Methane Dry Reforming process requires temperatures that reach 1100°C, due to the high chemical stability of reactants (highly negative $\Delta G^{0,f}$); thus, it must be performed in furnaces. In this configuration, the catalytic reactor is placed inside the furnace where fuel combustion provides the required energy input. Flames, generated by the fossil fuel combustion, heat the external surface of the reactor (composed by a number of fixed-bed catalytic tubular reactors), providing energy for the highly endothermic reaction. In conventionally heated systems, flames (from fossil fuels combustion) are exploited to generate a temperature gradient across the solid wall of catalytic reactors; their external surface will be at high temperatures, while inside the endothermic reaction absorb heat, leading to lower temperatures in the catalytic bed. Such gradients generates heat fluxes that travel through the reactor's wall, eventually reaching the catalyst surface. Temperature gradients are responsible for uneven temperature distributions in the pipe's cross-section; this negatively affects the performances of catalytic systems. Higher temperatures will be found near the walls; due to the catalyst's heat transfer resistance, and to the presence of endothermic reactions, temperature at the pipe's centre will be significantly lower. This result in lower reaction rates, selectivity, reactant conversions at the centre of the pipe, finally resulting in lower energy efficiencies of the heating systems and lower average conversion at the outlet. In addition, the gas will be heated at high temperatures; kinetics of the gas-phase reactions are enhanced, thus unwanted secondary products will be generated, degrading the product quality, and the application field of the product. Such problems could be solved by using alternative heating techniques; in particular, microwaves (MW) represents an attractive solution. Advantages of MW heating are summarized below:

1. Increased reaction rates
   Reactions rates can increase 10 to 100 folds as compared to conventional heat-

ing when MW are used, due to the ability of MW to substantially increase the temperature at the catalyst surface, enhancing the catalyst's activity. Literature [53] reports that many organic synthesis can be completed with 2-5 minutes under MW heating, where conventional heating require 8-10 hours or more.

2. Efficient heating source
   Microwaves allow to directly heat the catalyst surface, without wasting energy in heating non-reacting parts of the system.

3. Instantaneous heating
   By using MW it is possible to heat the catalyst up to very high temperatures in a very short time; conventional heating instead require large transient, where a lot of energy is used for bringing temperature at the right value, without actually carrying any reaction.

4. Selective heating
   The capability of MW to heat up different materials depends only on their chemical nature; some materials are completely transparent to MW radiation, while others are highly susceptible. This aspect is particularly important in gas-solid catalytic reactions, where the solid is highly susceptible to MW heating while the gas is not. As a result, temperature of the solid phase is higher than the one of the gas phase, hindering the gas-phase reactions.

By using MW, heat is delivered where is needed, in the required amount and at the required moment, as stated by the principles of PI. Such characteristics of MW heating allows chemical reactions to proceed faster than reactions carried out under conventional heating. Due to these characteristics, faster rates of reaction, higher selectivity and reactant conversions, lower reaction time, and higher energy efficiencies are expected with microwave-heating systems. A schematic representation of MW heating is reported in figure 1.1 At present time this technology has, however, some

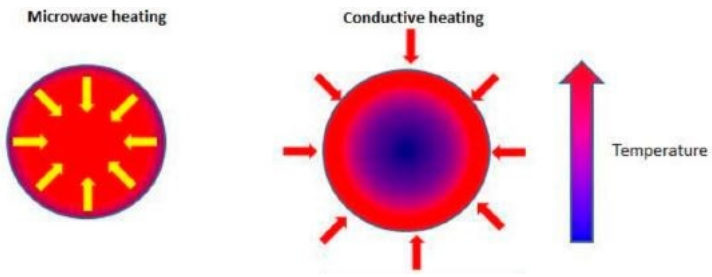

Figure 1.1: Difference between MW (left) and conventional (right) heating [44].

significant drawbacks [5], which are responsible for its poor diffusion in industry;

1. Lack of scalability
   Low prices for MW oven are possible only for small-scale apparatus (commercially available oven). Although there have been developments in the recent past relating to the scalability of microwave equipment, still there is a gap that needs to be filled to make this technology scalable.

2. Limited applicability
   Only dielectric molecules are capable of absorbing heat; MW cannot heat low-dielectric materials, since they are transparent to such radiation. Adequate absorbing materials are often required, leading to complications in the process or higher production costs.

3. Difficulties in Temperature control
   Typical temperature monitoring devices are composed of metallic parts (thermocouples), which are very susceptible to MW radiation.

4. Health hazards
   If the oven is not adequately designed, MW radiation escape from the oven cavity. Radiation exposure can lead to excessive heating of (mainly) eyes and testes, particularly vulnerable because there is relatively little blood flow in them to carry away excess heat, leading to overheating [2].

5. Unclear reaction's mechanism
   Effect of MW on the reaction mechanism is complex, and not fully understood, resulting in a currently ongoing debate among the scientific community. Some authors claims that MW enhance reaction rates due to specific (or non-thermal) effects, caused by the influence of electromagnetic radiation on the chemical process; however, other authors found no evidence of those effects.

Of particular interest is the problem of temperature control, due to the huge impact of temperature on the reaction performances.

1.1 Microwave heating

In the following pages, the nature of MW radiation is explored, along with the effects that it produces on matter and on reacting systems. A brief mathematical description is introduced; finally, the current state of the art is reported.

1.1.1 Microwaves in the EM spectrum

Microwave is a form of electromagnetic radiation, characterized by an energy content too low to ionize atoms on a single event basis (non-ionizing radiation); however, when sufficient power is applied, MW may be able to generate plasma (but only through the intermediate process of classical acceleration of plasma electrons [57]). Although different definitions exists, the commonly accepted definition of MW radiation refer to the portion of electromagnetic spectrum located between frequencies of $0.3-300$ GHz, corresponding to wavelengths of $0.001-1$ m (vacuum or free space wavelength). This radiation is located between the high portion of radio frequencies (VHF), and the lower portion of infrared radiation (Far-IR).

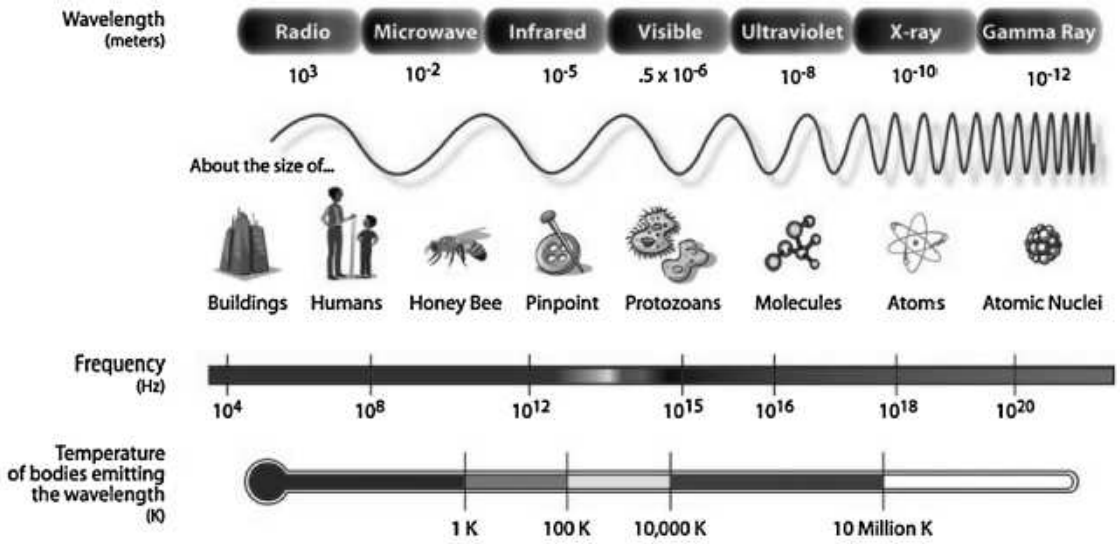

Figure 1.2: The Electromagnetic spectrum [21]

Application of radiation within the MW region is regulated by national and international rules, as to avoid interference with telecommunications [40]. In particular radiation at 941 MHz, 2.45 GHz and 5.85 GHz are the most commonly available for industrial, scientific, and medical use. Radiation at 2.45 GHz is commonly used in domestic microwave ovens.

1.1.2 History

MW radiation was originally used for radar detection during the second World War; only in later times (1967) it was recognized its potential use as heating source for chemical reactions. In contrast to communication purposes, in which microwave's frequency, phase, and amplitude must be accurately controlled to carry the information, for heating purposes efficient irradiation apparatus and output power are important factors to be controlled. This fact result in highly different composition of MW devices.

1.1.3 Microwave generators

Microwaves can be generated by different devices, like magnetrons, power grid tubes, klystrons and gyrotrons. MW production is based on different physical processes, and the selection of the best suited generator depend on various factors, including power, frequency, efficiency, gain, bandwidth, phase, size, weight and cost [21]. The most widespread MW generator is the magnetron, shown in figure 1.3. Its high efficiency, compact size, and low cost are the reasons behind its diffusion in household MW ovens. It converts electrical energy (DC current) to MW radiation at typically 2.45 GHz. Two different types of Magnetrons are present on the market; pulsed magnetrons and continuous wave magnetron. Pulsed magnetrons produces high peak output power (from kW to several MW) for very short duration. Continuous wave magnetrons instead produces continuous output power in the range of few W to kW.

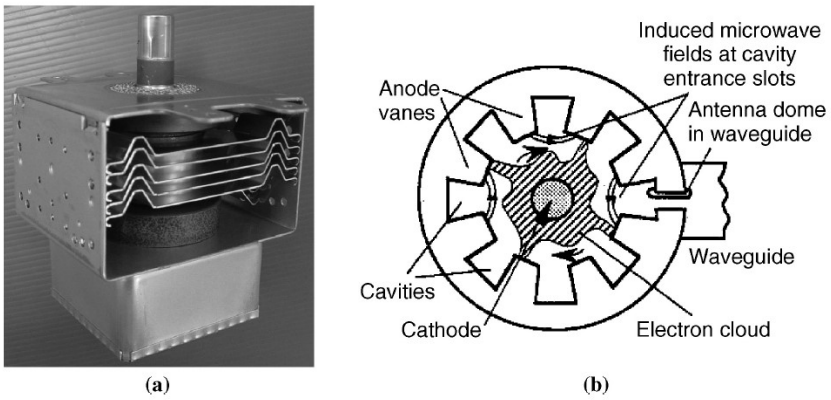

Figure 1.3: Typical aspect of a continuous wave magnetron (a), and a schematic cross-sectional view of the magnetron cavity [21]

The magnetron is a high vacuum electronic valve consisting of a hollow copper anode incorporating a resonant structure, at the centre of which is an electron emitting cathode, typically composed by a Thorium-Tungsten alloy, or by Barium Oxide-coated metal surface. The cathode is a thermo-ionic valve, which emits electrons if heated up to a sufficiently high temperature. Permanent magnets on the outer magnetron structure generate a static EM field, which induce a rotatory motion to the electrons. In the presence of this field, alternating positive and negative voltages are generated on the anode vanes and electrons emitted can either be accelerated or decelerated. Bunching of electrons occurs due to the presence of regions of accelerating and decelerating fields; the resulting electron's clouds shape is shown as shaded region in Figure 1.3b. Characteristics of MW radiation is defined by the anode shape. The cavities and parallel surfaces of the anode behave as capacitors and inductors, thus the magnetron can be represented as an LC circuit, with the resonant frequency defined entirely by its dimensions. Magnetrons requires few components to be powered, which are typically cheap; therefore, the entire MW heating system is characterized by a low cost, which explain the vast diffusion of MW ovens in domestic environments. These components are necessary to convert the AC current (available in Europe at 220 V and 50 Hz) to DC current at a much higher voltage. Such components are;

- Transformer
  It is a device through which the AC current coming from the grid is converted to a much higher voltage. In particular, voltage is changed from the grid's one ($\sim 10^2$ V) to the one required for magnetrons ($\sim 10^3$ V).

- Fuse
  Instantaneous characteristics of electricity from the grid may change depending on the power line load. A fuse is a device that protect the condenser and magnetron from over-currents; the metal wire inside the fuse melts when too much current flows through it, thereby interrupting the electricity flux.

- Capacitor
  Magnetrons are designed to work with continuous currents. In order to convert

the current from AC to DC, a capacitor is used; the resulting time profile of the current coming out of capacitors is not exactly a DC signal, but that's not a problem for magnetrons.

- Antenna and Waveguide
  Microwaves generated in the magnetron must be directed toward the oven cavity. This operation is performed by the antenna and waveguide.

Another common type of MW generator is the Klystron, depicted in figure 1.4; those are high-power MW generators used in applications like linear accelerators, TV transmissions, industrial heating and modern radar systems. Klystrons are characterized by an output peak power of 100 W to 150 MW, while the average power range between 100 W to 1 MW; they produce a frequency ranging from 300 MHZ to 40 GHz. In it, an electron beam is generated by an electron gun and travels along a circuit consisting of a series of resonant cavities separated from each other by drift tubes. Magnets are frequently used to focus the electron beam as it passes through the circuit. The output of the klystron is obtained by velocity modulation of the electron beam, leading to bunching of electrons. Velocity modulation is obtained by varying the velocities of the electrons, alternately accelerating and decelerating the electrons through the application of a microwave signal as they pass through a pair of closely spaced grids in the input cavity, which is located close to the drift tube entrance. Bunches of accelerated and decelerated electrons are further modulated as they pass through intermediate cavities. At the output cavity, the amplified signal is extracted.

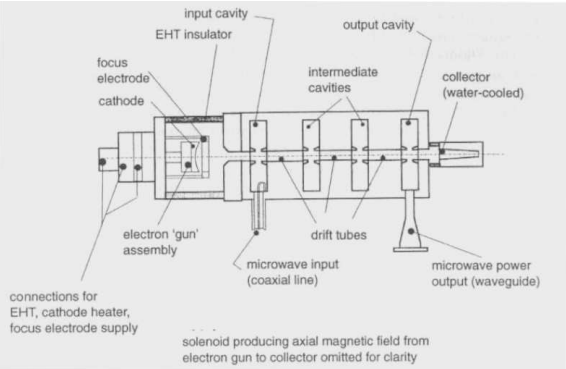

Figure 1.4: Schematic view of a high-power klystron [38]

Another type of MW generator is the Gyrotron: it is high-powered electron tubes which emit a millimeter wave beam by bunching electrons with cyclotron motion in a strong magnetic field. Gyrotrons are capable of producing much higher power levels at millimeter wavelengths than other tubes. Power output can range from kilowatts to several megawatts. Operating frequencies range from about 8 to 800 GHz. Gyrotrons can be designed for pulsed or continuous operation. They are used primarily for the cyclotron resonance heating of fusion plasmas in fusion reactors, for sintering of ceramics and joining of metals.
Power grid tubes are commonly used at lower frequencies and consist of a cathode, grid and anode. The weak microwave signal to be amplified is applied between

the grid and the cathode. The signal applied to the grid controls the electron flow drawn from the cathode and results in a larger signal at the anode. The output of power-grid tubes ranges from low-power tubes capable of producing approximately 1 kW at frequencies of 350 MHz to high-power tubes used in fusion research (plasma heating) that are capable of producing more than 2MW of output at frequencies in the 30 MHz range through the use of special grid structures.

1.1.4 Microwave oven applicators

Electromagnetic energy produced in MW generators is delivered to the load in applicators; those can be waveguides, travelling wave applicators, multi-mode and single-mode cavities. Depending on the system's geometry, different number of resonant modes can be generated. Typically, a magnetron generates EM waves within a frequency spectrum of 2.45 $GHz \pm 50$ MHz (where most of the output power is emitted at 2.45 GHz); depending on how the waves are transferred to the load, different applicators are identified. By far, the most used MW applicator is of the multimode type, used in domestic ovens, for a large number of low power industrial units, and many high-power installations. It is characterised by a mechanical simplicity and versatility, due to its capacity of accepting a wide range of heating loads; however, heating uniformity is frequently a problem [39]. In multi-mode applicators, the cavity dimensions are several wavelengths long in at least two dimensions; in it, a large number of resonant modes are present, for a given frequency range, so that many different resonant wave frequencies are present. Such modes add vectorially in space and time, to give a resultant field pattern, which result in a complex evolution of the field distribution. In a multi-mode cavity, multiple modes are excited within the cavity, hence it is not possible to separate the electric and magnetic components of the EM field. In multi-mode ovens, it is essential to design the load as to obtain load matching, where the impedances of the load, the generator and the waveguide are designed as to minimize power reflections. Proper load matching, in multi-mode applicators, allow to introduce a certain mode splitting effect of degenerate modes which is a desirable effect, since it enhances the uniformity of heating within the applicator.

In single-mode oven applicators, a standing wave pattern is generated, which for simple structures is well defined and predictable in space; typically, the load is placed in a specific point where the electric field is maximised, thus the power transferred to the load is high. Single-mode ovens have a small cavity, which allows to concentrate the EM field. The magnetic field maximum is instead located in a different position, allowing for separation of magnetic and electric fields. Single-mode applicators are often characterised by high absorption of the incident energy; however, operation must be within narrow frequency bands in order to maintain high coupling efficiencies. Single-mode applicators are characterised by very high power densities (10^7 kW/m^3). However, their cost is much higher than multi-mode applicators.

Travelling wave applicators (TWA) are instead characterized by the absence of

resonant modes. All the power emitted is either absorbed by the work load, or by a terminating load, so that there's negligible reflected power, hence, no standing waves are formed. Due to the absence of resonant modes (stationary waves), TWA represents the simplest type of applicators; the EM field they generate can be easily described from a mathematical point of view. Many different TWA configurations exists, depending on the cavity shape. An example of the electric field pattern generated in a standing-wave type single-mode applicator (waveguide) is reported in Figure 1.5a; the EM field pattern in multi-mode applicators is instead reported in Figure 1.5b.

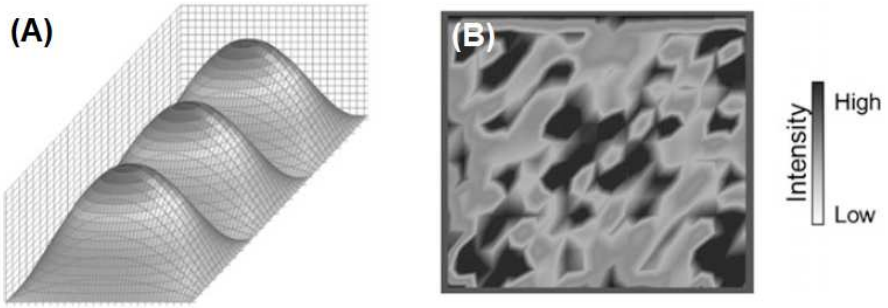

Figure 1.5: Representation of the EM field distribution in single-mode and multi-mode applicators [26].

1.1.5 Microwave-material interactions

In order to determine the interactions between matter and MW radiation it is first necessary to understand the dielectric properties of materials, since the alternating electric (and, less frequently, magnetic) field of the EM wave interacts with the atomic structure. Matter is composed by charged particles (electrons in the external shells, distributed on various orbitals, and protons in the nucleus); depending on the charge distribution, molecules may have a net charge (ions and electrons), may have zero net charge but non-symmetrical charge distribution of electrons around nuclei (dipoles), or may have zero net charge and a symmetrical charge distribution (non-polar molecules). A material is classified as dielectric if it has the ability to store energy upon application of an external electric field [26]. When an external static EM field is imposed on ions or dipolar molecules, these tends to orientate in a direction opposite that of the applied EM field, as to reduce the energy content of the system; potential energy will be stored in the molecules in the final equilibrium position. When the direction of the applied EM field is inverted, dipoles will attempt to rotate of 180°, transforming potential energy into kinetic energy, which is used to return in the configuration that minimize the system's energy content. If the applied field oscillate with a certain frequency, dipoles will attempt to rotate each time the applied field change direction. Each molecule is a physical entity, characterized by mass and inertia. At high enough frequencies, dipoles will not rotate as fast as the EM field; at each rotation, a fraction of potential energy will be returned to the system in form of kinetic energy, that is, heat. In the most common case, MW generate heat due to the inability of polarized molecules to follow extremely rapid

reversals of the EM field. There are different polarization mechanisms, depending on the atomic structure of materials [3], which are schematically shown in figure 1.6:

1. *Orientation (or Dipolar) polarization* is typical of dipolar molecules. Such molecules, in absence of applied EM fields, have permanent dipole moments which are randomly oriented. When EM fields are applied, dipoles tend to reorientate as to reduce the energy content of the system, directing the dipole parallel to the field. An example of such materials is Water, or Hydrogen Chloride.

2. *Electronic polarization* refer to the mechanism where electrons around nuclei are displaced from their low-energy state. Displacement of these charge particles from their equilibrium position give rise to induced dipoles, which respond to the applied field. In covalent solids, such as crystalline Silicon, the valence electrons in the covalent bonds are easily shifted (compared to the rigid ionic cores of ionic solids) under influence of EM fields. Such materials are characterized by high dielectric constants.

3. *Ionic or Atomic polarization* occur due to the relative displacement of positive and negative ions/atoms within molecules, and crystal structures from their equilibrium lattice sites. Nuclei are displaced from their equilibrium position, thus the net dipole moment is no longer zero. Examples of such materials are Alkali Halides, and combinations of elements from Groups I and VII of the periodic table.

4. In heterogeneous systems, free charges tend to accumulate at interfaces within the material, like grains, defect regions, or phase boundaries. This polarization phenomenon is termed *Maxwell-Wagner polarization*.

In high-conductivity materials, such as metals, interaction with the EM field produce a force that pushes the conducting electrons outward into a narrow area near the surfaces; eddy current density decreases exponentially with depth; this effect is known as *skin effect*, and it is exploited for induction heating of metals. Together with the Joule effect (generated by collisions of electrons with nuclei in solid conductors), such physical phenomena represents the basis of microwave; the different mechanisms are depicted in figure 1.6. The electric field component of the EM wave may be reflected, transmitted or absorbed by materials; also, materials may interact with the electric or magnetic field component of the EM wave. With respect to MW, materials can be classified into the following categories;

- *Opaque materials*, typically conducting materials with free electrons (such as metals), reflect the EM wave without allowing it to pass through;

- *Transparent materials* are typically low-dielectric loss materials or insulating materials (such as glass, ceramics and air), reflect and absorb the EM wave to a negligible extent and allow ME to pass through easily with little attenuation;

- *Absorbing materials*, also referred to as lossy dielectrics, absorb EM energy converting it into heat. Their properties range from conductors to insulators;

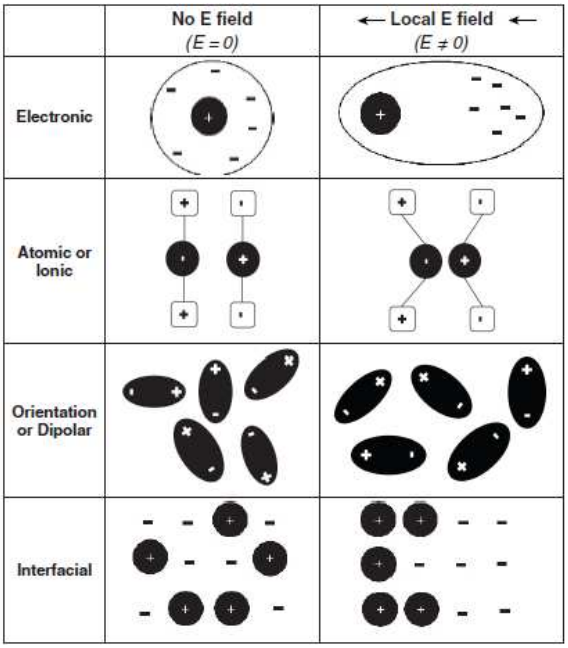

Figure 1.6: Different polarization mechanisms [21].

- *Magnetic materials* interacts only with the magnetic component of the EM wave.

Absorbing (or dielectric lossy) materials are the most interesting materials in MW heating, due to their ability to heat up when. In catalytic systems, under conventional heating, heat is transferred from the outer surface to the inside of the catalyst. Physical contact between the heat source and the catalyst (via the reactor wall) is required. The catalyst particle, support, and the entire catalyst bed are simultaneously heated; the temperature distribution is determined by the conductive heat transfer characteristics of the solid, plus the convective heat transfer characteristics in the fluid. In contrast, EM waves may interact directly with components that possess ability to absorb MW energy. Low-dielectric materials are not heated by the radiation; instead, they are indirectly heated by the conductive, convective and radiative heat transfer mechanisms that takes place into the catalytic bed.

1.1.6 MW effects on reacting systems

When reacting systems are subject to MW heating, it is possible to distinguish between different effects, which may lead to kinetic enhancement of the reaction;

1. *Thermal Effects*
   Microwave dielectric heating involve several thermal effects that are not found in conventional heating systems, such as (i) hot-spot formations, (ii) selective heating and (iii) super-heating. The first two effects are important in gas-solid catalysed reactions; the temperature gradient between the solid catalyst and gas phase allow to suppress undesired secondary gas-phase reactions, while hot spots are responsible for kinetic enhancements of the catalytic reaction. Typical hot-spot are $90 - 1000\ \mu m$ large; here, temperature

is $100 - 200\ K$ higher than the average bed temperature. This temperature difference affect the temperature-dependent part of the Arrhenius equation, $k(T) = A_0 \exp(-E_a/RT)$, leading to faster reactions.

2. *Non-thermal (athermal) effects*
Still a subject of intense debate in the scientific community, this mechanism has been postulated to explain unexpected yield enhancements that might not be explained by the previous two mechanisms; in this category we find the mechanisms where direct interactions between the EM field and specific reacting molecules takes place. The EM field may interact with the orientation of dipolar molecules or intermediates, resulting in a modification of the pre-exponential factor (A_0, related to frequency of collisions between molecules) or the energy term (E_a related to the energy barrier required to reach the intermediate transition state during the reaction). This modification may determine the enhancement observed in literature. Several authors suggest evidences for the presence of such non-thermal effects ([55], [15], [33], [12]); others ([29], [7], [60]) believe that this phenomenon may be traced back to non-accurate temperature measurements in the reaction environment.

Kinetic enhancement may be due to both contributions; however, a precise distinction between each contribution is hard to define. It is commonly agreed that thermal effects play the most important role in most standard cases ([31], [17]).

1.1.7 Mathematical description of dielectric properties

The effect of EM fields on matter is described by the Maxwell's equations (eqs.1.1, reported in their differential form), the set of coupled partial differential equations representing the foundation of classical electromagnetism theory;

$$\begin{aligned} \nabla \cdot \boldsymbol{D} &= \rho \\ \nabla \cdot \boldsymbol{B} &= 0 \\ \nabla \times \boldsymbol{E} &= -\frac{\partial \boldsymbol{B}}{\partial t} \\ \nabla \times \boldsymbol{H} &= \frac{\partial \boldsymbol{D}}{\partial t} + \boldsymbol{J} \end{aligned} \tag{1.1}$$

Response of matter to MW radiation depends on its nature; electrical conductivity (σ), electric permittivity (ε), and magnetic permeability (μ) are the physical properties of materials that determine interaction with respect to MW. They are influenced by the physical and chemical nature of matter, but also from the radiation characteristics and material temperature. In a dielectric material, the presence of an electric field $\boldsymbol{E}$ causes the bound charges in the material (atomic nuclei, electrons) to slightly separate, inducing a local electric dipole moment. This effect is measured by the electric displacement field $\boldsymbol{D}$;

$$\boldsymbol{D} = \varepsilon \boldsymbol{E} + \boldsymbol{P} = \varepsilon' \boldsymbol{E} \tag{1.2}$$

where $\boldsymbol{P}$ is the density of permanent (or induced) electric dipole moments. Similarly, the effect induced by the magnetic field is measured by the vector field $\boldsymbol{H}$;

$$\boldsymbol{B} = \mu_0(\boldsymbol{H} + \boldsymbol{M}) = \mu' \boldsymbol{H} \tag{1.3}$$

where $\boldsymbol{M}$ is magnetization. The link between applied EM field and resulting charge displacement in materials is ruled by the quantities ε, defined Electric Permittivity, and μ, the Magnetic Permeability. Such properties describes the capability of materials to interact with the incident radiation. Microwave is an oscillating electro-magnetic field; electro-magnetic waves may be represented by trigonometric functions, or equivalently, by an exponential function and complex numbers, thanks to the Euler's identity.

$$\varepsilon^* = \frac{\boldsymbol{D}}{\boldsymbol{E}}(\cos\delta + j\sin\delta) = \varepsilon' e^{-j\delta} \tag{1.4}$$

It follows that electric permittivity and magnetic permeability can be conveniently expressed in terms of complex quantities as stated in equations 1.5 and 1.6;

$$\varepsilon^* = \varepsilon' - j\varepsilon'' = \varepsilon_0(\varepsilon'_r - j\varepsilon''_{eff}) \tag{1.5}$$

$$\mu^* = \mu' - j\mu'' \tag{1.6}$$

where $\varepsilon' = Re(\varepsilon)$, the real part of complex electrical permittivity, known as *Dielectric Constant*, characterize the ability of materials to store electrical energy; $\varepsilon'' = Im(\varepsilon)$, the imaginary part of complex electrical permittivity, is defined *Loss Factor*, and reflect the ability of materials to dissipate electrical energy as thermal energy, being associated with the oscillatory component; ε_0 is the vacuum permittivity, ε_r is the Dielectric Constant in the material, and j is the imaginary unit. Dielectric properties of materials are function of the angular frequency typical of the applied EM field. Concerning magnetic properties, $\mu' = Re(\mu)$ is the real part of the complex magnetic permeability, representing the amount of magnetic energy stored within the material, while $\mu'' = Im(\mu)$ is the imaginary part of the complex magnetic permeability, representing the amount of magnetic energy which can be converted into thermal energy [53].

Dielectric heating can be generated by different physical processes related to the wave-material interactions. Since it is difficult to separate the different polarization mechanisms, all losses can be grouped together, leading to the definition of an *effective loss factor* ε''_{eff} (eq. 1.7);

$$\varepsilon''_{eff} = \varepsilon''_d + \varepsilon''_e + \varepsilon''_a + \varepsilon''_{MW} + \frac{\sigma}{\varepsilon_0\omega} \tag{1.7}$$

where the subscripts d, e, a, and MW refer to dipolar, electronic, atomic and Maxwell-Wagner respectively. Typically, one or two mechanisms dominate.

When an EM field is applied, electric charges in the material tends to orientate in its direction; however, an oscillating field continuously change direction, resulting in a continuous motion of charges. This alignment do not take place instantaneously, but the material response arises after a lag time; this lag can be represented geometrically on the complex plane $(\varepsilon', \varepsilon'')$ as an angle δ, as shown in Figure 1.7;

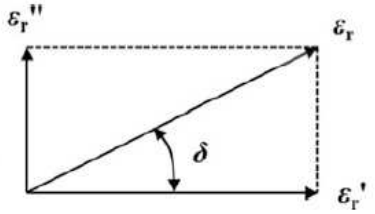

Figure 1.7: Loss angle representation on the $(\varepsilon'_r, \varepsilon''_r)$ plane [26].

The material response to the electric field imposed is measured by the *Loss angle* δ, representing the phase difference between the oscillating electric field and the material polarization. The loss angle is often expressed in terms of its tangent (*Loss tangent*, eq.1.8);

$$\tan(\delta) = \frac{\varepsilon''_{eff}}{\varepsilon'} \tag{1.8}$$

Due to the definition of ε' and ε'', the loss tangent $\tan(\delta)$ expresses the ratio of electric energy lost as heat to the energy stored stored into the material. Typical values of loss tangent for solid materials are shown in Figure 1.8; Materials characterized by high loss tangent (like C, SiC, Fe_xO_y...) absorb very efficiently the electromagnetic radiation, while low-dielectric lossy materials (like NiO) do not absorb it. Dielectric properties depends on temperature, frequency, material purity, manufacturing process and particle size (for granular materials). A list of loss tangent values for common materials is reported in table 1.1.

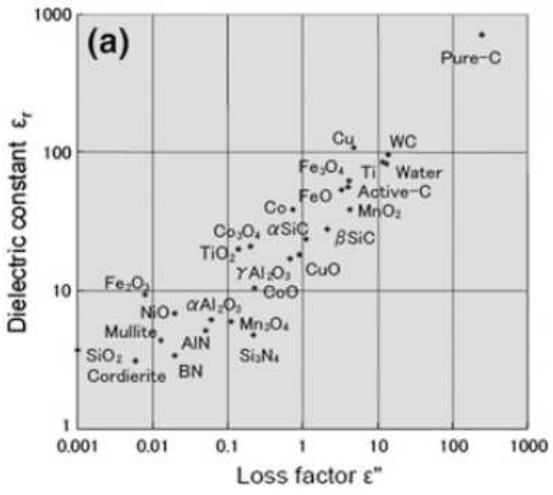

Figure 1.8: Complex permittivity and loss factor of various powders [26].

Table 1.1: List of dielectric properties for common materials .

Material	ε'_r	ε''_{eff}	Temperature [°C]	Frequency [GHz]	Ref.
$\alpha - Al_2O_3$	8-10	0-1	100-200	2.45	[59]
$\gamma - Al_2O_3$	3.006	0.1720	-	2.45	[59]
Teflon	2.14	0	25	2.45	[52]
SiO_2	3.066	0.215	-	2.45	[59]
C	7	2	25	2.45	[23]
	26	10	25	2.45	[52]
SiC	26.66	27.99	-	2.45	[45]
	30	11	20	2.45	[38]
	5.68	0.515	0	2.45	[6]
	7.7	0.44	1300	2.45	[6]
$\alpha - SiC$	9.8	51.8	0	2.45	[56]
	13.7	325.6	1000	2.45	[56]
Ni/SiC	19.58	8.23	646-946	4.2	[30]
SiC (La-doped)	14.5-12	4.5-4	600-950	4.2	[30]
Quartz	3.78	0.001	25	2.45	[52]

1.1.8 Frequency and Temperature dependence

Literature studies ([27], [56], [62]) have shown that the material's dielectric properties change with some important process parameters; the EM wave frequency, the sample temperature, and particle size of the solid material. There's no

The relations $(\varepsilon''_r, \varepsilon'_r) = f(T, f, d_p)$ must be obtained from experimental data, which are available only for commonly studied materials. In the case of interest, the material to be studied is Silicon Carbide (SiC), chosen because of its high loss tangent, chemical inertness, coupled with high mechanical strength and thermal properties; it is used as dielectric lossy material in our tests, in order to absorb the electromagnetic radiation, transforming it into heat to be used by the catalyst particle. Silicon Carbide is a ceramic material of interest in the field of electronics, due to its semi-conductor nature; it is currently under investigation for uses in harsh environments as substitute of more common semiconducting materials. Similarly to pure Silicon, SiC dielectric properties can be varied by using doping agents. The presence of many different SiC solid mixtures (produced by addition of different amounts of different doping agents), along with the natural polymorphism of SiC, makes very challenging the task of retrieving accurate experimental informations for SiC used in our experiments, and therefore the accurate estimation of its dielectric properties.

Effect of temperature

Real and imaginary permittivity change with temperature. Since the loss tangent is defined by starting from ε''_r and ε'_r, the capability of SiC of absorbing MW radiation change with temperature. In SiC the loss tangent increases with temperature, maintaining constant the sample size and MW frequency; at higher temperatures

therefore the material will be more susceptible to dielectric heating and also the fraction of incident radiation that reaches inner layers of SiC decrease as temperature increase, as discussed in [56].

Effect of radiation frequency

Changing the frequency will affect the SiC capabilities of absorbing radiation; however, this dependency is not important, since household MW ovens have typically a fixed frequency of 2.45 GHz. Generally, lower frequencies are associated with lower radiation absorption, thus the radiation penetrate deeper into the material. Effect of Temperature and Frequency for SiC is reported in figure 1.9.

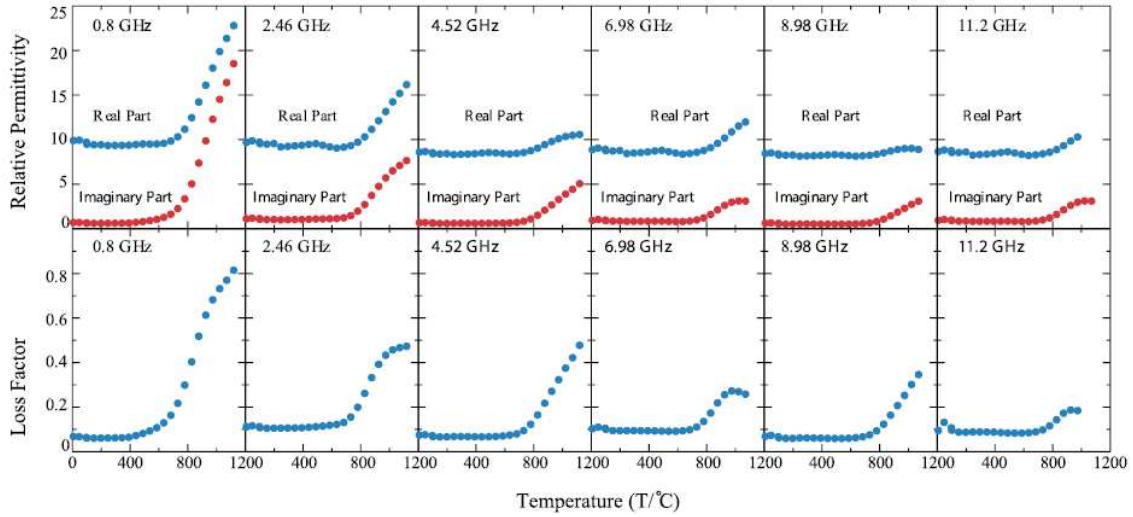

Figure 1.9: Effect of temperature and frequency on dielectric properties of $\beta - SiC$ having particle size of 530 nm [56].

1.1.9 Penetration Depth

As the electromagnetic radiation passes through lossy dielectric materials, the intensity of the EM field decreases as part of this energy is dissipated as heat. Wave propagation in continuous materials is governed by the Maxwell's equations; for a planar wave propagating in the inward direction, the equation describing its evolution in space and time of the electric field is reported in equation 1.9 [3];

$$\frac{\partial^2 \boldsymbol{E}}{\partial z^2} = \varepsilon_0 \varepsilon^* \mu_0 \mu^* \frac{\partial^2 \boldsymbol{E}}{\partial t^2} \tag{1.9}$$

The solution to be considered is that of a plane wave;

$$\boldsymbol{E} = \boldsymbol{E}_0 e^{-\alpha z} e^{j(\omega t - \beta z)} \tag{1.10}$$

Equation 1.10 describe wave propagation into a continuous material. Constant α is defined attenuation factor; it is related to the attenuation of $\boldsymbol{E}$ within the material, while β is the phase factor, related to the phase shift of the wave. Such constants

are determined from the material's dielectric properties and from the wave characteristics, as described by equations 1.11 and 1.12 (where all the properties are real numbers, since both phase and attenuation factors must be real numbers) [54].

$$\alpha = \omega \left[\frac{\mu\varepsilon}{2} \left(\sqrt{1 + \frac{\sigma^2}{\varepsilon^2\omega^2}} + 1 \right) \right]^{\frac{1}{2}} \tag{1.11}$$

$$\beta = \omega \left[\frac{\mu\varepsilon}{2} \left(\sqrt{1 + \frac{\sigma^2}{\varepsilon^2\omega^2}} - 1 \right) \right]^{\frac{1}{2}} \tag{1.12}$$

The electric field strength at a certain point determine the power dissipated through dielectric heating; in fact, the dissipated power per unit volume of material can be written as

$$P = \frac{1}{2}\sigma|\boldsymbol{E}|^2 + \pi f \varepsilon_0 \varepsilon_r''|\boldsymbol{E}|^2 + \pi f \mu_0 \mu_r''|\boldsymbol{H}|^2 \tag{1.13}$$

where $|\boldsymbol{E}|$ and $|\boldsymbol{H}|$ denote the strength of the MW electric and magnetic field, respectively, and σ is the electric conductivity of the material. Since P varies with $|\boldsymbol{E}|^2 = E_{rms}^2$, the dissipated power is very sensitive to α; in fact, P is proportional to $e^{-2\alpha z}$. It is possible to define the Penetration Depth as the distance from the surface where power carried by the radiation drop to 36.8% of its initial value (equal to $1/e$); it can be evaluated by

$$D_p = \frac{1}{2\omega}\sqrt{\frac{2}{\mu'\mu_0\varepsilon'\varepsilon_0}} \frac{1}{\sqrt{\sqrt{1 + \left(\frac{\varepsilon''_{eff}}{\varepsilon'}\right)^2} - 1}} \tag{1.14}$$

If the material is not magnetically susceptible (like SiC), the equation simplifies to

$$D_p = \frac{\lambda_0'}{2\pi\sqrt{2\varepsilon'}} \frac{1}{\sqrt{\sqrt{1 + \left(\frac{\varepsilon''_{eff}}{\varepsilon'}\right)^2} - 1}} \tag{1.15}$$

The distance for absorption of microwaves to reach 50% of the initial microwave power is given by the half power density depth $D_{1/2}$, estimated from Eq. 1.16 [26];

$$D_{1/2} = \frac{3.32 \cdot 10^7}{f\sqrt{\varepsilon''}} \tag{1.16}$$

Because MW only penetrate for a certain depth in the material, this depth has to be carefully taken into account in the design phase of catalysts for MW-assisted processes; if the catalyst volume is too large, MW energy may not be able to reach the catalyst's core, leading to non-uniform heating. Moreover, the temperature dependence of ε' and ε'' makes this penetration depth not constant.

Precise estimations of D_p in materials is strictly related to the evaluation of dielectric properties. For the dielectric lossy material considered in this work, Silicon Carbide, precise estimations of $\varepsilon', \varepsilon''$ are not easy to find. That's because of the large variability of sample dimensions, MW frequency, doping agents, and temperature at which the measurements can be performed. For Silicon Carbide, literature estimate a penetration depth of 0.97 cm at 2.45 GHz and 20°C ([21]).

1.1.10 Temperature measurements during Microwave processing: the significance of thermocouple effects [47]

Temperature measurement during MW processing is not a trivial task, representing one of the most challenging problem for the diffusion of MW heating. *Pert et al.* [47] determined the effects derived from the introduction of a metallic thermocouple into the MW cavity, distinguishing among the various physical processes that may lead to inexact measurements. Temperature measurement techniques that can be implemented in MW processing are listed in figure 1.10 (reported in the article); among them, thermocouple measurements is the cheapest technique, but it may lead to important measurement errors. Effects related to the presence of thermocouples

	Monochromatic radiation pyrometer	Two-color radiation pyrometer	Optical-fiber thermometer	Thermocouple
Measurement range (°C)	0–2800	400–4000	0–1900 (monochromatic) 500–1900 (two-color)	0–1600
Cost	Low to moderate	Moderate to high	High	Very low to low
Accuracy	Moderate to high	High to excellent	Excellent	Good in conventional furnace; unproved in microwave furnace
Problems	Large minimum spot size; sensitive to magnitude of emissivity	Sensitive to slope of emissivity	Delicate probe; cannot interchange probes readily; contamination of probe	High temperature not available; perturbs microwave field; contamination of sample

Figure 1.10: Comparison of T measurement techniques during MW processing [47].

in the oven cavity may or may not be pronounced; their presence depends on several factors, among which (i) the thermocouple size, (ii) dielectric properties of materials in the cavity, (iii) particle size of the material, (iv) heating rate, (v) atmosphere in the sample, (vi) MW frequency, and (vii) electric field intensity. Authors defined four different effects that may arise from the presence of thermocouples into the MW oven, which may (or may not) lead to measurement inaccuracies.

The first detectable effect is related to the electric field enhancement nearby the thermocouple tip. Thermocouples are generally metallic devices; their presence distorts the EM field. In particular, computer simulations of the EM field (in which the Laplace's equation is solved) shows that the electric field is more intense around the thermocouple tip. Since the delivered MW power is proportional to the square of electric field intensity, there may be local temperature increments that cannot be neglected. Figure 1.11 illustrates the tip-enhancing effect, plus the calculated relative absorbed power density along the axial direction of the thermocouple, from the thermocouple tip toward the sample boundary; it can be seen how the thermocouple presence increase significantly the amount of absorbed power, leading to temperature measurement inaccuracies. Due to increased power absorption, the risk of thermal runaway is increased in presence of thermocouples.This effect is well known in literature, since similar studies showed the same results [32].

Another effect is related to the dielectric breakdown of the materials present in the oven cavity. Dielectric (or electrical) breakdown refer to a process that occour when an electrical insulating material, subjected to a high enough voltage, suddenly

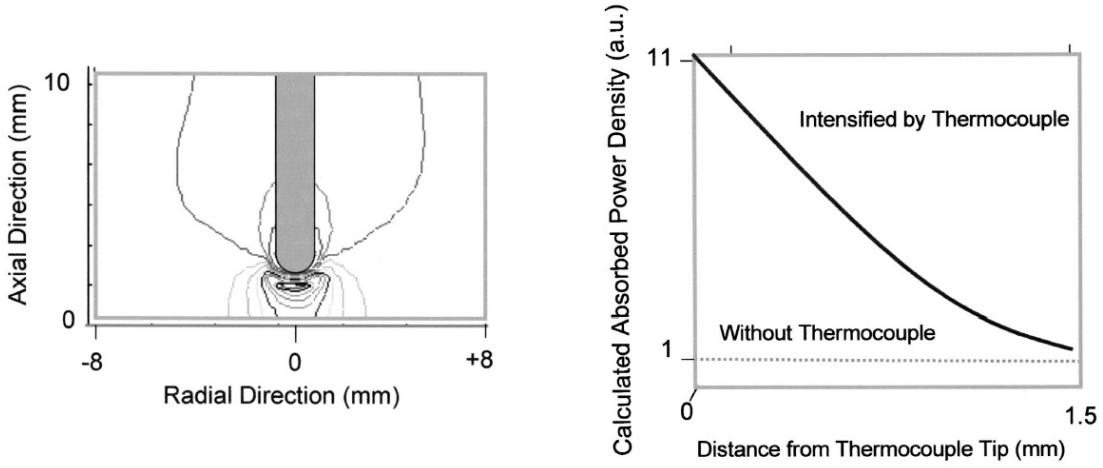

Figure 1.11: Contour lines of the EM field nearby the thermocouple tip (left) and calculated relative absorbed power density along the axial direction of the thermocouple, from the tip to the sample boundary [47].

becomes an electrical conductor and electric current flows through it. All insulating materials undergo breakdown when the electric field caused by an applied voltage exceeds the material's dielectric strength. The voltage at which a given insulating object becomes conductive is called its breakdown voltage and depends on its size and shape. This phenomenon may be enhanced by the presence of intensified electric field near the thermocouple tip; in addition, the phenomenon of "dielectric lens" may contribute at the micro-scale. At high temperatures (> 900°C), the effect may be even more pronounced; that's because the metallic thermocouple at those temperatures emits electrons, facilitating the formation of plasma in the material. If the thermocouple is made of metallic parts, it is capable of depositing carbon; in our system, this effect would be hidden due to the natural formation of Coke from Methane and Carbon Dioxide.

Another process involved in thermocouple measurements under MW heating is related to the presence of Ohmic losses. In metallic objects, MW radiation is capable to excite free electrons, generating an electric current. This current lies in the very superficial part of the object, contained in the so-called skin depth. This region is typically limited to few μm into the metallic object [39]. Ohmic loss (or Joule effect) refer to the physical process in which heat is generated by a current flow in a non-zero resistance (or impedance, for AC currents) material; in presence of high power absorbed by the thermocouple, the importance of Joule effect cannot be neglected; the thermocouple will be heated by radiation. However, this thermocouple effect is important only when processing low-lossy materials ($\tan(\delta) < 0.1$), while can be neglected for high-moderate lossy materials. If Ohmic losses are so important that the thermocouple reach $T > 900$°C, then electron emission, electrical breakdown and arching may take place, seriously damaging the thermocouple or the experimental system.

The last effect generated by the presence of thermocouples in MW ovens is related

to thermal conduction. The metallic material of which the thermocouple is composed is characterized by high thermal conductivity; if this coefficient is higher than the one of the sample, then heat will be conducted away from the sample, reducing its temperature. This effect is however negligible if the thermocouple's thermal conductivity is lower than the sample's one.

1.2 Literature survey on Syngas catalytic production via Methane Dry reforming with Microwaves

Interest of scientific community toward MW heating grew significantly since the introduction of cheap MW-generating devices on the market [31]. Catalytic endothermic reactions, in particular, is a field where promising developments are forecasted in the next years, due to a series of advantages related to the selective nature of microwave heating. In the following pages the most important studies concerning MW heating applied to catalytic reactions are examined. Some important reviews are given by Durka et al. [17], Stefanidis et al [53], and Palma et al. [44], where a series of articles concerning MW heating of gas-solid endothermic catalytic reactions are listed. Generally, higher selectivity and conversions, enhanced reaction rates, and reduction of reaction temperatures in MW heating systems than in conventional heating systems are found; however, many different chemicals were used as feedstock molecules (methane, biomasses, ethanol...), under different operating conditions (low or high temperature processes, plasma-based processes, single-mode or multi-mode MW reactors...), with several catalytic systems. In the following paragraphs, work performed by different research groups concerning the application of MW heating to the Dry reforming reaction is reported and analysed.

1.2.1 Thermodynamic equilibrium framework

The MDR reaction is highly endothermic, requiring high temperatures to activate the stable reactants. The reaction is thermodynamically hindered, as the highly positive ΔH^0_{298} imply. Thermodynamic spontaneity of the reaction is favoured by high temperatures, due to the highly positive ΔG^0_{298}.

$$CO_2 + CH_4 \leftrightarrows 2CO + 2H_2 \qquad \Delta H^0_{298} = +247.3\ kJ/mol \tag{1.17}$$

$$\Delta G^0 = 61770 - 67.32T \qquad \Delta G^0 \leq 0 \Leftrightarrow T \geq 917\ K \tag{1.18}$$

An additional problem is that Carbon deposition is favoured, thus catalyst deactivation is a major challenge. The catalyst choice, operating conditions and reactor type influence carbon deposition; several studies and patents were developed to reduce the problem of catalyst deactivation, which however cannot be completely eliminated [22]; thus long tests should be performed to verify the catalytic activity over time. The thermodynamic equilibrium analysis (which will be further elaborated in this Thesis in chapter 3.3.1) performed by Nikoo and Amin [41] suggested a complex reaction mechanism, involving 17 different reactions, listed in table 1.2. Amounts of the most important species present at equilibrium is reported in figure 1.12; the

problem of Carbon deposition is evident in the figure, particularly at low temperatures. The complex reaction mechanism, the large amounts of carbon formed, and the need of high temperatures, makes the implementation of the MDR process in industry very challenging.

Table 1.2: Reaction mechanism for Dry reforming of methane suggested in [41].

# Reaction	Reaction	$\Delta H^0_{298}[kJ/mol]$
1	$CH_4 + CO \leftrightarrows 2CO + 2H_2$	+247
2	$CO_2 + H_2 \leftrightarrows CO + H_2O$	+41
3	$2CH_4 + CO_2 \leftrightarrows C_2H_6 + CO + H_2O$	+106
4	$2CH_4 + 2CO_4 \leftrightarrows C_2H_4 + 2CO + 2H_2O$	+284
5	$C_2H_6 \leftrightarrows C_2H_4 + H_2$	+136
6	$CO + 2H_2 \leftrightarrows CH_3OH$	-90.6
7	$CO_2 + 3H_2 \leftrightarrows CH_3OH + H_2O$	-49.1
8	$CH_4 \leftrightarrows C + 2H_2$	+74.9
9	$2CO \leftrightarrows C + CO_2$	+172.4
10	$CO_2 + 2H_2 \leftrightarrows C + 2H_2O$	-90
11	$H_2 + CO \leftrightarrows H_2O + C$	-131.3
12	$CH_3OCH_3 + CO_2 \leftrightarrows 3CO + 3H_2$	+258.4
13	$3H_2O + CH_3OCH_3 \leftrightarrows 2CO_2 + 6H_2$	+136
14	$CH_3OCH_3 + H_2O \leftrightarrows 2CO + 4H_2$	+204.8
15	$2CH_3OH \leftrightarrows CH_3OCH_3 + H_2O$	-37
16	$CO_2 + 4H_2 \leftrightarrows CH_4 + 2H_2O$	-165
17	$CO + 3H_2 \leftrightarrows CH_4 + H_2O$	-206.2

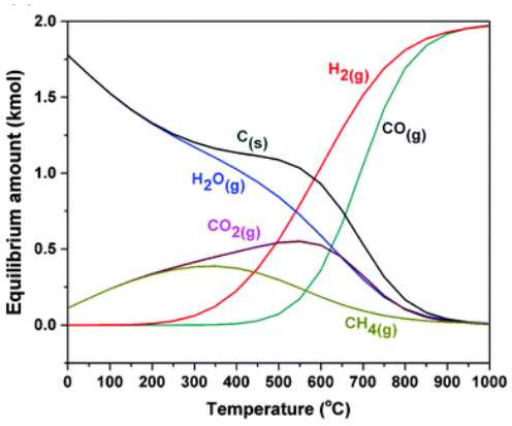

Figure 1.12: Equilibrium compositions of all the species, included solid carbon [23].

1.2.2 J. Chaouki, S. Hamzehlouia, S.A. Jaffer [23]

Chaouki et al. studied the MDR process under both MW heating and conventional heating, testing a catalyst specially developed for the purpose of enhancing MW absorption. The catalyst developed consist in silica sand (SiO_2, particle size

$= 212 - 250\ \mu m$) coated with pure C receptors, which allows for MW dielectric heating. Carbon is inserted into the SiO_2 structure through chemical vapour deposition, which allows for the creation of a coating layer of C, $5 - 450\ nm$ thick. Dielectric properties measurements allowed to determine the MW-absorbing capacity of the catalytic system. The experimental setup implemented in the article is shown in figure 1.13; an important aspect of this setup is the presence of thermocouple grounding, which allows convey electrical currents away from the thermocouple, as to eliminate the thermocouple effects and microwave interaction leading to measurement errors.

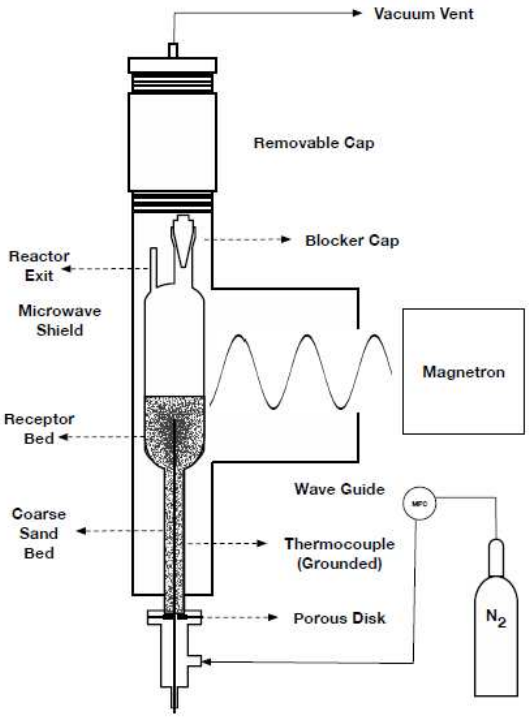

Figure 1.13: Experimental setup for the MW heating fluidized bed reactor.[23].

In the article the advantages of MW heating are defined in heating uniformity and selectivity, and volumetric heating; high power density, and instantaneous temperature control; reduced energy consumption, high reaction selectivity, less heat transfer limitations, process flexibility and equipment portability. However, the study is focused on the importance of the specificity of MW heating; since the gas is not heated by MW radiation, they expect a significant temperature difference between the catalyst surface and the gas mixture flowing around the catalyst particle. This difference, quantified hundreds of degrees ($\simeq 300$řC), is expected to inhibit the secondary gas-phase reactions, while allowing only for reactions on the catalyst surface to take place. Secondary gas-phase reactions, like Methane cracking (MC, eq. 1.19), Water-gas shift (WGS, eq. 1.20), and the Carbon Monoxide disproportion (Bou, eq. 1.21) profoundly restrict the MDR process productivity, due to carbon deposition on active catalyst sites and product consumption, decreasing the process'

selectivity toward Hydrogen and Carbon Monoxide.

$$CH_4 \rightarrow C + 2H_2 \tag{1.19}$$

$$CO_2 + H_2 \leftrightarrows CO + H_2 \tag{1.20}$$

$$2CO \leftrightarrows C + CO_2 \tag{1.21}$$

In figure 1.14 the measure temperature profiles of the solid catalyst surface, bed bulk and the calculated gas temperature are reported. Temperature is monitored using thermometry and radiometry methods; direct gas temperature measurements were not feasible, thus authors estimated the gas phase temperature through energy balances and empirical correlations developed in previous works [24], where temperature inside the fluidised bed was obtained thanks to an energy balance on a small volume of the bed, summarised as

$$(Q_g|_z - Q_g|_{z+\Delta z}) + (Q_p|_z - Q_p|_{z+\Delta z}) + Q_{MW} = Q|_{Lg} + Q_{Lp} \tag{1.22}$$

where meaning of symbols is reported in table 1.3; z and Δz represents the small volume boundaries. From the energy balance, the gas temperature was obtained as

Table 1.3: Terms of the energy balance [23].

Term	**Description** [°C]	**Mathematical expression**
Q_g	Heat transfer in the gas phase	$\pi\frac{D^2}{4}\rho_g U_g c_{P,g} T_g$
Q_p	Heat transfer in the solid phase	$\pi\frac{D^2}{4}\rho_p U_p c_{P,p} T_p$
Q_{Lg}	Convective Heat transfer by the gas phase	$(\pi D\Delta z)\varepsilon h_{gw}(T_g - T_w)$
Q_{Lp}	Convective Heat transfer by the solid phase	$(\pi D\Delta z)(1-\varepsilon)h_{pw}(T_p - T_w)$
Q_{MW}	Microwave Heat transfer	$q_{mw}(\pi\frac{D^2}{4}\Delta z)(1-\varepsilon)\rho_p$

$$\frac{1}{a}\ln\frac{T_g + \frac{b}{a} - T_w}{T_{g,0} + \frac{b}{a} - T_w} = z - z_0 \tag{1.23}$$

where a, b are constants that depends on the bed characteristics, gas velocity, heat transfer coefficients and microwave heat. In addition, no comparison with conventional heating methods is carried out.

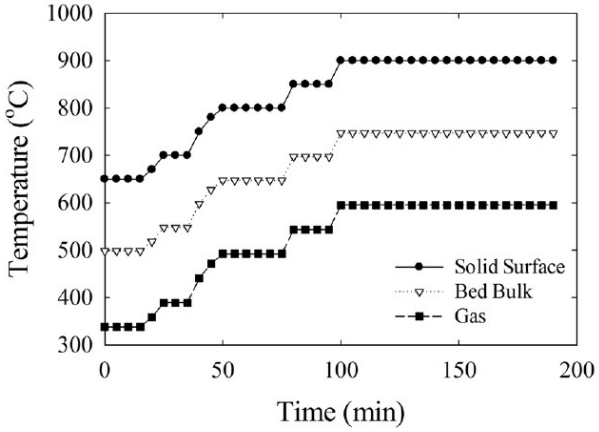

Figure 1.14: Temperature profiles of the solid catalyst surface, bed bulk and gas under MW heating [23].

With such catalytic system, authors found; high Methane and Carbon Dioxide conversions and high selectivity to both Hydrogen and Carbon Monoxide (essential for having a H_2/CO ratio close to 1), as shown in figure 1.15, prior to the catalyst deactivation due to coking.

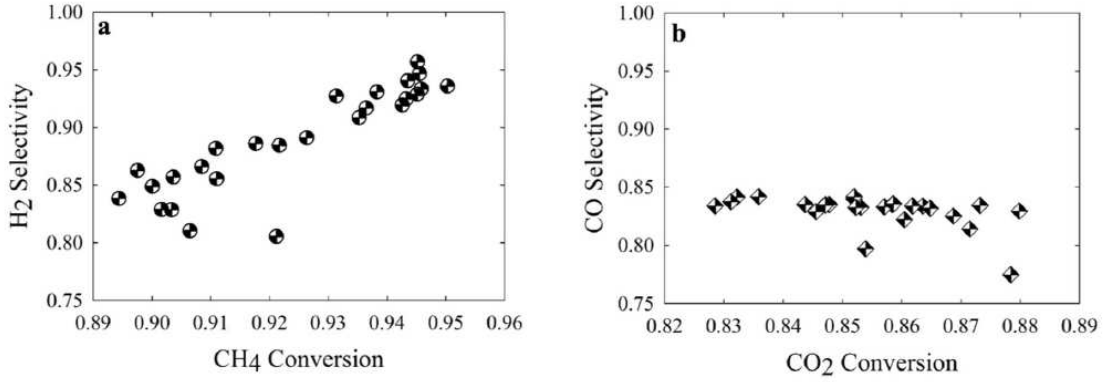

Figure 1.15: Selectivity of Syngas products plotted vs reactant conversions, parametric in temperature [23].

Hydrogen selectivity increase as methane conversion increase; this is interpreted as effect of temperature differences between catalyst and gas, as well as the high CO selectivity up with constant CO_2 conversion. Hydrogen selectivity diminished at high temperatures, due to the presence of the reverse WGS reaction; high temperatures lead to faster catalyst deactivations, directly related to the diminished H_2 selectivity. Carbon monoxide instead reached maximum selectivity close to 100% at 700°C; this was interpreted as effect of deposition of Coke on the catalyst, which pushed the Boudouard reaction toward CO production. Authors tested other catalytic systems in addition to the described $C - SiO_2$ system; one of the catalytic systems was based on Nickel, for which high performances were found.

1.2.3 B. Fidalgo, A. Domìnigues, J.J. Pis, J.A. Menéndez [19]

Fidalgo et al. investigated the DRM reaction over an activated carbon catalyst, which acts both as catalyst and MW receptor; comparison with conventional heating is carried out to compare the heating strategies. A single-mode MW cavity oven was used for the tests, where the catalyst sample was placed where the EM field intensity is maximum; the experimental setup is described in Figure 1.16. The reactor consist of a fixed bed; however, the outlet mixture is analysed by sampling at fixed time intervals the outflow gas mixture. Tests were conducted over a range of different operating conditions, reported in table 1.4, where each test is labelled, to identify the results in Figure 1.17. Conversions of Carbon Dioxide and Methane are higher under MW heating, as shown in figure 1.17. Authors explain this observation by considering the temperature differences between the gas and the catalyst particle, since gas is not able to absorb MW radiation. The single-mode MW heating device allowed for a more uniform temperature distribution in the bed, which resulted in

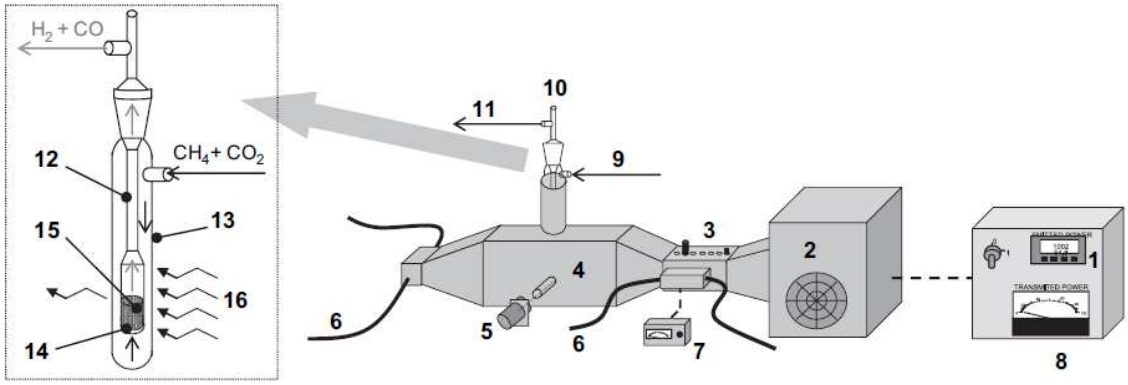

Figure 1.16: Schematic diagram of the experimental setup [19].

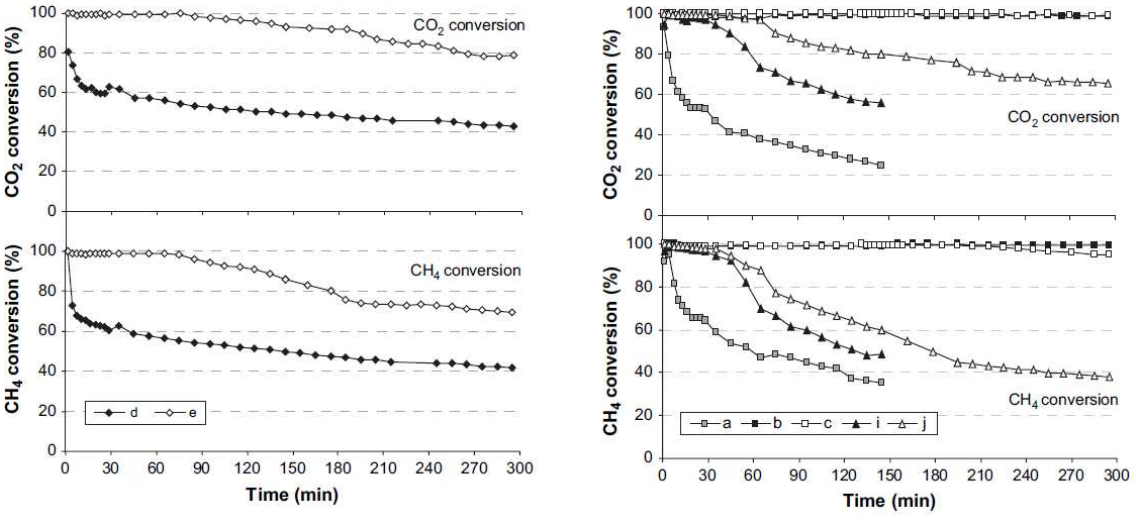

Figure 1.17: Effect of heating mode on the MDR reaction. Labels as in table 1.4[19].

improved performances. Authors speculate about presence of micro-plasma in the bed, due to the presence of hot spots. At 800°C, the theorised reactions used to explain the observed results are Methane Dry reforming, Methane cracking and the Boudouard reaction. In particular, coke deposition due to cracking is advantageous for the system, since gasification reaction allow to regenerate the active sites that has been blocked by coke. Methane Craking and the Boundouard reaction seems to be favoured by MW heating, which explains the enhanced conversions attained in other tests. The obtained H_2/CO ratio was unity. Authors investigated the effect of temperature on the systems, by studying the isotherms of 600°C, 700°C, 800°C and 900°C. At 900°C carbon deposition is much more enhanced in MW heating systems than in conventional systems; that's due to the enhancement of the Boudouard reaction under MW heating. In fact, coke deposition is much more intense in the MW heating system; in the electric furnace, no deposits were found. Carbon deposition is believed to originate outside of the catalytic bed, due to the contact of the feed mixture with the outside wall of the reactor; MW radiation may contribute to this deposition. The carbon deposits were investigated using Raman spectroscopy on the catalytic bed; such analysis indicate that not only amorphous carbon is generated,

Table 1.4: Conditions of the experimental campaign [19].

Test	**Temperature** [°C]	**Heating device**	**Time** [min]
a	600	MW	150
b	700	MW	300
c	800	MW	300
d	800	Conv.	300
e	800	MW	300
f	800	MW	300
g	800	MW	300
h	900	MW	-
i	700	MW	150
j	800	MW	300
k	800	MW	150

but also graphitic deposits are present. Graphite is a good electric conductor; when MW irradiate such materials, radiation is reflected back and not absorbed. Deposits of graphitic nature, therefore, prevent MW radiation from reaching the catalytic bed surface, with the obvious consequence of the inability of temperature control of the MW-heated system.

1.2.4 X. Zhang, C.S.M. Lee, D.M.P. Mingos, D.O. Hayward, [64]

Zhang et al. investigated the MDR process performances over different catalysts under MW heating, comparing the obtained results with conventional heating systems. The experimental setup used is a lab-scale packed bed reactor, placed in a cylindrical cavity to contain MW dispersions; temperature was monitored with optical fiber thermometers, whose tip was placed at the catalyst centre. Low-power MW generating device is used. Authors performed the DRM reaction under different operating conditions (see table 1.5) and then examined changes in catalyst conformation (through X-ray diffraction analysis) to detect evidences of hot-spots. It was found that the catalyst structure (for the $Pt/CeO_2/\gamma Al_2O3$ catalyst) was

Table 1.5: Conditions of the experimental campaign [64].

Process parameter	**Value**	**Units**
Temperature	$450 - 800$	$°C$
Pressure	1	bar
CO_2/CH_4 ratio	from 3 : 1 to 1 : 3	-
Total flowrate	60	mL/min
Catalyst mass	0.5	g
Maximum MW power	200	W

altered under MW heating, with formation of metallic alloys that would technically require temperature well above 1000°C to be formed, while tests were performed at maximum 800°C. The high temperature found locally on the catalyst structure

enhanced the reaction kinetics, leading to better performances of the MW-heated system if compared to the conventional heating system, even though both experiments were carried in the same temperature range.
Figures 1.18 show the comparison of Carbon Dioxide and Methane conversions with temperatures, measured at 50°C intervals. Microwave heating resulted in higher conversions, above the theoretical thermodynamic equilibrium value; the conversion difference between the experimental and theoretical data reduces with increasing temperature, with conversions above 80% over 700°C. The increased performances of MW heating were explained through the presence of hot spots, having a temperature significantly higher than the average bulk catalyst temperature. However, other non-thermal effects were theorised, by comparing these results with the ones from previous experiments [63], where X-ray diffraction analysis on the catalyst after the reaction confirmed the presence of hot-spots.

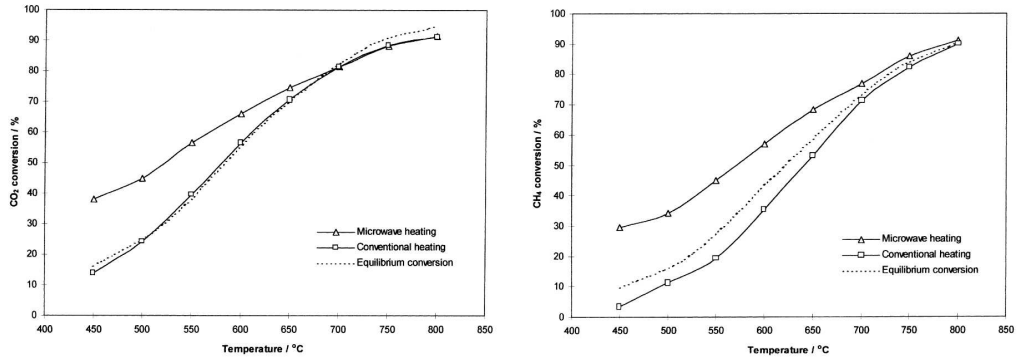

Figure 1.18: Conversions of Carbon Dioxide (left) and Methane (right) at different temperatures for MW heating, conventional heating and the theoretical thermodynamic value, for the catalytic system $Pt(8\%)/CeO_2(20\%)/\gamma - Al_2O_3$[64].

Product selectivity also resulted increased under MW heating at lower temperatures. This can be seen in figure 1.19, where the H_2/CO molar ratio is plotted against temperature. In general, the H_2/CO ratio increased with increasing temperature; however, MW heating shows higher performances for lower temperatures. Values of ratio under 1 suggest the presence of the Water-gas shift reaction, which lower the Hydrogen concentration at the reactor outlet. Analysis of equilibrium constants for the WGS, MDR and MSR reactions showed that the K_p increase of MDR reaction with temperature is much more pronounced than the other reactions; thus, high temperatures favour H_2/CO ratios equal to 1. Authors measured the input, reflected and absorbed MW power delivered to the catalyst sample; it was noted that, in order to increase the bed temperature, increased MW power is necessary. The relation between reflected and absorbed power is determined by the catalysts dielectric properties. For the catalytic system considered, the MW-absorption capacity decreased with temperature, since the reflected power increase more rapidly than the absorbed power at high temperatures, as shown by figure 1.20. Authors attributed the increased performances of MW heating compared to conventional heating to the presence of hot-spots into the material, rather than specific MW effect on the reaction kinetics.

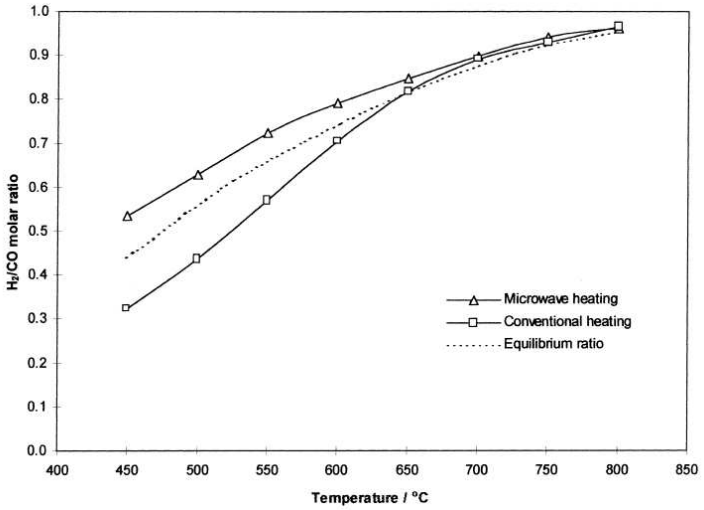

Figure 1.19: Selectivity as H_2/CO ratio over temperature, for the catalytic system $Pt(8\%)/CeO_2(20\%)/\gamma - Al_2O_3$ [64].

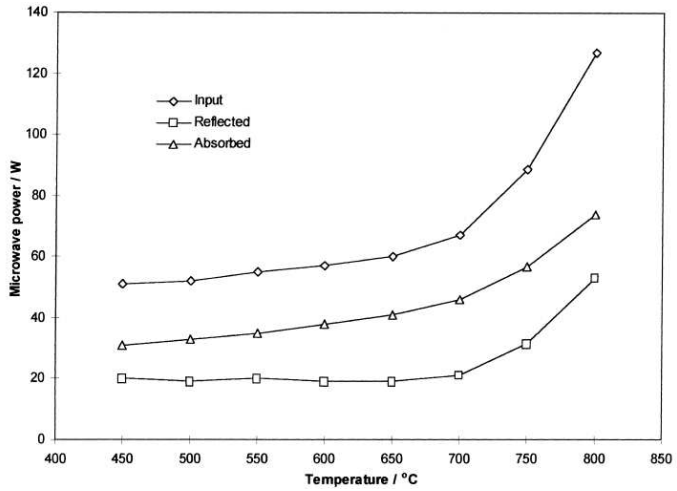

Figure 1.20: Input, absorbed and reflected power as function of temperature [64].

1.2.5 A. Ramirez, J.L. Hueso, M. Abian, M.U. Alzueta, R. Mallada, J. Santamaria [49]

A central effect of the MW heating mechanism is related to the uniqueness of MW selectivity toward the solid phase only, in gas-solid catalytic reactions. Research in gas-solid catalytic processes is typically aimed toward optimization of catalyst composition to achieve higher conversions and selectivities. However, an upper limit is always found; above a certain reaction temperature, gas-phase reactions become important, and their effect cannot be neglected. Consequently, impurities are always found. In this study, *Ramirez et al.* [49] applied the concept of MW heating to a catalyst-support ensemble capable of absorbing MW radiation. MW heating is applied to the reaction of CO_2 mediated oxidative dehydrogenation of isobutane; in conventional heated processes, the reaction present a complex pathway. Rather than employing a specific catalysts, authors chosen to exploit commercially

available catalyst (V/Al_2O_3) which was coated on a monolith of strong MW absorber material, that is, Silicon Carbide. The two different reaction pathways taking place in the homogeneous gas phase and on the V/Al_2O3 catalyst are reported below (eqs. 1.24-1.25).

$$iC_4H_{10} + CO_2 \xrightarrow{Gas\ \ Phase} iC_4H_8 + C_3H_6 + C_2H_4 + CH_4 \tag{1.24}$$

$$iC_4H_{10} + CO_2 \xrightarrow{V/Al_2O_3\ \ Catalyst} iC_4H_8 + CO + H_2O \tag{1.25}$$

Catalyst temperature was monitored using an IR camera (lateral monolith temperature) coupled with a pyrometer (temperature at the top monolith surface, corresponding to the exit gases). However, the gas-phase temperature could not be directly measured, since non-contact temperature measurement devices are not sensitive to the gas phase. Thus, the gas temperature was obtained from the gas-phase kinetic model; this indirect measurement method can be exploited only when a reliable kinetic model is available. The experimental campaign consisted in performing the reaction both in presence of MW and conventional heating. Under MW heating, selectivity of the reaction toward the desired product (isobutylene) resulted increased, while production of unwanted cracking products (propylene, methane, ethylene) was much lower; this effect was attributed to the much lower temperature of the gas phase if compared with the solid catalyst temperature. MW heating resulted lower in conversions; this effect results from the absence of secondary gas-phase reactions. In particular, the much lower gas-phase temperature is responsible for a diminished production of radical intermediates, responsible for formation of methane, ethylene, propylene and other minor by-products. Figure 1.21 shows the relation between selectivity, conversion and GHSV for both heating strategies.

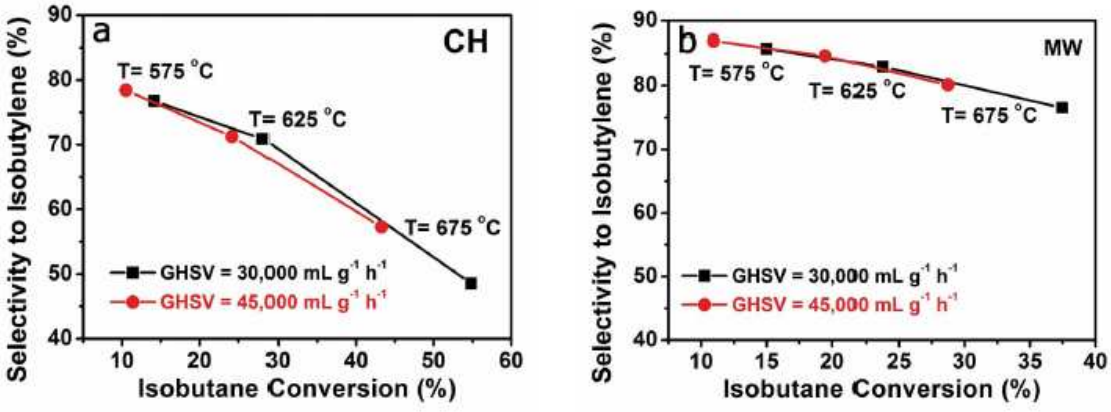

Figure 1.21: Influence of contact times on the Isobutane CODH reaction under conventional (left) and MW (right) heating. [49].

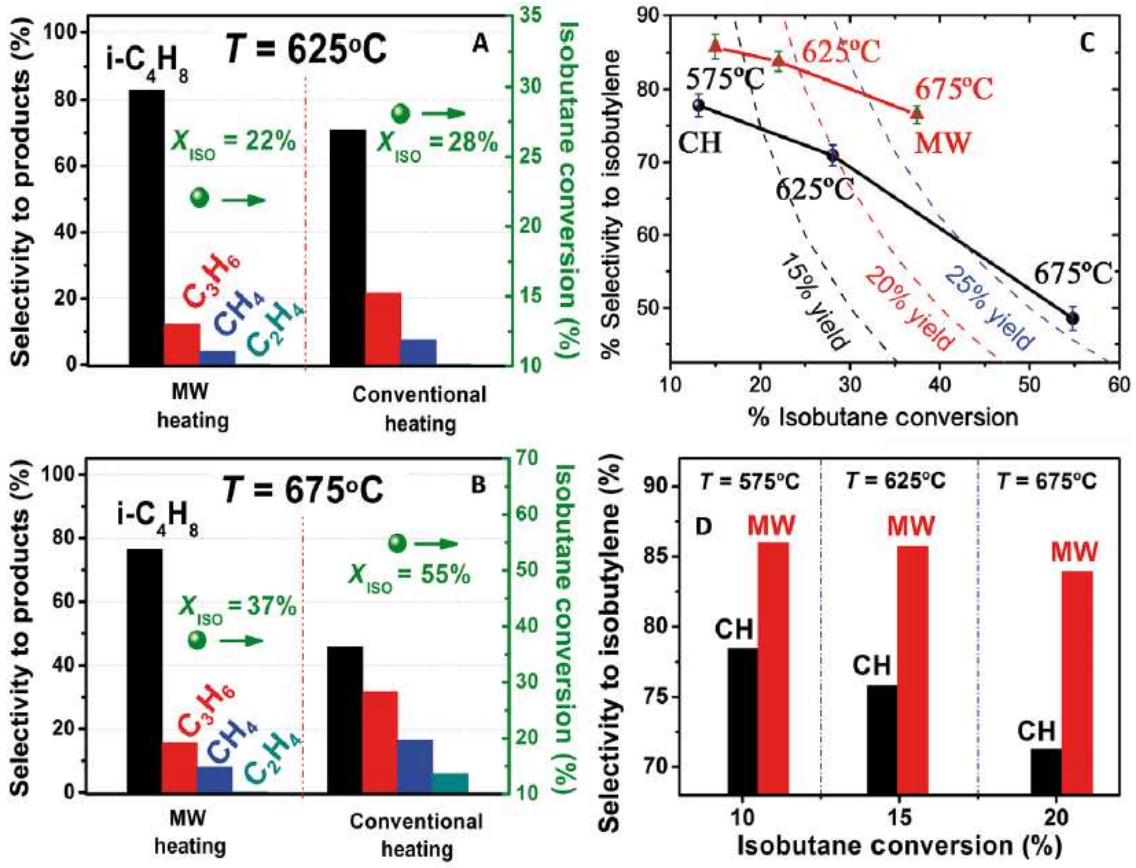

Figure 1.22: Comparative catalytic performance in isobutane CODH: (A, B) selectivity o products and isobutane conversion (solid green dot) at 625°C and 675°C; (C) selectivity-conversion plots (dashed lines represents equal yields); (D) evaluation of selectivity to isobutylene at different temperatures for equivalent conversion levels of isobutane. [49].

Figure 1.22 shows the comparison between the two heating systems, in terms of selectivities to isobuthylene and isobutane conversion for different temperature and GHSV. It is underlined that MW heating, as well as conventional heating, lead to catalyst deactivation due to Coke deposition on active sites; however, this effect is also present in conventional heating systems. After catalyst regeneration through a TPO, it is concluded that the use of MW heating systems do not impact on the catalyst performances. Finally, it is underlined that CO production is higher under MW heating; this effect is attributed to the enhancement of the Boudouard reaction, which seems to be more favorably driven under MW heating systems.

1.2.6 K. Sato, H. Luo, M. Miyakawa, M. Nishioka [50]

Sato et al. investigated performances and characteristics of different catalysts (different composition and active site loading) for both the dry and steam methane reforming reactions under MW heating, and compared the performances with conventional heating systems. In particular, the catalysts studied were $Pd/\gamma Al_2O_3$ (5% and 10% of both pure Pd and PdO) and $Ni/\gamma Al_2O_3$. The experimental set-up

consists in a catalytic fixed bed reactor, as shown in figure 1.23. The experimental parameters used in this study are reported in table 1.6.

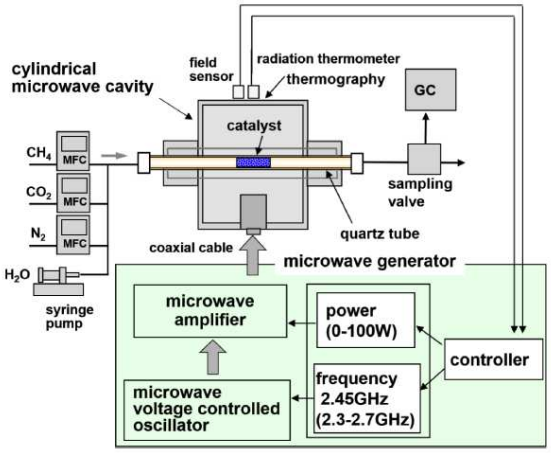

Figure 1.23: Schematic diagram of the MW reactor system.

Table 1.6: Conditions of the experimental campaign.

Reaction	**Feed flowrate** $[mL/min]$	**Reactant ratio**
MSR	50	$H_2O/CH_4 = 3$
MDR	50	$CO_2/CH_4 = 1$

Flowrates of both reactants and products are monitored using an online GC apparatus. The MW oven used in this case is characterized by low power capacity (100 W); moreover, a particular oven was used in this study, capable of producing and concentrating a standing wave (frequencies of 2.47 and 2.45 GHz were investigated), as to prevent non-uniform temperature distributions in the reactor. Three different aspects of the MW-assisted heating method are investigated:

- the possibility of employing a supported metal catalyst in their MW-heating system;
- the performance comparison between MW and electrical heating (via an electric furnace operating at different temperatures);
- investigate coke deposition on the catalyst under MW heating.

The MW system consist in a single-mode apparatus, where radiation is produced by a semi-conductor-type generator capable of providing a maximum power of 100 W. Temperature is measured through a radiation thermometer. The apparatus allowed to generate a standing wave having a peak of the EM field in the position of the fixed bed. Results of the study confirm the possibility of rapid heating of the catalyst, which in turn determine high activity; that's not an obvious conclusion, since metals are characterized by the tendency of reflecting MW. This effect increased with higher Pd loadings. Efficient heating is achieved thanks to the presence of finely dispersed nanoparticles of Pd on the highly porous support. Calcinated form

of the active metal (PdO) was found to be more susceptible to MW radiations, resulting in faster heating. In addition, it is noted how heating capacity of the catalyst is strictly related to the size of the finely dispersed active sites, decreasing when bigger agglomerates are used. Authors reported that under MW-assisted heating performances of both MSR and MDR processes resulted enhanced if compared with the conventional heating technique, as shown in 1.24. As expected, higher Pd loadings resulted in higher process' performances. In addition, higher conversions for the MSR reaction were measured at lower temperatures: the reaction started at approximately 330°C under conventional heating, while lower temperatures were recorded when using MW-assisted heating (280°C), suggesting a potential reduction in the reaction temperature (thus, consistently lower costs of the process). At the same temperature, the MW-assisted heating is capable of converting reactants more efficiently.

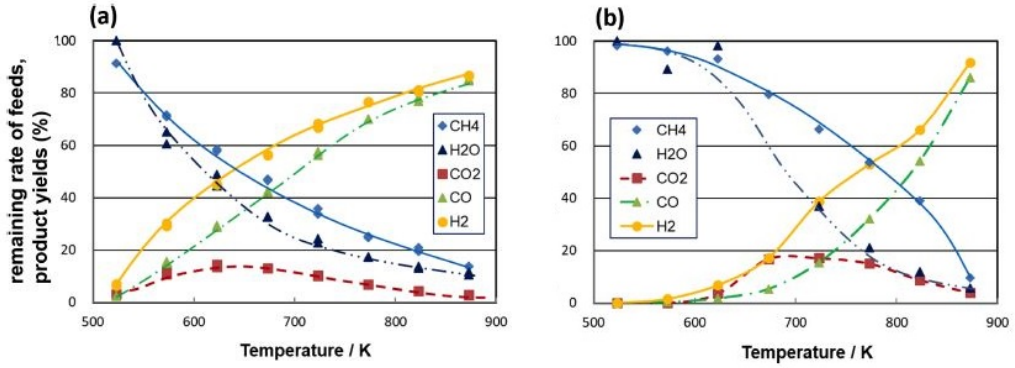

Figure 1.24: Comparison between components concentrations as function of temperature for MW-assisted Methane Steam reforming (left) and conventional heating (right) [50].

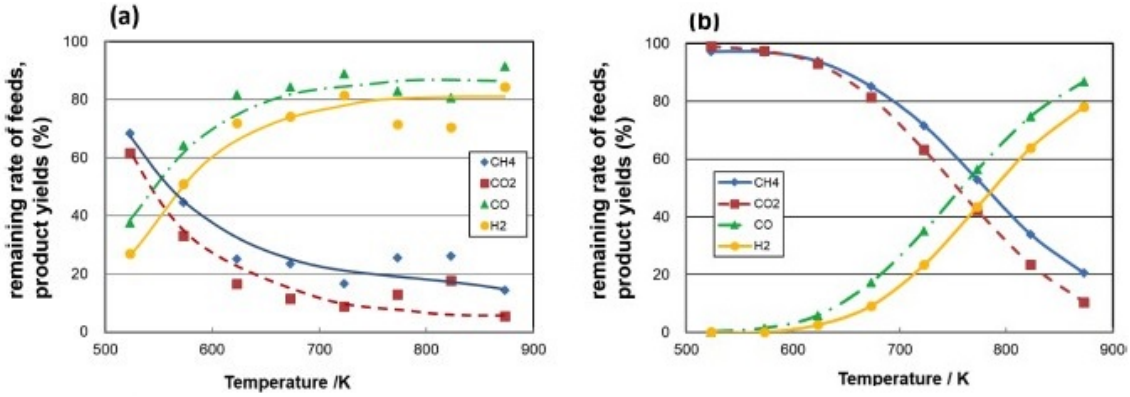

Figure 1.25: Comparison between components concentrations as function of temperature for MW-assisted Methane Dry reforming (left) and conventional heating (right) [50].

A successive thermo-gravimetric analysis showed that carbon deposition was limited in the case of microwave heating. As figure 1.26 shows, that's because pure car-

bon is a good microwave absorber, having loss tangent orders of magnitude higher than the catalyst support; local hotspots are therefore generated where carbon is deposited, providing suitable conditions for carbon combustion, resulting in stable catalytic activity.

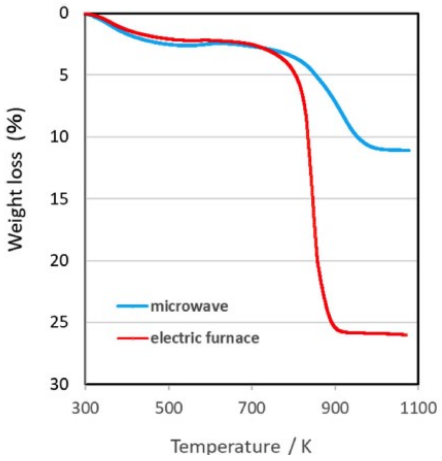

Figure 1.26: Thermo-gravimteric analysis of the catalyst used in the study [50].

1.2.7 S. Sharifvaghefi, B. Shirani, M. Eic, Y. Zheng [51]

Sharifvaghefi et al. studied the MDR reaction exploiting different $Ni - MgO$ based catalysts deposited on activated Carbon (chosen because of its high loss factor). Results obtained under MW heating were then compared with the conventional heating system. A schematic representation of both heating systems is reported in figure 1.27.

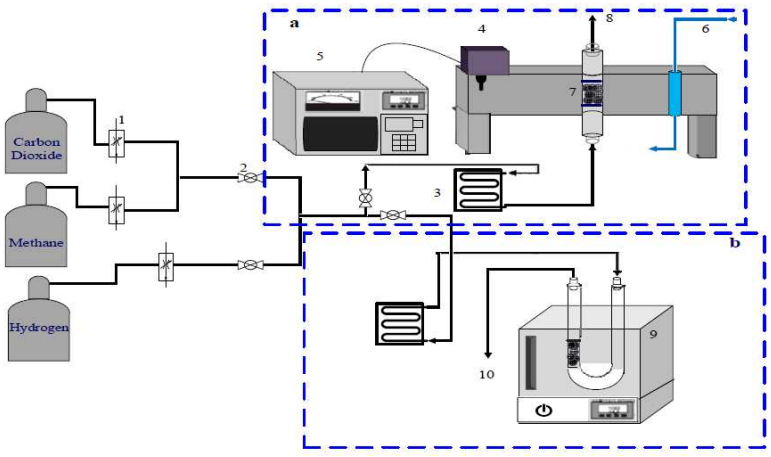

Figure 1.27: Schematic representation of both MW (**a**) and conventional (**b**) heating systems. [51].

Some important performance parameters are evaluated in this study, namely (i) conversion of reactants, (ii) Hydrogen selectivity, and (iii) energy efficiency of the process. Different catalytic systems were proposed (in terms of composition and

active component loadings). Conversion and selectivity were studied as function of temperature. Selectivity of products is here defined as eq. 1.26, while energy efficiency as eq. 1.27 (as suggested by *Durka et al.* [16]).

$$S_{prod|react} = \frac{N_{prod}^{out}}{\Delta N_{react}} \tag{1.26}$$

$$\epsilon = \frac{\Delta H_R^0}{\Delta H_R^0 + \sum N_i^{out} \int_{T_{amb}}^{T_{out}} C_{P_i}(T) dT} \tag{1.27}$$

Reactant conversions under MW heating resulted significantly enhanced. The most performant catalyst was found to be the $Ni/MgO/C$ system, having an intermediate loading of active sites (15%). Increasing the active site loading over this value does not result in an enhancement of the reaction, as shown by figure 1.28. Decreased catalyst performances with loadings over 15% are determined by active site agglomeration, thus, lower catalyst dispersion and catalytic activity. Addition of MgO to the catalyst promoted finer active site dispersions, resulting in increased performances. The H_2/CO ratio of the produced syngas is reported in figure 1.28. Higher temperatures favour the production of hydrogen with respect to CO; maximum selectivity is observed at 800°C with $Ni/MgO/C$ catalysts. It can be observed how the ratio follows the same trend as the conversion of the reactant for the catalysts. Reactant conversions and Hydrogen selectivity increases under MW

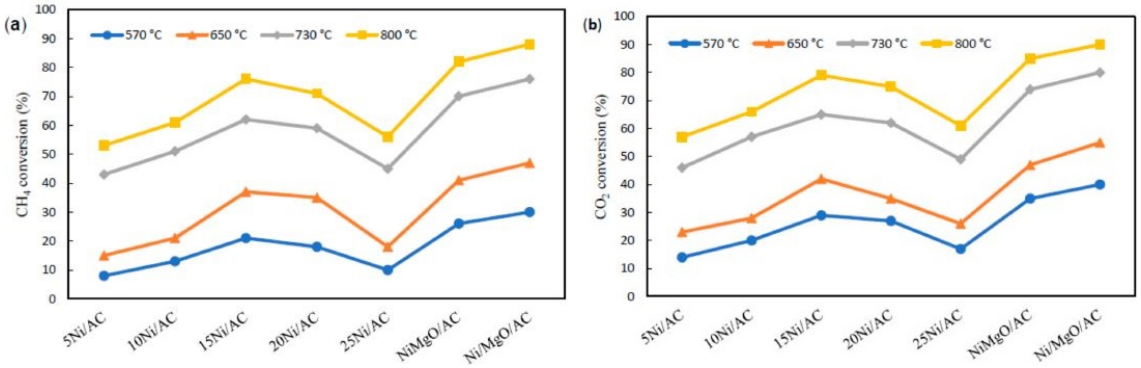

Figure 1.28: Performance of different catalytic systems in terms of CH4 conversion (left) and CO2 conversion (right) [51].

heating: at any operating temperature, the outlet gas approached equilibrium conditions under MW heating (Figure 1.30). Increased conversion under microwave heating can be explained considering that the energy is directly transferred to the catalyst surface. This result in higher temperature inside the catalyst, compared to the surrounding atmosphere temperature (near the catalyst surface). Authors speculate that localized temperature increases, resulting from the particular distribution of the EM field in the rector cavity, led to micro-plasma formation: due to higher temperatures, kinetic phenomena are enhanced, thus higher yields, conversions and selectivity are obtained. This is expressed in Figure 1.30, where reactant conversions and H_2/CO ratio are reported against temperature in the cases of conventional, MW heating and equilibrium conditions. MW heating enhances all such performance indices, resulting in above-equilibrium H_2/CO ratios at temperatures

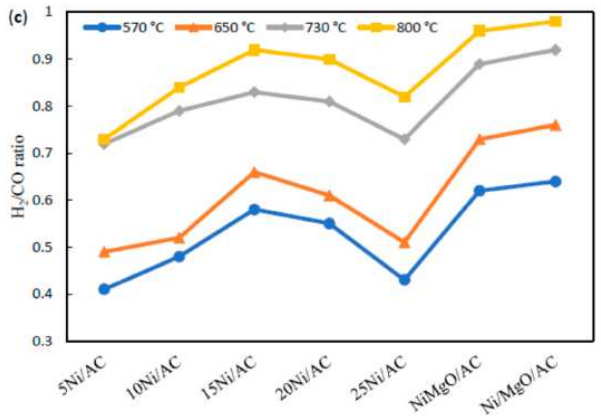

Figure 1.29: Performance of different catalytic systems in terms of H_2/CO ratio [51].

higher than 730°C: authors speculate that this effect can be attributed to a different kinetic mechanism than the one proposed by the authors, indicating that different kinetic pathways may arise from using MW heating; however, the effect may be traced back to wrong temperature measurements. Reaction pathways may be influenced by the presence of ionized atoms and molecules; plasma, in fact, may trigger different reactions from the ones used to evaluate the equilibrium composition, resulting in over-equilibrium conditions for the set of reactions considered. Energy efficiency is also increased under MW heating. Authors defined energy efficiency as the fraction of input heat that is actually used for the reaction, compared to the overall heat exchanged. This information was obtained by coupling an energy balance with thermodynamic information on the reaction enthalpy. The best results are obtained under the $Ni/MgO/C$ catalytic system: in addition, high reactant conversions are obtained in such condition.

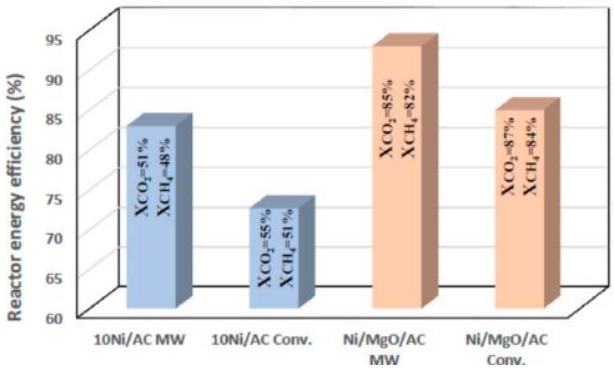

Figure 1.31: Performances of conventional and microwave heating, for different catalytic systems, in terms of reactor energy efficiency and reactant conversions [51].

Authors concluded that the higher performances shown by the MW heating system are due to the creation of hot-spots or micro-plasma over the active sites; this led to increased reactor performances, since the local temperature is higher than the average one.

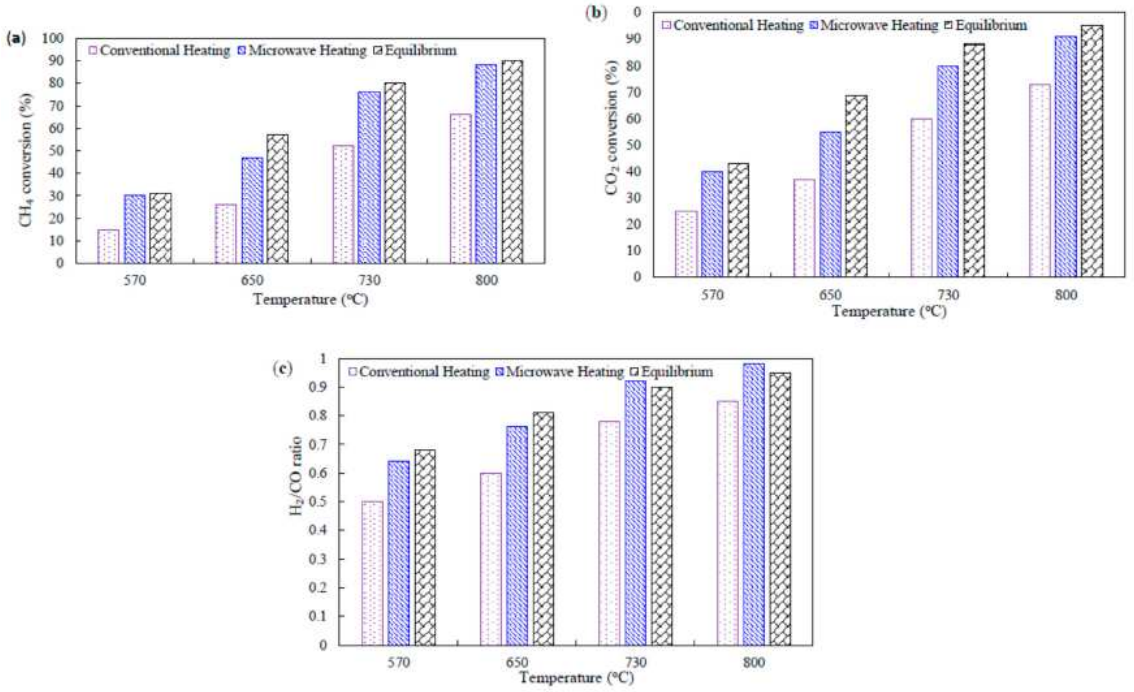

Figure 1.30: Comparison between conventional heating, microwave heating and equilibrium conditions for (a) methane conversion, (b) CO_2 conversion and (c) H_2/CO ratio. [51].

1.2.8 I. de Dios Garcìa, A. Stankiewicz, H. Nigar [14]

This article has been selected among others because authors implemented a Ni/SiC catalyst, the same one used in our experimental setup. In this paper performances of different catalysts are assessed, under varying conditions of:

- Microwave power;
- CH_4/CO_2 ratio in the feed stream;
- Space velocities.

Tests were conducted in order to determine the best catalyst, along with optimal operating conditions, as to maximize the hydrogen production. Contrary to the previous study, the experimental setup used here do not consist in a flow reactor: instead, a batch-type reactor was implemented (autoclave), characterized by a maximum power output of 400 W.
In particular, the Ni/SiC catalytic system studied here is tested with a CH_4/CO_2 feed ratio equal to 1, at temperature of 700°C and 800°C. with a space velocity of 11 $L/g_{cat}h$. Under this experimental configuration, after the 6 hours residence time, higher reactant conversions were measured (after 6 hours of batch time, methane conversion was 80% at 700°C, increasing to 90% at 800°C), significantly higher than other catalytic system. Conversion of CO_2 resulted significantly higher than the one of CH_4, suggesting an active role of solid C in the reacting system, involved in the gasification reaction with CO_2. The latter effect was significantly less

pronounced with other catalysts, particularly with the ones based on $\gamma - Al_2O_3$, which is supposed to delay the coke deposition. Moreover, homogeneous temperature distributions were measured using the SiC-based catalyst. Figure 1.32 shows the conversion profile of both CO_2 and CH_4, evaluated at the reaction temperature of 800°C, sampled at time intervals of 1 hour. It can be seen how the H_2/CO ratio decrease in time, due to the presence of the Boudouard reaction (Coke gasification, $C+CO2 \leftrightarrows 2CO$); however, the power supplied remained stable, resulting in a more controllable operation.

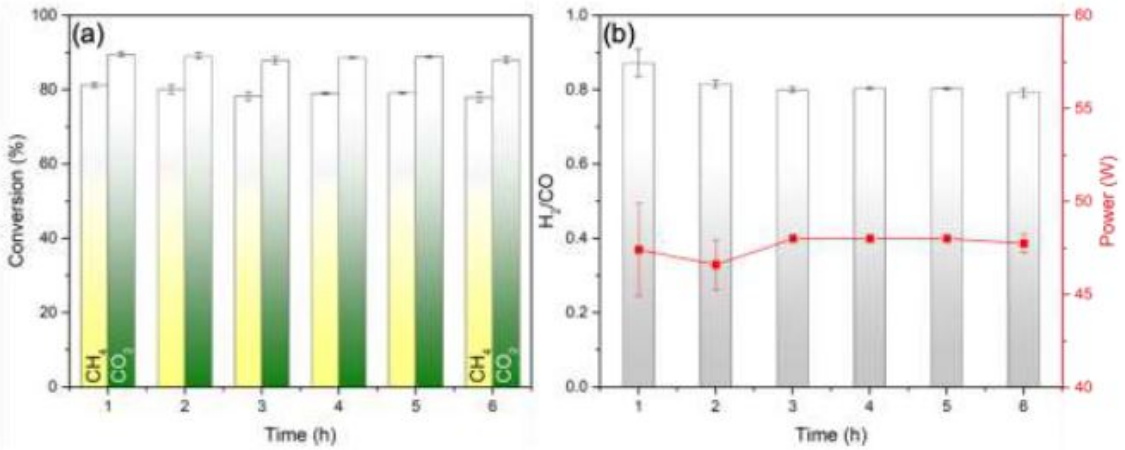

Figure 1.32: Catalytic performance of Ni/SiC at 800°C in terms of CH_4 and CO_2 conversions (left), H_2/CO product ratio and power consumption (right) for the MDR process [14].

Since the Ni/SiC catalytic system show higher reactant conversions, homogeneous temperature distributions, authors continued to study that system at 800°C, under different operating conditions, as to determine the optimum conditions which maximize the hydrogen production. In particular, it is discussed how the feed reactant ratio CO_2/CH_4 influences yield and energy consumption. Higher CO_2/CH_4 ratio increased the catalyst stability: that's because of the aforementioned gasification of coke, enhanced by increasing the CO_2 concentration. In addition, high ratio increased the conversion after the batch time; CO_2 conversion, however, changed with time due to the competition of the coke gasification with the dry reforming reaction. Using CO_2/CH_4 ratios equal to 2 resulted in longer catalyst lifetime, since the coke deposited is significantly consumed by the gasification with CO_2. However, using higher ratios implies higher power consumptions: that's because the coke gasification reaction is highly endothermic, increasing the power requirement of the MDR reaction.

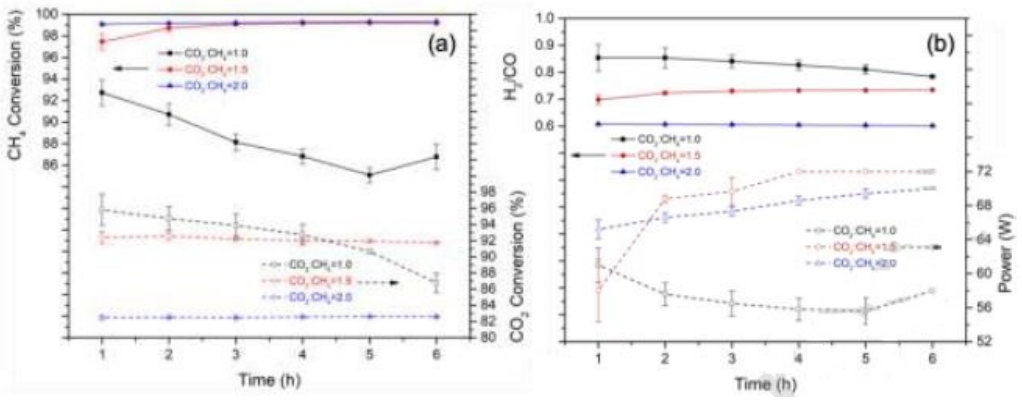

Figure 1.33: Influence of the ratios of CO_2/CH_4 in the conversions of CH_4, CO_2 (left) and supplied microwave power input and H2/CO ratio (right) [14].

Finally, the effect of the space velocity was assessed on the SiC catalytic system, under the operating conditions of 800°C and a feed ratio CO_2/CH_4 of 1.5, identified as optimal operating conditions from previous analysis. It is observed how the reactant conversion decreased (almost linearly); however, high conversions were still achieved (93% of CH_4, 88% of CO_2) at high WHSV values.

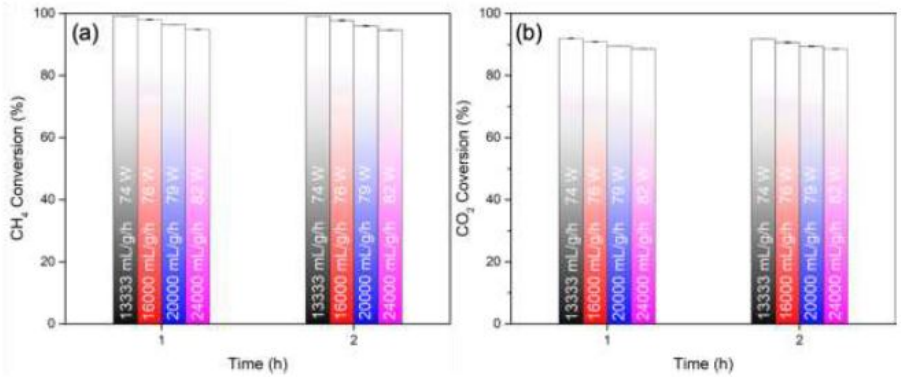

Figure 1.34: Influence of the space velocity on the conversion of CH_4 (left) and CO_2 (right). [14].

Conversions of both methane and carbon dioxide were found to decrease almost linearly when the GHSV is increased; in particular, doubling the feed flowrate (from 13.3 $L/g_{cat}h$ to 24 $L/g_{cat}h$) decrease the methane conversion after (1 hour of residence time) from almost 100% to slightly above 95%. From the author's analysis, it is concluded that the feed flowrate does not impact the process performances.

1.3 Literature survey on Syngas catalytic production via Methane Steam reforming with Microwaves

In the following section, articles where Syngas is produced via the MSR reaction are discussed.

1.3.1 D. Czylkowski, B. Hrycak, M. Jasinki, M. Dors, J. Mizeraczyk [13]

Academic research has not only focused on the catalyst type, but also catalyst-free systems were studied, as to allow for significant cost reduction of the MSR process. Particular interest has gained the plasma-based technology, where plasma (ionized atoms) is used to perform the high-temperature reaction. In this paper, a patented plasma source (able to generate plasma of several kW of power, using the MW frequency of 2.45 GHz) is used to determine the effectiveness of H_2 production via MSR. A particular aspect of the study is that high gas volumes are processed (circa 9000 NL/h), contrary to other lab-scale experimental studies: this allow to study the process efficiency at higher production scales. The experimental apparatus used is reported in Figure 1.35; it consist of a single-mode applicator, where MW are generated by a magnetron.

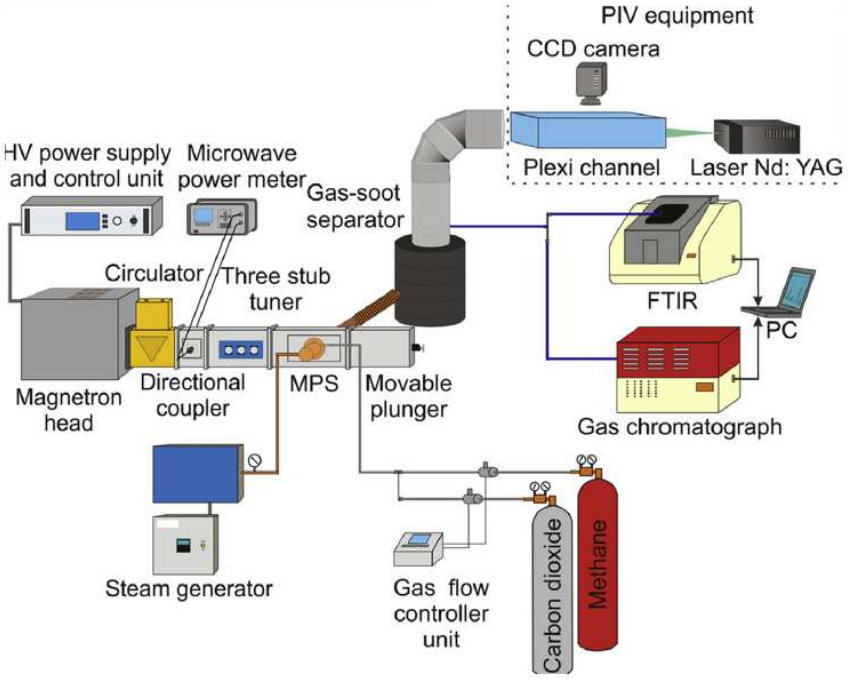

Figure 1.35: Scheme of the experimental setup used by the authors [13].

Plasma can be generated almost instantaneously, leading to significant reduction of start-up time. The study identifies the conventional steam reforming process as a benchmark for comparison of alternative processes; in particular, it defines some

comparison parameters, namely (i) Hydrogen production rate, (ii) the process' energy yield, (iii) Methane conversion and (iv) Hydrogen concentration in the outlet gas. The MSR process based on plasma can be competitive with other conventional H_2 production processes like Methane pyrolysis or dry reforming. However, it must be noted how the fluid-dynamic condition of the fluid (inlet nozzles) affects the process performances, as well as the power supplied by MW. Hydrogen concentration increased when high MW power are implemented, but the energy yield slightly decreased. Increased hydrogen production are associated with increased electric field in the plasma region with increasing MW power delivered to the system, which induces higher heat transfer capability of the plasma toward the surrounding gas. Hydrogen production through MSR under conventional heating techniques is one of the most energy-efficient way, resulting in 60 g/kWh; using MW-induced plasma, such value is about 42.9 g/kWh, suggesting that further optimization could increase the energy efficiency of the process. The best results in terms of H_2 hourly production were fixed in 192 g/h.

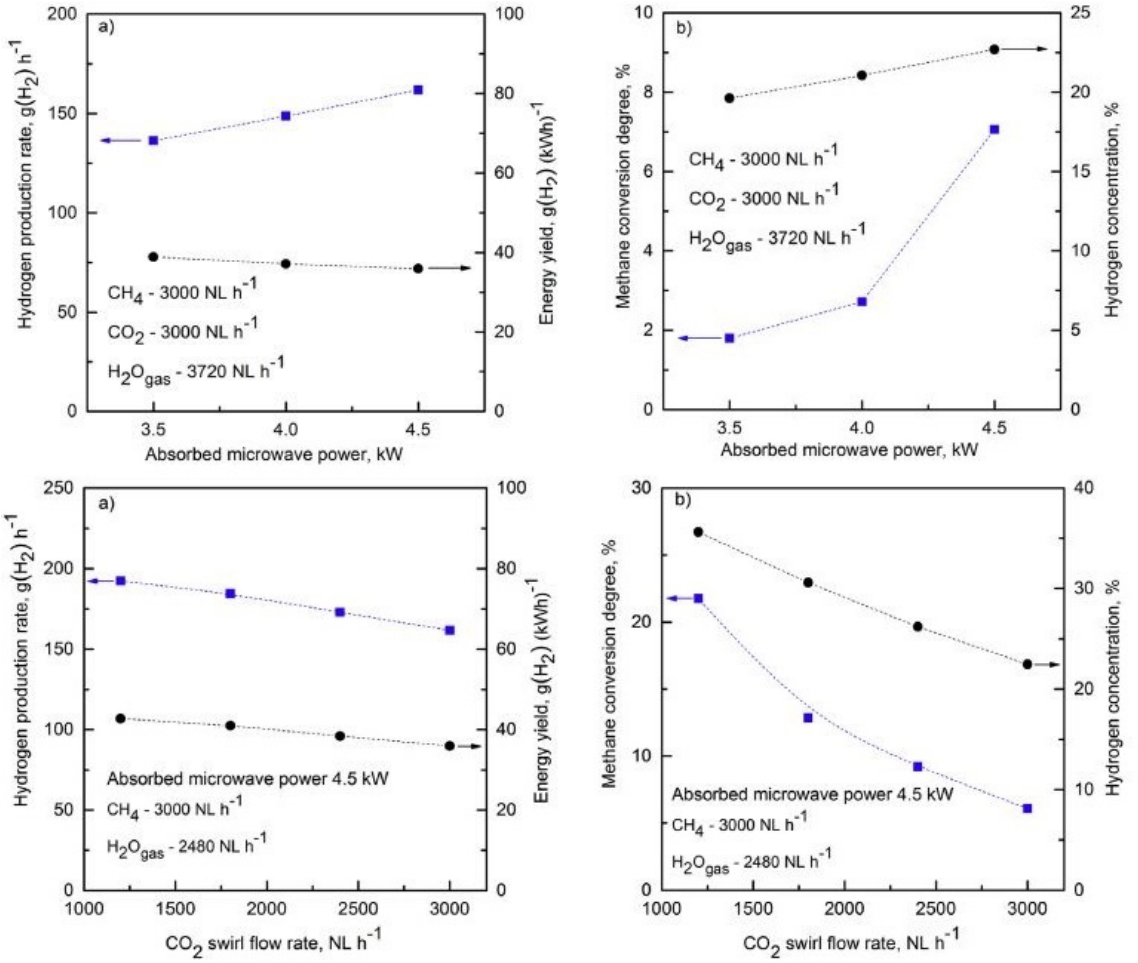

Figure 1.36: Influence of the absorbed MW power (up) and CO_2 flowrate (down) in the H_2 production flowrate and energy yield (left), and CH_4 conversion and concentration H_2 (right). [13].

1.3.2 N.M. Alawy, G.H. Pham, A. Barifcani, M.H. Nguyen, S.Liu [4]

Catalysts are used to lower the reaction temperature of the reforming reaction, enhancing the activity of reactants; however, they are often very costly, and have short lifetime, since the reforming reaction can lead to formation of coke nanoparticles (due to methane cracking reactions), which deposit on the catalyst surface, hence deactivating it. Such problems could be avoided by using plasma, which can be induced by microwave radiation: moreover, the radiative energy transfer is rapid and produces uniform temperature distributions in the reactor (without the need of using electrodes), allowing for high plasma density and therefore high reaction rates. In this study, the authors investigate on the combination influence of some process parameters on the H_2/CO ratio obtained using the plasma technology, under MW irradiation at atmospheric pressure. The parameters studied are (i) steam concentration, (ii) total feed flowrate, and (iii) the Input MW power. The study is performed for both the dry and steam reforming reactions of methane; however, it was chosen to report only results concerning the steam reforming reaction. Under conditions of constant feed flowrate, microwave input power, CO_2/CH_4 inlet ratio, the inlet steam concentration on the system has huge impact on the process performances. It can be seen from Figure 1.37 that increasing the inlet steam concentration lead to increased: (i) methane conversions, (ii) selectivities to H_2 and CO, (iii) yield of H_2 and CO from CH_4, and (iv) H_2/CO ratios. Enhanced process performances were associated with an increased concentration of radical species (like $H\cdot$,$OH\cdot$,$O\cdot$), responsible for the reactions of oxidation and reduction.

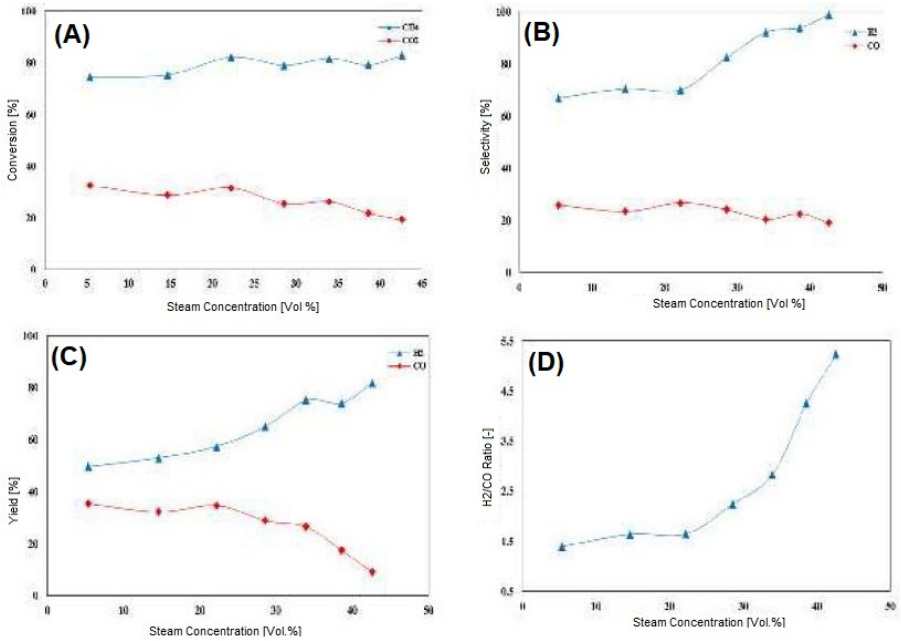

Figure 1.37: Effect of the inlet steam concentration on the Methane conversion (a), Selectivity to H_2 and CO (b), Yield to H_2 and CO (c) and on the H_2/CO ratio (d) [4].

The effect of inlet feed flowrate depends on the process considered: if in the methane dry reforming reaction increasing the feed flowrate results in lower process performances (lower conversions, yields, selectivities), when dealing with the methane steam reforming reaction, authors found increased conversions, yields and selectivities, as can be observed from Figure 1.38 and Figure 1.39. Despite the fact that, at higher flowrates, the inlet feed receives lower energy per unit mass, authors attributed the higher performances to the presence of $OH\cdot$ and $H\cdot$ radicals, which inhibits the reaction of methane recombination, favouring instead the formation of radicals like $CH_3\cdot$ and other species.

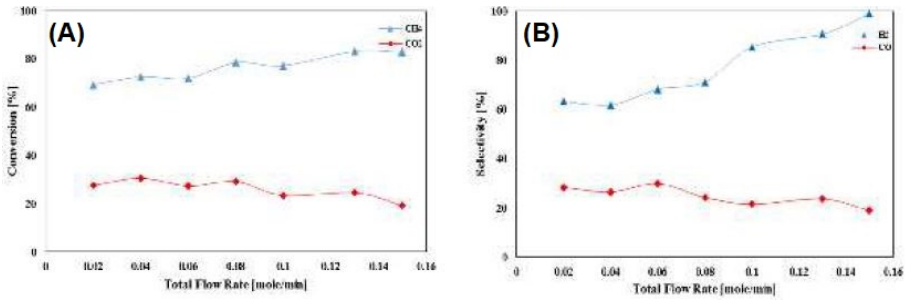

Figure 1.38: Effect of the total feed flowrate on (a) Conversion of CH_4, CO_2, (b) Selectivity of the process to H_2 and CO [4].

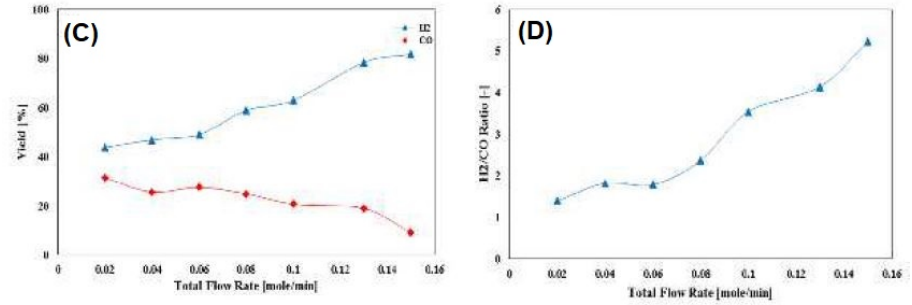

Figure 1.39: Effect of the total feed flowrate on (c) Yields of Hydrogen and CO, (d) H_2/CO ratio [4].

Chapter 2

Materials and Methods

This chapter describes the experimental setup and the instruments used in the experimental campaign carried out in the laboratory. Tests were performed to asses the feasibility of microwave heating of gas-solid catalytic reactions in a modified, commercial oven, to compare with the results obtained under conventional heating (i.e., electric heating). Differences between the two setups were minimized, to evaluate the most significant performance indices of the systems under equivalent conditions. Due to the inherent differences in the heating technologies, an exact comparison is almost impossible. In the following paragraphs the two experimental setup are presented. Both setups can be divided in three main sections; a feed section, a reaction section and a measurement section. The feed and measurement sections remain unchanged in both heating systems. In Figure 2.1 the schematic configuration of the experimental setup is reported; the reaction section generally identify the microwave oven or the electric oven, depending on the test considered.

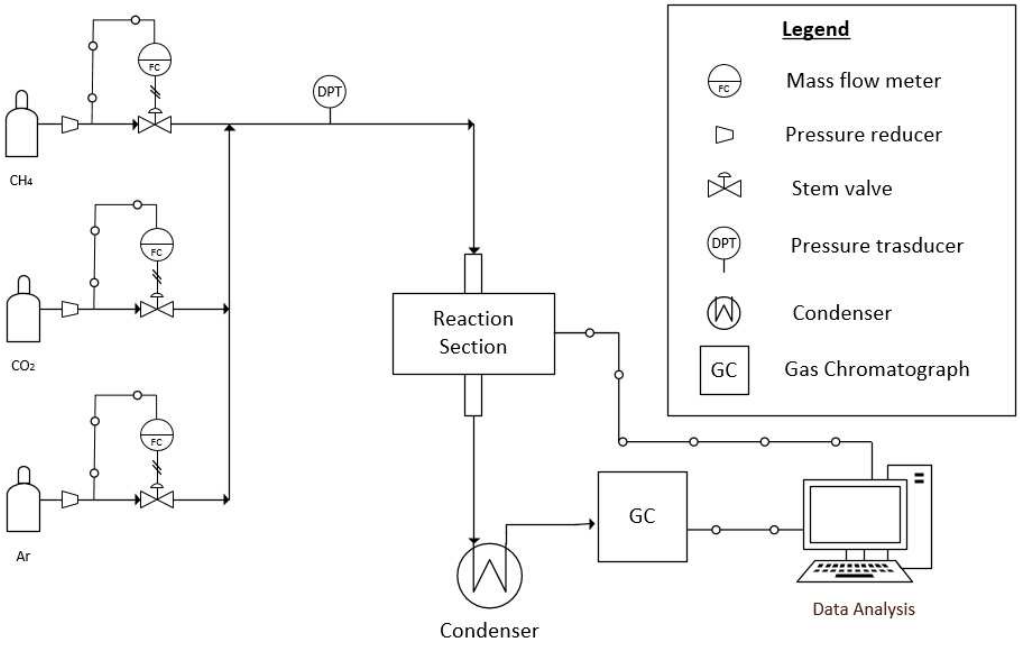

Figure 2.1: Schematic representation of the experimental setup.

2.1 Feed section

The gaseous mixture used as feed is composed by an equimolar mixture of Methane and Carbon Dioxide plus Argon, used as tracer for quantitative analysis of mixtures of unknown moles (or volume) variations. Feed composition is reported in Table 2.1.

Table 2.1: Composition of the feed mixture used in the experiments.

Species	**Concentration**
CH_4	47.5%
CO_2	47.5%
Ar	5%

All gases are available in cylinders, initially at 200 bar; in order to reduce such pressure down to 1 bar, a sequence of pressure reducers is implemented. A first step lowers the pressure from 200 bar to 50 bar; then, a second step further reduce the gas pressure to 5 bar. At this point the gas enter into the mass flow meter (described in detail in section 2.1.1), controlled by a dedicated software, and its pressure is further reduced to atmospheric pressure. Connection between the flow meter and the reaction section is guaranteed by polyamide tubes. The operating parameters used in both tests are listed in Table 2.2. An inherent difference between the two setups is

Table 2.2: Operating parameters for the gas feed used in both tests.

Parameter	**MW heating**	**Electric heating**	**Units**
GHSV	20195	20015	h^{-1}
WHSV	14.8	14.17	$mL\ mg^{-1}\ h^{-1}$
Total Flowrate	342.6	254.65	$mL\ min^{-1}$
Catalyst mass	1.386	1.077	g
Bed height	2	1.7	cm

determined by the transient period that is required to reach the isotherm. Microwave heating is characterised by a very fast ramp; the temperature set point imposed by the controller is generally reached in less than a minute. However, the conventional heating system requires longer transients, since the maximum temperature ramp is $25\,°C/min$ due to instruments limitations and heat transfer limitations in the reactor and oven. In order to limit coke deposition on the catalyst during this period, to preserve catalytic activity, in conventional heating it was chosen to close the Methane and Carbon dioxide fluxes during transients (required to reach the temperature set point imposed), feeding only the inert.

2.1.1 Mass flow meters

Gas flowrates are controlled by Brooks and Bronkhorst mass flow meters; control is based on the by-pass measurement principle, where a ΔT between a heated section and a capillary tube is exploited to obtain the volumetric flowrate. In particular,

temperature is measured before and after an electrical resistance; when the flow crosses the wire, it heats up bringing its temperature to a known value. Flowrate of single gasses is calculated from this temperature variation of the fluid between the two probes. Those mass flux meters can control the flowrate of a wide variety of different gasses; calibration of these instruments is performed referring to a single gas, namely Nitrogen, and then corrective factors are used for each gas. Mass flowmeters are represented in Figure 2.2. The flowmeters are operated through dif-

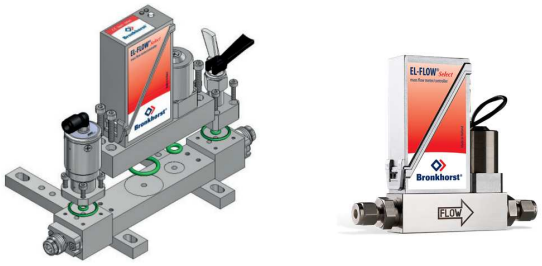

Figure 2.2: Bronkhorst mass flow meter.

ferent boldsymbol. DDE (Dynamic Data Exchange) commands are used to allow bidirectional connection between flowmeters and Windows applications. Depending on the type of mass flowmeter (Brooks and Bronkhorst), software products are distinguished respectively in SmartDDE and FlowDDE. These boldsymbol handle all communications to the instruments and provides the data to the Microsoft Excel and LabVIEW applications. Control of the flow parameters from Microsoft Excel is done through specific connections that make it communicate with SmartDDE; control through FlowDDE is instead instead performed through the interfact buolt in Flowview or Flow-Bus, which is used as direct control of value exchange between instruments and PC. Specifically, the computer used to control the mass flowmeters is PC-Flux, on which Windows 11 is installed. For the mass flowmeters controlled through Excel, the operating procedure required to obtain the desired mixture composition consist in first calculating the set points of each gas; this operation is automatically performed by the spreadsheet. The flowrate is then checked manually; to do so, a bubble flow-meter is used. In particular, the time required for the bubble to travel through a given volume is measured; the volumetric flowrate is then obtained by converting dividing the volume by the time measured. The set point is then manually adjusted as to obtain the desired flowrate. Once the procedure is repeated for all the gaseous species, the mixture is obtained by conveying all the species in static mixers, and transported using Polyamide or PTFE tubes.

2.1.2 Pressure trasducer

Two pressure transducers were used in the experimental setup; one to monitor pressure drops across the bed, and one for the air thermometer. The transducers have different measurement range (expressed as gauge pressure); in particular, the one used by the thermometer has a measure interval of $0 - 5$ *bar*, while the one used to monitor pressure drops $0 - 1$ *bar*. The working principle is the same for both instruments.

Before entering into the reaction section, pressure is monitored and compared to its atmospheric value. This comparison, useful to monitor the amount of carbon deposited on the catalytic bed during the reaction, is performed by the pressure sensor MPX5010DP build by NPX, depicted in Figure 2.3. It consist in a piezore-

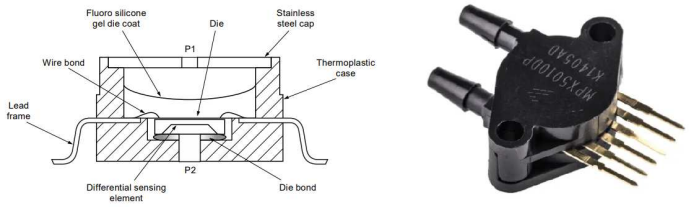

Figure 2.3: Honeywell Pressure Trasducer MPX5500DP and its scheme.

sistive trasducer, which exploits the piezoresistive effect to detect the applied gauge pressure difference with respect to the environment. When pressure is applied, the semiconductor or metal embedded into the sensor change its electrical resistivity; from this change it is possible to determine the value of pressure applied. With this type of pressure transducer, the gauge pressure range that can be analysed is $0 - 5$ *bar*. The pressure trasducer is connected to the feed line by means of a three-way quick release connector; the signal generated by the trasducer is acquired and processed through Matlab. To do so, an executable file is used; this executable file allows to acquire both temperatures from thermocouples and analog inputs. The program is found on the *PC-SR* computer, under the path "C:/Dati/TAI"; the method file is called "TAID4.met", while the executable file is called "TAID4.exe". The pressure transducer used by the thermometer is instead powered via an USB connection with a PC. The USB cable feed the transducer with a 5 V DC current. When a differential pressure is detected, the output voltage produced is acquired by a *PicoLog* instrument, which allow to record the signal's profile in time. The output file is stored in a dedicated software.

2.2 Reaction section

The dry reforming reaction was carried out in both heating systems; it is necessary to separately describe the Microwave heating systems and the conventional heating system. The temperature policy exploited in the tests is focused on studying how the two systems behave at different isotherms, namely 500°C, 600°C, 700°C, 800°C and 900°C. Once reached, temperature is maintained for all the time necessary for the gas chromatographic measures to be stabilised, when possible; in fact, during the reactions, some isotherms were characterised by very long transients, and it was necessary to stop the measurement before stabilization was achieved.

2.2.1 Vibratory sieve shaker

Both SiC and catalyst are available in a coarse form; in order to be formed into a fixed bed, they need to be grind down to the granulometric class that is chosen

(namely, $850 - 100\ \mu m$), and then the different particles must be separated, as to obtain a homogeneous particle dimension. This separation is performed into a vibratory sieve shaker, a device that exploit vibrations and several sieves with different opening to separate the grind particles of solid, represented in Figure 2.4. Separation was performed by using two sieves, having openings of 1 and 0.85 mm

Figure 2.4: Vibratory sieve shaker used for sieving the grind SiC and Catalyst.

respectively; separation was complete after 5 minutes of operation of the vibratory sieve shaker.

2.2.2 Reactor and Fittings

The extremes of the quartz reactor are closed with two junctions of the type reported in Figure 2.5. They consists of a steel cube with a steel thread cylinder. The cube is perforated and three holes are joined in a T shape; one opening allows the gas to flow in and out of the quartz tube, while the other two openings allows the passage of a thermocouple. The system of o-ring, ogive and hex nut prevent gas leakages and infiltrations, thus allowing for mechanical seal.

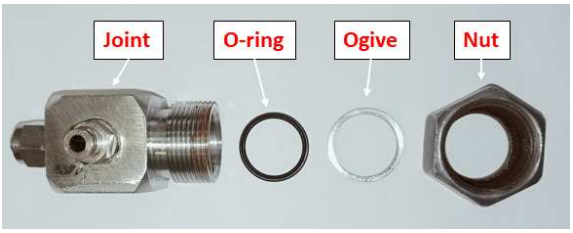

Figure 2.5: Fittings used to prevent leakages from the reactor

Materials used in the reaction section under microwave heating must be carefully chosen as to minimize interactions with the electromagnetic field. Conventional reactors, typically built from metallic alloys, cannot be used since electrons in the material tends to move accordingly to the oscillating electric field, generating hazardous electric currents in the upper layers of the material. In addition, the material must be resistant to high temperatures, required for the reaction to occur. A convenient material, characterized by low dielectric constant and resistance to high temperatures is quartz, having a melting temperature of 1670°C and a dielectric

loss tangent of $6 \cdot 10^{-5}$ (for comparison, SiC has a loss tangent of 5.28 [56], four orders of magnitude higher). Available quartz rectors have an internal diameter of 20 mm and a length of 600 mm. Gasses are injected in and withdraw from the reactor by using custom fittings; leakages are prevented thanks to a system of o-ring, ogive and hex nut. The reactor is shown in Figure 2.6.

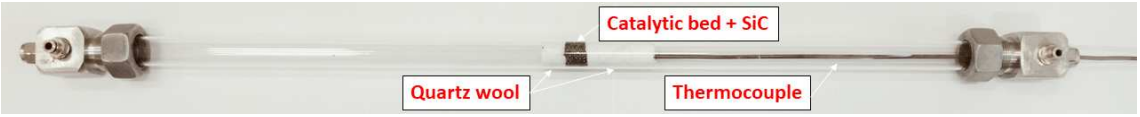

Figure 2.6: Reactor used for the reaction. A type K thermocopule control the bed temperature.

The reactor is configured as a fixed bed, where catalyst used to perform the reforming reaction belongs to the Katalco 25-4™ series, produced by the Johnson Mattew™ company. This tpe of catalyst is commonly used to reform a wide variety of feedstock molecules [1]. It is composed by a support of Calcium Aluminate, on which NiO is deposited. Catalyst composition is reported in Table 2.3 [20]. Due to

Table 2.3: Composition of the JM's catalyst Katalco 25-4™

Support	NiO wt%	K_2O wt%
$CaAl_2O_4$	18	1.8

its ceramic nature (low loss tangent), the catalyst's support is not able to absorb microwave radiation; therefore, it has to be mixed with a solid able to undergo dielectric heating. Such material has been identified in Silicon Carbide (SiC), due to its high chemical and thermal stability, coupled with relatively high loss tangent. Active sites are made up of metallic Nickel; the catalyst has to be reduced before its use in the reactor, due to the spontaneous oxidation to NiO in air. This process is performed right before the reaction, in a controlled Temperature Programmed Reduction program (TPR) using the same reactor. The reducing agent of TPR is Hydrogen, which is fed to the heated reactor along with an inert (typically Nitrogen). As Nickel Oxide reduce to metallic Nickel, Hydrogen is consumed; the operation continue until there's no more variation in the Hydrogen flowrate coming out of the reactor, since all the catalyst has been reduced. Then, the reactor is placed under inert atmosphere to preserve the catalyst from oxidation, until the beginning of the test. Metallic catalyst particles, as well as the metallic thermocouple, can generate sparkling if exposed to MW radiation; thermocouple grounding is therefore required to avoid such events, which affects the structural integrity of the system and the correct operation of the temperature probe. The reactor passes through the oven cavity in a vertical arrangement. The position of the reactor in the oven cavity was determined in a previous thesis work [18], through modelling of the electromagnetic field. However, it has to be noted that the EM field distribution is modified by the presence of objects into the cavity, like the metallic thermocouple (which was not included in the study) and the fixed bed dimensions; thus the EM field may be different from the predicted one. To obtain a fair comparison between

the two heating systems, the reactor structure (Quartz tube and thermocouple position within the bed) is maintained constant in both tests. However, the mixture of catalyst and SiC is prepared from fresh catalyst in each new test, to preserve its original catalytic activity; in fact, if local hotspots are present under MW heating, catalyst sintering may be favoured.

2.2.3 Microwave heating system

Microwave heating is achieved in a common household oven, model *OMW 310 W*™ built by the company *Ok.*; its original control logic was modified in order to include the thermal control, as reported in previous thesis works [43]. Figure 2.7 depict the arrangement of the components required to operate the magnetron, described in detail in Table 2.4.

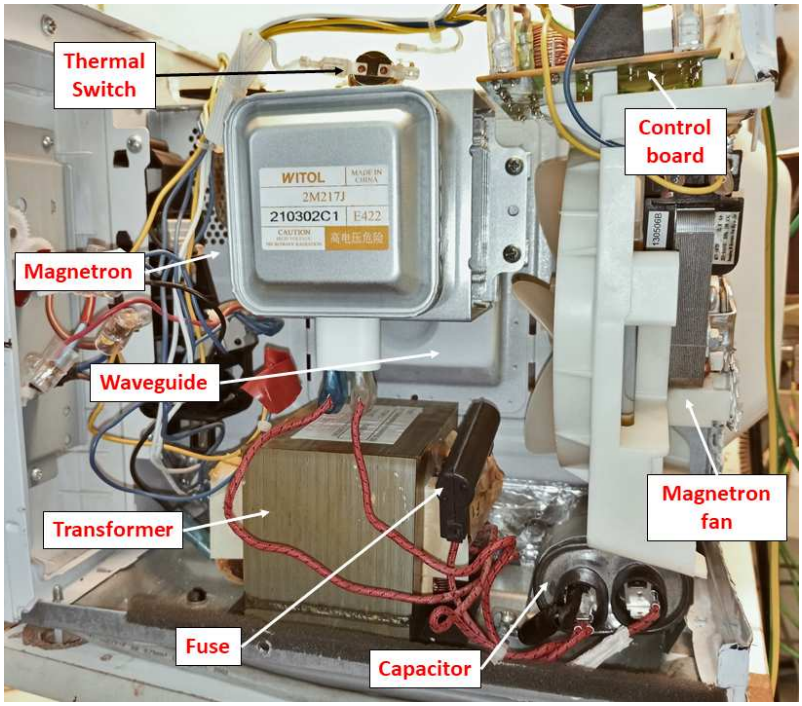

Figure 2.7: Internal components of the Microwave oven.

Safety devices, apart from the fuse, allow to feed the magnetron only when its temperature is lower than a certain limit (thermal switch), and only when the microwave door is closed. Temperature is measured with a K metallic thermocouple, having external diameter of 3 mm (1/8 in). Temperature is controlled by an Omron E5CC™ digital temperature controller. It exploits the on-off control logic, providing electric power to the magnetron through a solid state relay, which open and close the electric circuit that bring electric current at 220 V to the magnetron's transformer. The manufacturer claims that the power absorbed by the oven is 1050 W; the average output power is instead 580 ± 30 W, as reported by the microwave data sheet. The construction features of components present in the MW oven are reported in Table 2.4. Additional informations about the controller are reported in previous thesis works [43]. The reactor scheme is reported in Figure 2.9, while the

reactor dimensions are reported in Table 2.5. The magnetron temperature is monitored too, since its performances and structural integrity depends on temperature; an additional K metallic thermocouple is used for this purpose. The Magnetron temperature is maintained low by adding a cooling fan (in addition to the standard oven fan), as shown in Figure 2.8.

Table 2.4: Characteristic of the components used in the oven.

Component	Model	Manufacturer	Characteristics
Transformer	EMD-701EMR-1	MD Microwave oven manuf.	$V_{in} = 220\ V\ AC$ $V_{out} = 2100\ V\ AC$ $f = 50\ Hz$
Fuse	BJ-HVF-650 mA	BOJACK	$V_{max} = 5\ kV$ $A_{max} = 650\ mA$
Capacitor	CH85-21090	BiCai	$V = 2100\ V\ AC$ $C = 0.9\ \mu F$
Magnetron	2M217J	Witol	$V_{max} = 3.9 \pm 0.2\ kV$ $A^{avg}_{anode} = 200\ mA$ $P^{avg}_{out} = 580 \pm 30\ W$ $f = 2458 \pm 10\ MHz$ $V_{filament} = 3.3\ V$

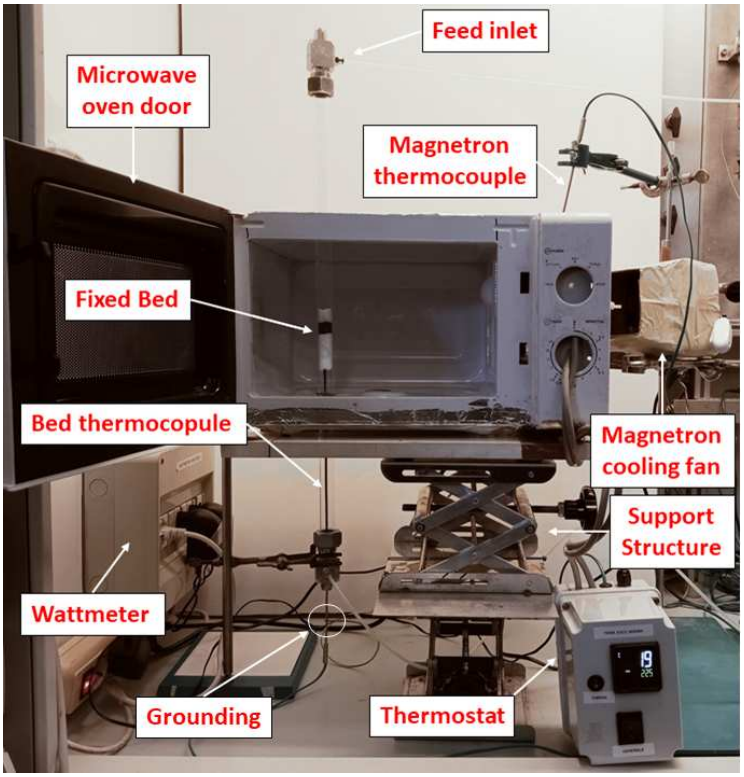

Figure 2.8: Setup of the Microwave heating reaction system.

Finally, it is important to monitor the power absorbed by the system from the whole oven, as to verify the actual energy used. This operation is performed by

the Wattmeter, an instrument internally built by the University of Padova, which measures the active power subtracted by the electric load from the grid. A detailed description of the instrument is reported in section 2.3.4.

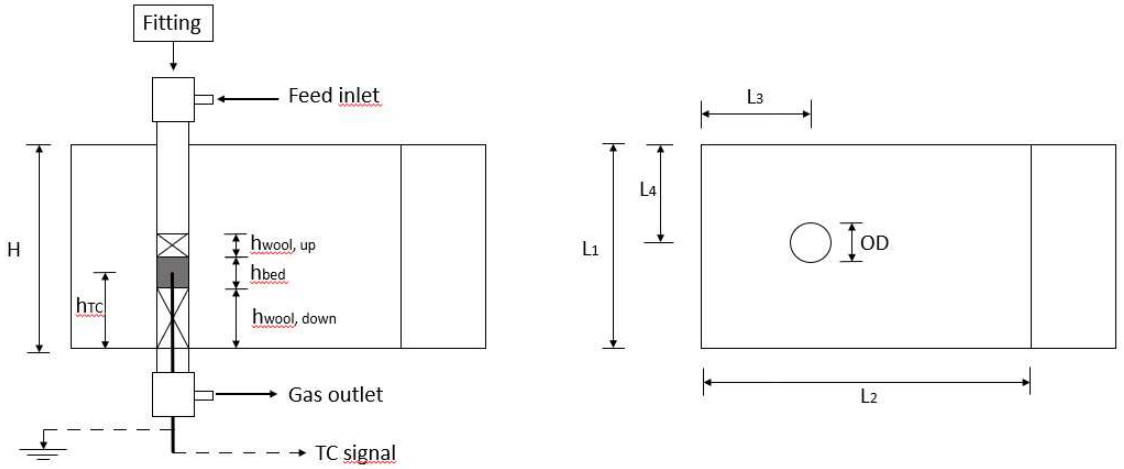

Figure 2.9: Scheme of the experimental setup of the MW oven; (left) front view, (right) top view.

Table 2.5: MW oven dimensions and lengths.

Dimension	Value	Unit	Dimension	Value	Unit
H	17	cm	$h_{wool,down}$	6	cm
h_{bed}	2	cm	h_{TC}	7	cm
$h_{wool,up}$	1.5	cm	H	17	cm
L_1	25.5	cm	L_2	28	cm
L_3	12.5	cm	L_4	12.5	cm
OD	2	cm			

2.2.4 Conventional heating system

Conventional heating is achieved through electric heating. A *Watlow* heater is used; it consist of a refractory cylinder, in which electric resistances are embedded in a refractory structure, which allows the oven to reach a maximum temperature of 1000°C, while consuming 440 W. The oven is shown in Figure 2.10. The resistances operate at 120 V AC. Temperature is controlled by a dedicated software (*CX-Thermo*), which acquires the signal from the thermocouple placed into the catalytic bed. The heater dimensions are reported in Table 2.6. The heater is inserted into a steel tube having diameter of 200 mm, while the empty space between heater and tube is filled with quartz wool to insulate the oven. The steel tube is closed on the top and bottom by means of two perforated lids, with holes of 50 mm in which the quartz tube used as reactor is inserted. Differently from the MW oven, in this case the Omron E5CC controller can be programmed through a PC interface; temperature, sensed by the type K thermocouple inserted in the catalytic bed, is controlled by a dedicated software, namely, *CX-Thermo*. When the measured

Table 2.6: Watlow heater characteristics.

Dimension	Value	Unit
Internal diameter	25	$[mm]$
Outer diameter	76	$[mm]$
Length	305	$[mm]$
Voltage	120	$[mm]$
Power	440	$[mm]$

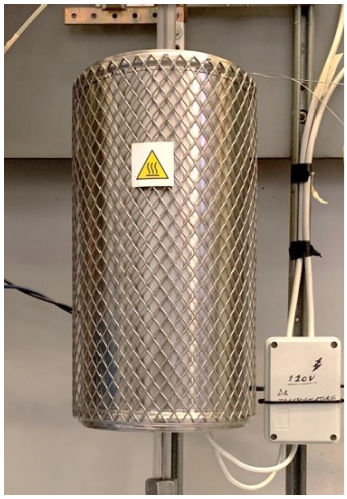

Figure 2.10: Electrically heated oven.

temperature is lower than the set point value, the controller powers on the heater. A PID control logic is implemented, as to best regulate the temperature profile; PID constants are identified through an auto-tuning algorithm, embedded into the controller, while feeding the reactor with the feed mixture.

2.3 Measurement section

The gaseous mixture leaving the reactor (either with microwave or conventional heating) is analysed using a gas chromatograph. One of the chromatographic columns consists in a bed of zeolites; due to the high affinity with water, it is necessary to condense the water formed in the catalytic bed before entering into the gas chromatograph. For this purpose, a condenser is placed right before the GC entrance; here, the wet gas is cooled down to 3°C. Temperature in the condenser is maintained low by a chiller. Once analysed, the mixture is vented into the hood. During the tests, carbon may be deposited on the catalyst; its formation is thermodynamically favoured, as stated by the exploratory equilibrium study, specially at low reaction temperatures. Quantifying the amount of carbon formed during the test is important to get informations regarding the reactions that takes place in the bed. Its quantitative determination is performed through a Temperature Programmed Oxidation process (TPO), which consists in feeding the reactor with a mixture containing a known amount of Oxygen, while heating. The mixture composition used for the TPO is 2% O_2 in N_2. The temperature policy consists in reaching 550°C with a ramp of $15\,°C/min$ in inert atmosphere, and then reaching $650\,°C$ with a ramp of $1\,°C/min$ in oxidizing atmosphere. Knowing the amount of CO and CO_2 formed in the oxidation process, the overall carbon can be estimated with a numerical integration. The mixture of inert, CO and CO_2 coming out is analysed using an FTIR; it was chosen to use the FTIR, and not the GC, due to its much higher sampling rate, as to precisely follow the oxidation process and allow a more accurate evaluation of the integral. In fact, the only species that needs to be measured in a TPO are CO and CO_2; other components of the mixture coming out of the reactor are unreacted

O_2 and the inert.

2.3.1 Gas Chromatograph

Gas coming out of the reactor is analysed through a Gas chromatograph, model *7820*, produced by *Agilent technologies*. The principle of gas chromatography consist in a chemical-physical separation based on adsorption equilibrium of distinct species partitioning between a mobile and stationary phase. The mobile phase is a carrier gas (typically He), while the stationary phase is a polymer on an inert solid support, inside a piece of metal tubing, defined chromatographic column. Walls of the column are coated with stationary phase; as the mobile phase flows through the column, gaseous components bind with different strength with it, causing each compound to elute at a different time, defined retention time, thus allowing for separation. In the GC model used, the gaseous sample is injected into a 6-ways valve, and goes first into the polymeric column (named PPQ, where separation of H_2O, CO_2 and hydrocarbons takes place), and then into a column made of zeolites (MS5A, used to separate the permanent gasses). After the separation, two detectors in series are found; a TCD (temperature conductivity detector) and then a FID (flame ionisation detector), of which only the former is used, due to its ability of detecting all the species. A schematic representation of the instrument is reported in Figure 2.11.

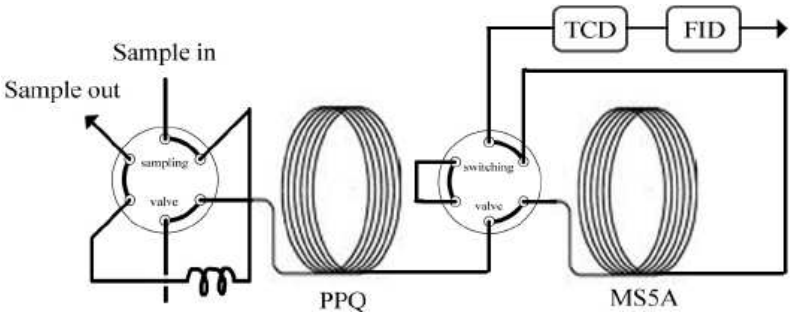

Figure 2.11: Configuration of the GC.

Gaseous components are detected thanks to a thermal conductivity difference with the carrier; thermal conductivity of all the species involved is reported in Table 2.7.

Table 2.7: Thermal conductivity of gasses involved in the separation [36].

Species	**Thermal conductivity**	**Units**
H_2	0.27534	$[W\ m^{-1}\ K^{-1}]$
CO_2	0.03465	$[W\ m^{-1}\ K^{-1}]$
Ar	0.02743	$[W\ m^{-1}\ K^{-1}]$
CH_4	0.07023	$[W\ m^{-1}\ K^{-1}]$
CO	0.3958	$[W\ m^{-1}\ K^{-1}]$
He	0.26062	$[W\ m^{-1}\ K^{-1}]$

The separation performances can be varied by changing temperature, pressure and column length; since the latter is fixed, one can only change the temperature

and pressure profiles in time. The method used to separate the mixture is reported in Table 2.8; the method file is called "Analisi_Microonde_22102021.met", stored in the *PC-GC* computer, under the path "C:/Dati/Openlab/Microonde/Methods".

Table 2.8: Method developed for the GC analysis.

Pressure			
Set point *[Psi]*	Hold time *[min]*	Ramp *[Psi/min]*	Run time *[min]*
40	3.4	-	3.4
30	1.7	50	5.3
35	5.7	30	8.3
Temperature			
Set point *[°C]*	Hold time *[min]*	Ramp *[°C/min]*	Run time *[min]*
55	3	-	3
45	1.9	50	5.1
65	2.2	20	8.3
TCD temperature *[°C]*			
250			
Reference Helium flow *[mL/min]*			
10			
Switch time			
On *[min]*	Off *[min]*		
1.45	2.685		

When the TCD detect a species different from the carrier, a peak is shown on the chromatogram. Height of such peak depends on the thermal conductivity difference between carrier and species; concentration of the component is directly proportional to the peak height, and can be retrieved through a calibration of the instrument performed by feeding the instrument with a mixture of known composition. Figure 2.12 shows the GC used for sample analysis. The instrument is operated by a

Figure 2.12: Gas chromatograph used to analyse the gaseous mixture.

dedicated software, namely *OpenLAB*; peak areas are exported and elaborated using

Matlab, in order to obtain the volumetric concentration of components into the mixture.

2.3.2 FTIR Spectrometer

Sample analysis in gas chromatography is a lengthy process; the method developed require more than 8 minute to complete a single analysis. IR spectroscopy instead is a much faster analytical technique; due to this fact, it was chosen to analyse the TPO exploiting this spectroscopic technique, as to precisely evaluate the amount of carbon deposited during the tests. IR spectroscopy is an analytical technique based on the interaction of electromagnetic radiation with matter. Electromagnetic radiation exploited is infrared (IR) light, between visible and microwave radiation, having a wavelength range of $0.7-1000\ \mu m$, corresponding to a frequency of $0.3-430\ THz$. If absorbed by a gaseous molecule, the energy content of IR light causes the molecule to vibrate; different molecules absorb at different frequencies, depending on the chemical nature of the component. Thus, the vibration frequency is associated with a particular mode of motion and a particular bond type. As specific wavelength gets absorbed (and converted into vibrational motion), the intensity of that specific wavelength decrease; from this fact it is possible to determine the amount of component in the mixture. The instrument is shown in Figure 2.13

Figure 2.13: IRTracer-100.

The analysis produce an IR spectrum that can be visualized in a plot of absorbance intensity as function of wave number. In the instrument, absorbance of the gaseous mixture is measured; its relation with species concentration is given by the Lambert-Beer law:

$$A = \varepsilon \times l \times C \tag{2.1}$$

where A is absorbance (measured by the instrument), ε is the wavelength-dependent absorptivity coefficient, l the path length, and C concentration of the component that is measured. The instrument is equipped with a Michelson interferometer. In the TPO analysis, the FTIR is used to monitor concentration of CO and CO_2 as they are formed from the reactor. Concentration of those species is then used to calculate the amount of carbon that has been oxidized. Carbon oxidation is described by reactions (2.2) and (2.3)

$$C_{(s)} + O_2 \rightarrow CO_2 \tag{2.2}$$

$$C_{(s)} + \frac{1}{2}O_2 \rightarrow CO \tag{2.3}$$

Knowing the amount of CO, CO_2 coming out of the reactor, carbon can be estimated. Both species are detected due to their typical spectrum. Wavenumbers selected for both species are reported in Table 2.9; they were chosen as resulted the most sensible wavenumbers. Since those two are the only species of interest in the analysis, the wavenumber range is restricted to the interval $1950 - 3000\ cm^{-1}$. The instrument resolution is $8\ cm^{-1}$. In the analysis, 5 scans are averaged to give a single measure; the mixture is analysed every 6 seconds circa, thus a single measure takes 30 seconds.

Table 2.9: Wavenumbers for CO and CO_2.

Species	**Wavenumber** $[cm^{-1}]$	**Wavenumber range** $[cm^{-1}]$
CO	2073.3	2026.53 - 2142.25
CO_2	2334.16	2234.34 - 2392.016

Calibration of the instrument is performed by feeding the instrument with inert only (N_2 is typically used), acquiring the background signal; this signal contains all the residue gaseous species present into the cell.

2.3.3 Condenser

The gaseous mixture leaving the reactor contains steam. Water is characterized by high affinity toward zeolites, which are packed into the chromatographic column; thus, it must be eliminated from the mixture. This removal step is performed by a condenser, which is placed right before the GC inlet. The condenser is internally designed [35]; it exploits a *LAUDA* chiller, where ethylene glycol is used as refrigerant fluid. With this fluid, the condenser chamber is cooled down to 3°C, allowing for excess water to be condensed. The instrument is shown in Figure 2.14

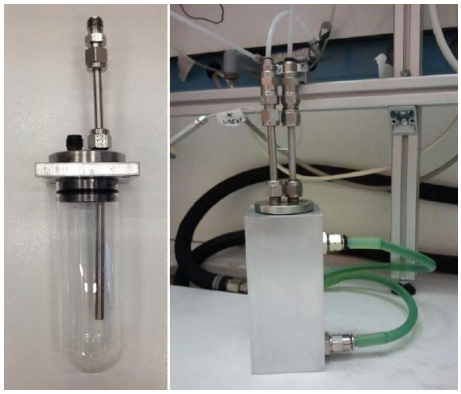

Figure 2.14: Condenser (right) and its internal structure (left) [35].

2.3.4 Wattmeter

Microwaves are generated by the magnetron; when this component is active, the power absorbed by the oven is around 1100 W, while when it is off the power ab-

sorbed is much lower, around 40 W, required by components such as the cooling fans, the temperature controller, etc. It is possible to determine whether the magnetron is correctly working by analysing the instantaneous power absorbed by the MW heating system. The instrument communicate with a PC through the communication protocol Modbus; data are transferred through an USB RS-485 standard communication system. Data are read using Matlab; the program though which data are read is called "pzem_014_RS485_matrix_01.m", located in *PC-SR* under the path "C:/Dati/TAI/TAIDW". Communications between instrument and PC requires less than a second. All the energy required to power the MW heating system is measured by the instrument, placed between the oven and the electric grid, thus measuring the energetic demand of the MW oven and Omron E5CC controller.

2.3.5 Air thermometer

In previous thesis works ([43]) an air thermometer was developed, as alternative method to measure temperature under MW radiation. A technical drawing of the air thermometer is reported in Figure 2.15.

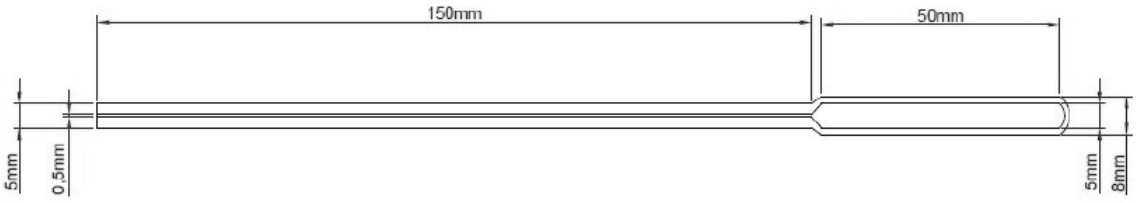

Figure 2.15: Technical drawing of the air thermometer [43].

The air thermometer was built in Borosilicate glass. It consist of a cylindrical bulb, welded to a capillary. Volumes of both bulb and capillary are reported in Table 2.10.

Table 2.10: Volumes of the air thermometer.

Section	Volume	Units
Capillary	29.44	mm^3
Bulb	981.25	mm^3
Total	1010.69	mm^3
Volumes ratio	33.33	–

At the end of the capillary, a Polyamide junction allows to connect the thermometer with the pressure transducer *MPX5500DP*. A metallic bend ensures sealing. Signal from the transducer is split in two different lines; one reach the *PicoLog* acquisition device, the other the Omron E5CC controller. The air thermometer works on a simple principle. Air is a mixture of ideal gasses at low pressures; its volumetric behaviour is well described by the Ideal Gas Equation of State, reported in equation 2.4

$$PV = nRT \tag{2.4}$$

At constant volume and number of moles, Temperature increases lead to Pressure increases. Being a gaseous mixture of low-dielectric gasses, air is not affected by MW radiation; thus, it is possible to exploit its non-dielectric nature to extract informations about the system's temperature. The air thermometer was calibrated by simultaneous immersion with a thermocouple in a oven; results of the calibration are shown in figure 2.16.

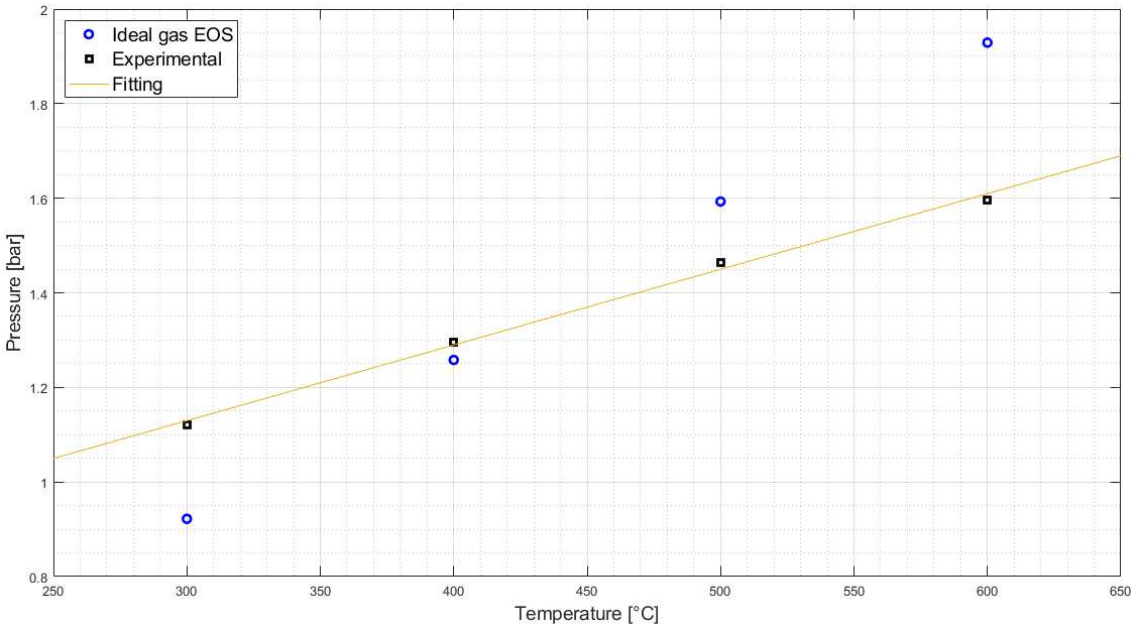

Figure 2.16: Calibration of the air thermometer performed in previous thesis works [43].

2.3.6 Thermocouples

Thermocouples are electronic devices for temperature measurement that are based on the Seebeck effect; in a continuous circuit of two different metallic wires, where the wires are joined together in a hot and cold junction, current flows if the junctions are at different temperatures. A schematic representation of the electric circuit of a thermocouple is depicted in figure 2.17.

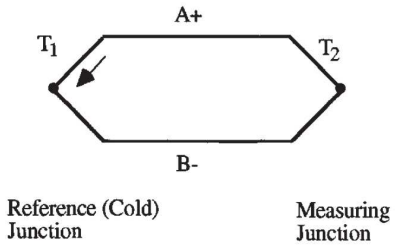

Figure 2.17: Electric circuit of a thermocouple [**?**].

Electric current is generated as result of a voltage difference between the hot and cold junction; the temperature-dependent voltage is proportional to the temperature

gradient between the hot and cold junctions; by knowing the temperature-dependent material properties that relate ∇T with ∇V, called Seebeck coefficient, it is possible to calculate the temperature at the hot junction by knowing the temperature at the cold junction. Type-K thermocouples are the most widespread thermocouples used in industry, due to their low cost, acceptable accuracy and versatility; the metal wires are composed by Chromen and Alumen, and the recommended temperature measurement range is between -200°C and 1100°C, with a sensitivity of 41 $\mu m/K$. Depending on the position of the hot junction with respect to the thermocouple sheath, thermocouples may be classified as (i) grounded, (ii) ungrounded or (iii) exposed, as shown by figure 2.18. The most diffuse type of thermocouple is of

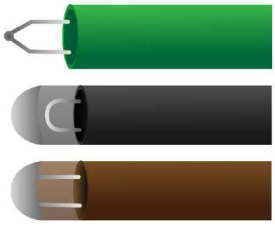

Figure 2.18: Types of thermocouples, depending on the relative position of hot junction and sheath: (top) exposed, (centre) insulated and (bottom) grounded.

the grounded type, as to ensure a fast response and circuit protection; in non-chemically aggressive environments, the exposed type may be employed; finally, for corrosive environments a grounded thermocouple may be desirable, although the thermal response is slower (due to the thermal inertia of the tip). All the thermocouples available in the laboratory are of the grounded type, which ensures chemical resistance and fast response.

2.3.7 Radiation Pyrometer

Temperature measurement using pyrometers is a technique based on the detection of IR radiation emitted by the material. Infrared radiation refer to the fraction of EM spectrum between $0.78 - 1000\ \mu m$ of wavelength, corresponding to frequencies in the range $0.3 - 430\ THz$. When materials are heated, they emit temperature-dependent IR radiation, which is associated with the vibrational and rotational movements of molecules. Radiation emitted by black-bodies (which emit radiation in all wavelengths of the EM spectrum) is described by the Stefan-Boltzmann equation (eq. 2.5, describing the emitted power per unit area) and by the Plank's law (eq. 2.6, describing the power per unit area emitted at a specific wavelength):

$$J_B = \sigma T^4 \tag{2.5}$$

$$L(\lambda, T) = \frac{C_1}{\lambda^5} \frac{1}{\exp\left(\frac{C_2}{\lambda T}\right) - 1} \tag{2.6}$$

where J_B is the black-body emissivity (measured in W/m^2), σ the Stefan-Boltzmann constant, L the spectral emissive power (measured in $W/m^2\mu m$), C_1 and C_2 the Plank's constants. By measuring the emitted IR radiation at specific wavelengths,

it is possible to calculate the temperature of emitting material, assuming it behaves as a black-body. The pyrometer used in this thesis work is shown in Figure 2.19; it was purchased from *TC Direct*.

Figure 2.19: The radiation pyrometer.

The pyrometer available in the laboratory is characterised by a wavelength measurement range of $6 - 14\ \mu m$, which is located in the mid-IR region.

2.4 Programs

In this paragraph it is reported a list of the programs that were used to monitor the variables of interest during the tests. These are listed in Table 2.11

Table 2.11: Programs used to monitor the variables of interest

Variable	Program	Method file	Location (PC)	Path
Flowrate	Excel	-	PC-Flux	*C:/Dati/MF/Tutti_da_xls*
Pressure Drops	TAI.exe	TAID4.met	PC-SR	*C:/Dati/TAI*
Pressure	Picolog	-	-	-
Temperature	Picolog	-	-	-
Temperature	CX-Thermo	-	-	*C:/Dati/Cxthermo/Microonde/DryRef_12.14.2021*
Temperature	TAI.exe	TAID4.met	PC-SR	*C:/Dati/TAI*
Power	pzem_014_RS485_matrix_01.m	-	PC-SR	*C:/Dati/TAI/TAIDW*
Composition	Openlab	Analisi_Microonde_22102021.met	PC-GC	*C:/Dati/Openlab/Microonde/methods*
Composition	LabSolution IR	-	PC-IR	*C:/Dati/FTIR/Microonde*

Chapter 3

Experimental Results

In this chapter the results of the experimental campaign carried out in the laboratory are reported. Three main areas of interest were investigated in this thesis work; first, a reliable method for temperature measurement, essential for development of the reactor's control system; then, the experimental setup necessary to perform the reaction was determined; finally, comparison of the MDR reaction in both heating systems is performed. In the following chapter all the three topics are discussed in detail.

3.1 Temperature measurement

Temperature measurement under microwave radiation is not a trivial task [17]. Conventionally, temperature is measured using thermocouples; however, the presence of MW radiation determine the impossibility of using metallic objects into the oven cavity, if appropriate precautions are not taken. Other possibilities for measuring temperature involve the usage of non-contact methods, such as IR pyrometry; however, this technique only allows to measure the reactor's external surface temperature, making impossible to extract informations on the thermal behaviour of the inner layers of the catalytic bed. Another temperature measurement technique involve the use of air thermometer; this solution was proposed in previous thesis works [43]. In the following paragraphs, all these temperature measurement techniques are discussed.

3.1.1 Air thermometer

The literature survey showed that no studies were found in which air thermometers were used for temperature monitoring of reactions under MW heating. *Bond et al.* [9] was among the first to suggest the structure of an air thermometer to be used under MW heating; the proposed structure consists in a bulb connected to a capillary tube, which is itself connected to a pressure transducer. The material suggested in the article is Pyrex (borosilicate glass), which can be used up to its softening point (about 500°C). Pyrex is not suitable for high temperature environments, like the ones in which the MDR reaction takes place. A convenient material characterized by low dielectric properties is quartz, which is able to withstand high temperatures,

maintaining unaltered its mechanical and chemical properties. Quartz is, in fact, a very inert material having a melting point of at least 1425°C [**?**]. Contrary to thermocouples, where the measured temperature is referred to a small volume nearby the tip (where convection due to hot gas, radiation and conduction from SiC influences the measure), the air thermometer has a larger sensing volume, leading to an averaged bed temperature, in which contributions of both hot and cold spots (generated by the uneven distribution of the EM field in the bed) are summed up. In addition to this problem, the usage of such air thermometers imply several complications. Quartz is a material hard to form into capillary shapes, due to its brittleness; not all glassmakers are able to work the material to produce this capillaries having an internal diameter of half a millimetre. Apart from this minor problem, several major challenges remain. Two aspects were found to be particularly important: (i) heat losses from the capillary, and (ii) the rapid heating typical of dielectric lossy materials under MW radiation. These two aspects will be analysed in depth in the following paragraphs.

Maximum allowable pressure in the bulb

The maximum allowable pressure which the bulb was able to withstand was estimated to avoid breakage due to high pressure conditions at high temperatures. This estimation is based on the procedure used to size metallic pipes in industry, which exploit the Barlow's equation [**?**]; however, data of hoop tensile strength σ for common glasses is not available in literature, since glass is not a common building material for piping. In order to estimate the bulb's maximum allowable pressure, values of σ for glass-fibre composites were retrieved from literature [8], and then a stringent safety factor k was applied to reduce the maximum allowable pressure. The Barlow's equation (Eq. 3.1) appear as

$$P_{max} = k\left[\frac{2 \cdot s \cdot \sigma}{d_{ext}}\right] \tag{3.1}$$

where s is the pipe thickness, d_{ext} the pipe's external diameter, P_{max} is the maximum allowable pressure for the material, and k is the safety factor. Dimensions of the air thermometer were retrieved from the technical drawing shown in Figure 2.15. Imposing a safety factor of 0.05 (that means, if the hoop tensile strength of glass is only 5% the one of those glasses reported in the study), the maximum allowable pressure resulted equal to 3.1 bar, which is however sufficient to withstand the theoretical 2.5 bar that would be obtained if air in the bulb was found at 500°C, the maximum possible temperature for Pyrex (calculated from the ideal gas EOS).

Calibration

To be used, the air thermometer needs to be calibrated, as to verify the relation between pressure inside the bulb, voltage produced by the pressure transducer, and the bulb's air temperature. Two different methods were used to calibrate the probe;

1. *Temperature calibration*
   First, the probe was inserted into the electric oven; temperature was independently measured by using a thermocouple, and the oven was controlled

through a dedicated software (*CX-Thermo*). The measurement range was limited to 25°C-500°C, since the only gas thermometer available was made in Pyrex (borosilicate glass). The resulting voltage produced by the transducer was then measured, and the relation $T(V)$ was obtained by coupling the temperature from thermocouple with voltage from the pressure transducer. A scheme of the arrangement is reported in Figure 3.1. In this arrangement, a part of the stem was inevitably exposed to air, since the pressure transducer needed to be placed outside of the oven.

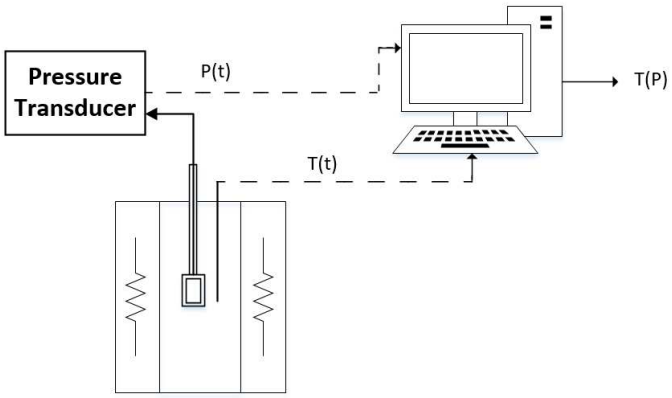

Figure 3.1: Schematic diagram of the temperature calibration.

2. *Pressure calibration*
A double-check was performed by calibrating the system by changing pressure, instead of temperature. The schematic diagram of this pressure calibration is reported in Figure 3.2. Pressure of the compressed air coming out of the

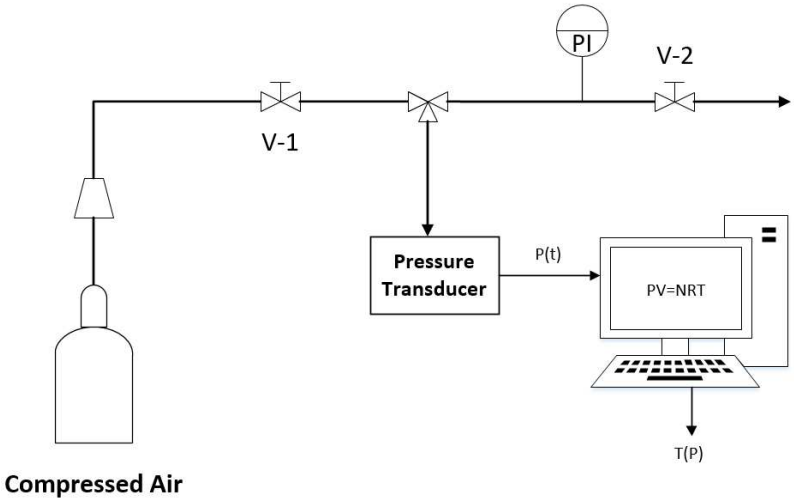

Figure 3.2: Schematic diagram of the pressure calibrations.

cylinder at 5 bar was first reduced through a first valve (V-1), maintaining opened the valve at the end of the line (V-2). Then, pressure was gradually increased by partially closing the valve V-2; the corresponding voltage measured

by the transducer were recorded. Assuming valid the Ideal Gas EOS, the only difference between the two calibrations is the presence of heat losses, which may be present into the temperature calibration, but are absent in the pressure calibration. Pressure was monitored by using several different manometers, as to exclude instrument defects. Temperature was then obtained by exploiting the Ideal Gas EOS; the mass density was first evaluated at ambient temperature and pressure, by knowing the thermometer dimensions, as:

$$\rho_{air} = \frac{P}{RT} MW_{air} \Big|_{T_{amb},\ P_{amb},\ V_{bulb}} \tag{3.2}$$

Density remain constant if (i) the bulb volume remains the same at any temperature (thermal expansions of Pyrex are neglected), and (ii) no leakages at the thermometer-transmitter junction are present. Then, temperature was calculated as:

$$T = \frac{P \cdot MW_{air}}{R \cdot \rho_{air}} \tag{3.3}$$

Results of both calibrations are reported in Figure 3.3. It can be seen that the pressure calibration is almost linear, whereas the temperature calibration is not; the two curve diverges at high temperature. Divergence can be determined by several factors; first, the ideal gas EOS is not a suitable EOS to describe the system; alternatively, leakages were present during the pressure calibration, which in turn could lower the $P(V)$ relation (reported in Eq. 3.4).

$$P = 1.5 \cdot 10^{-3} V + 0.4 \tag{3.4}$$

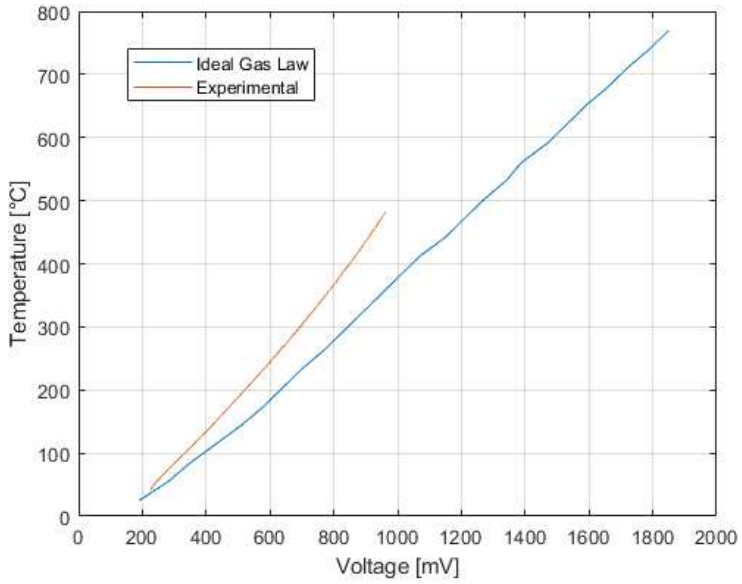

Figure 3.3: Calibrations of the air thermometer. Red line is referred to the temperature calibration; the blue line refer to the pressure calibration.

Finally, heat losses in the temperature calibration may have influenced the measure (the latter, however, should have led to opposite behaviour, that is, pressure

measured should have been lower than the observed one). The calibration curves were found by fitting of experimental data with a polynomial curve (linear for the pressure calibration, quadratic for the temperature calibration). Equations of the fitted calibration curves are reported in Eq. 3.5 (for pressure calibration) and Eq. 3.6 (for temperature calibration).

$$T(V) = 4.44 \cdot 10^{-1} \cdot V - 1.54 \cdot 10^{2} \tag{3.5}$$

$$T(V) = 2 \cdot 10^{-4} \cdot V^{2} + 3.875 \cdot 10^{-1} \cdot V - 48.182 \tag{3.6}$$

Where temperature is expressed in °C and voltage in mV. To determine which calibration curve better describes the thermometer behaviour, it was decided to perform a test where the temperature probe was immersed in a hot oil bath, whose temperature was simultaneously monitored by using an independent thermocouple, as shown in Figure 3.4.

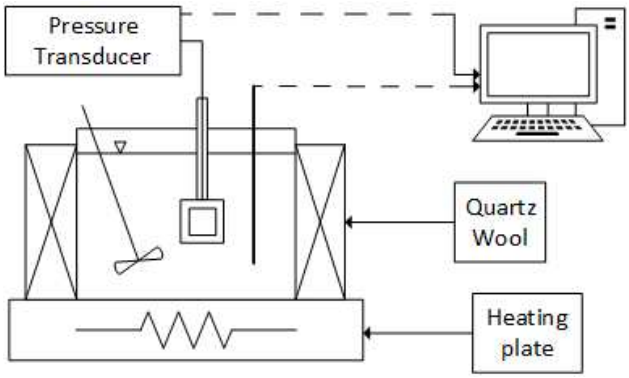

Figure 3.4: Test performed to check the air temperature calibration.

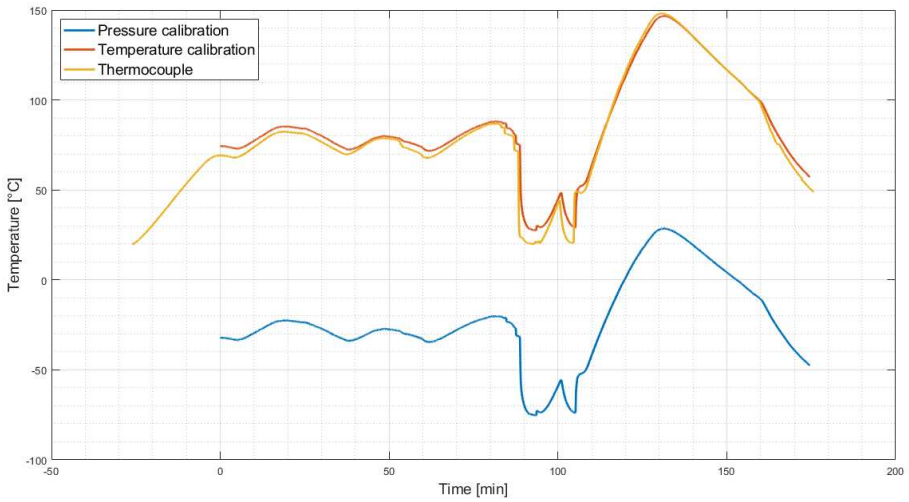

Figure 3.5: Temperature profiles of the type-k thermocouple (yellow line), the pressure-calibrated thermometer (blue line) and the temperature-calibrated thermometer (red line).

The oil bath was heated on a heating plate; in order to ensure that no temperature gradients were present in the oil bath, insulators and stirrers were added.

Both thermocouple and transducers signals were acquired by a data logger (*PicoLog* recorder). The temperature calibration better fits the thermocouple's temperature profile, as shown by Figure 3.5.

Heat losses

Heat losses represents a huge obstacle to the implementation of this probe. Assuming the bulb in thermal equilibrium with the catalyst bed, all the remaining parts of the air thermometer would be exposed to lower temperatures; as stated in the literature survey (section 1.2.2), temperature of the gas phase coming out of the catalytic bed may be hundreds of degrees lower than the bed's temperature. This temperature difference induces heat losses, both conductive (in the thermometer, from the bulb to capillary end) and convective (at the interface gas-thermometer, toward the gas phase). In addition, in order to avoid gas leakages from the reactor, the air thermometer must pass through the junction (made of steel, an highly conductive metal), which is at room temperature, contributing to the conductive heat losses. Assuming steady state, where the thermometer's stem temperature is constant, a simple heat balance may be written as

$$Q_{bed} - Q_{loss} = 0 \tag{3.7}$$

Where Q_{bed} is the conductive heat from the bed, while Q_{loss} represents the heat losses due to convection (heat transfer between gas and the capillary) and conduction (heat transfer at the end of the thermometer's stem). Heat losses are modelled as:

$$Q_{loss} = A \cdot q''_{loss} = A_b \cdot q''_{cond} + A_{ext} \cdot q''_{conv} \tag{3.8}$$

where A_b is the cross-section area of the stem, while A_{ext} is the external surface area. A simple model for estimation of heat losses may be expressed as follows; assuming constant temperature in the cross section of the stem (no radial gradients), constant bed temperature (steady-state), conductive heat losses inside the stem are:

$$q''_{cond} = k \cdot \Big(T_{stem}(z) - T_{amb}\Big) \tag{3.9}$$

while the convective heat losses may be expressed as

$$q''_{conv} = \overline{h}\Big(T_{stem}(z) - T_{gas}\Big) \tag{3.10}$$

Thanks to this energy balance, it would be possible to estimate the stem temperature $T_{stem}(z)$, and further assuming thermal equilibrium between the capillary and air (contained into the capillary), the pressure inside the capillary can be estimated. The convective heat transfer coefficient depends on the flow filed conditions; for annular flows, it can be estimated through Dittus-Boelter correlation [28];

$$Nu_D = 0.023 \cdot Re_D^{4/5} Pr^{0.3} \tag{3.11}$$

where Re is the Reynolds number, Nu the Nusselt number, Pr the Prandtl number. Subscript D indicates that the dimensionless numbers are based on the hydraulic diameter. However, precise estimations of T_{gas} are required to solve the system of

equations. In literature [24], under MW heating, the gas temperature was estimated with energy balances which involved a kinetic model for the MSR reaction, which has to be theorised (since the effect of MW on reacting systems is not clear). In absence of the gas-phase temperature measures, it is not possible to analytically determine the air pressure inside the capillary. Independently of the quantitative estimations of Q_{loss}, the dissipated heat reduces the air temperature inside the capillary, making it lower than the one into the bulb. As direct consequence, pressure measured by the transducer will be lower, introducing an under-estimation error. To determine the effect of heat losses on the measure, the thermometer was immersed into the hot oil bath at different depths, and the measured temperature (using calibration 3.6) was compared with the measurement of a thermocouple, placed at the same depth; the thermometer's stem was immersed at 1/4, 1/2, 3/4 of his length, and for the latter, an additional test with insulation was also performed (by insulating the part of capillary outside of the oil bath, to verify the difference between tests at the same immersions, in presence of capillary insulation). Results are shown in Figure 3.6. It can be clearly seen how the immersion depth influenced the measure's accuracy. In fact, the error between the two measures was reduced with increasing immersion depths, as shown in Figure 3.7.

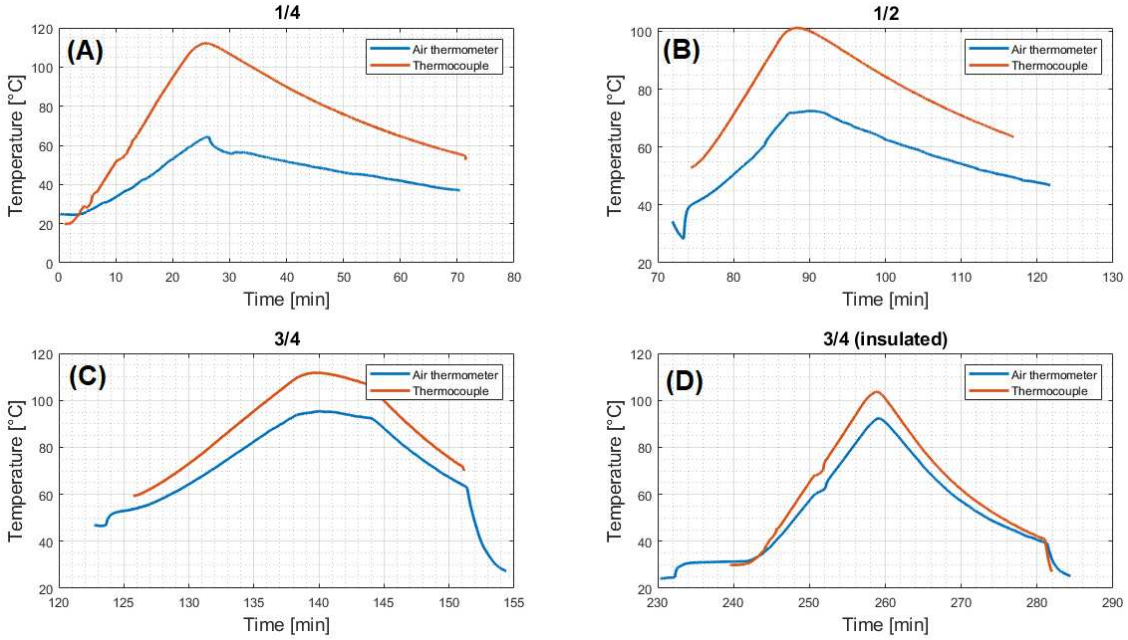

Figure 3.6: Temperatures of the thermocouple (blue line) and thermometer (red line) vs time at different immersion depths. Thermometer immersed for 1/4 (**A**), 1/2 (**B**), 3/4 (**C**), 3/4 with insulation (**D**).

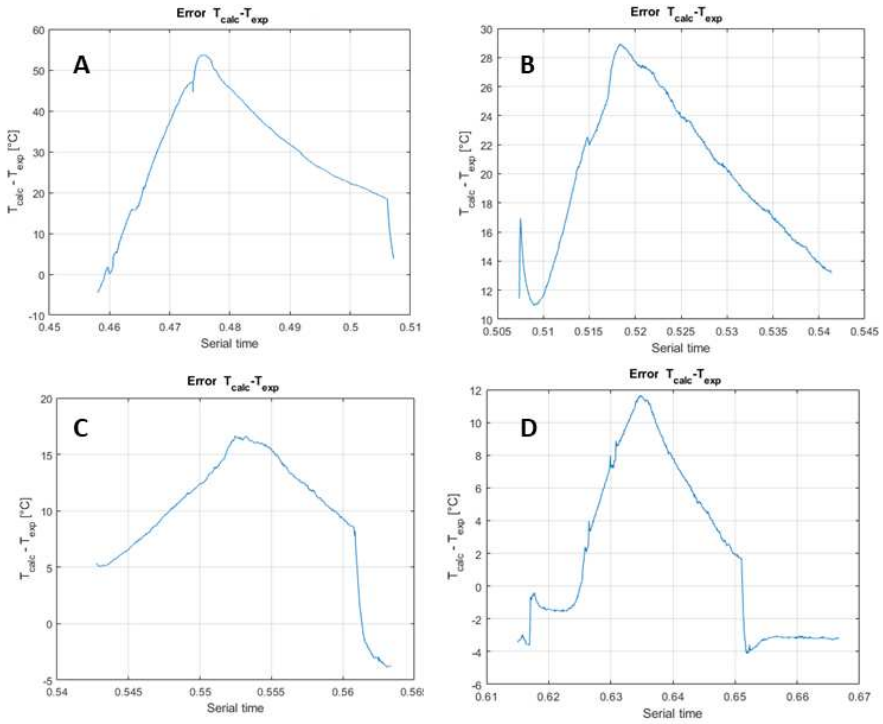

Figure 3.7: Errors between the two temperature probes vs time at different immersion depths. Thermometer immersed for 1/4 (**A**), 1/2 (**B**), 3/4 (**C**), 3/4 with insulation (**D**)

Rapid heating

Dielectric lossy materials, when exposed to MW radiation, increases their temperature in a very short time; SiC, for example, has been observed to get red hot ($T > 550$°C) in less than a minute of exposure to microwaves in our setup. This aspect is central in dielectric heating; it allows the solid to reach high temperatures in very short transients. However, the construction material of the air thermometer is characterized by low thermal conductivities, as reported in Table 3.1.

Table 3.1: Thermal conductivities of some materials.

Material	**Thermal conductivity** $[W/mK]$	**Ref.**
Silicon Carbide	490	[46]
Borosilicate glass	1.4	[46]
Quartz	6.21	[25]
Chrome iron	111	-
Borosilicate glass	1.1	[46]
Stainless steel	15	-

Due to its much lower thermal conductivity, Pyrex is not capable of rapidly transporting heat from the SiC bed toward the air inside of the thermometer. Depending on the bulb thickness, a delay between the actual bed temperature and the one recorded by the thermometer may exist. In order to verify this aspect, the air

thermometer was inserted into the electrically heated oven, and temperature ramp was first imposed of 10°C/min, and then with a higher temperature ramp (20°C/min, where the maximum ramp was 25°C/min due to instrument limitations). Results of the test are shown in Figure 3.8. In the first test (10°C/min) the air thermometer was softened by the high temperatures; thus, in the following test the maximum temperature was limited to 350°C. A small measurement lag between the thermo-

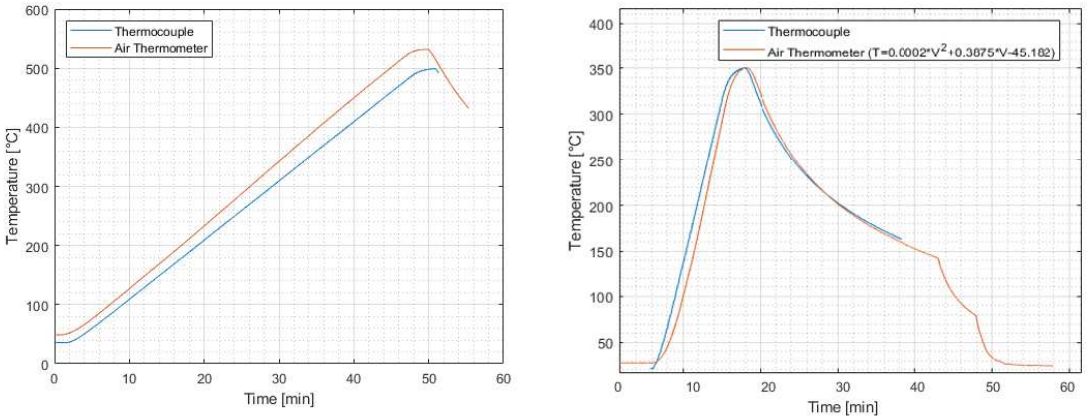

Figure 3.8: Temperature profiles of the type-k thermocouple and the temperature-calibrated thermometer. Heating rates of 10°C/min (left) and 25°C/min (right).

couple's measurements and the one of air thermometer was recorded during the heating phase; during cooling instead, temperature decreased, allowing for thermal equilibrium to be established between Pyrex and the external temperature inside the oven. Influence of heating rates is further underlined in heating tests performed in the MW oven, where the air thermometer was immersed in a bed of SiC, while a type K thermocouple was used to monitor the temperature of the capillary outside the oven (as to avoid interferences with MW); the scheme of such test is reported in Figure 3.9.

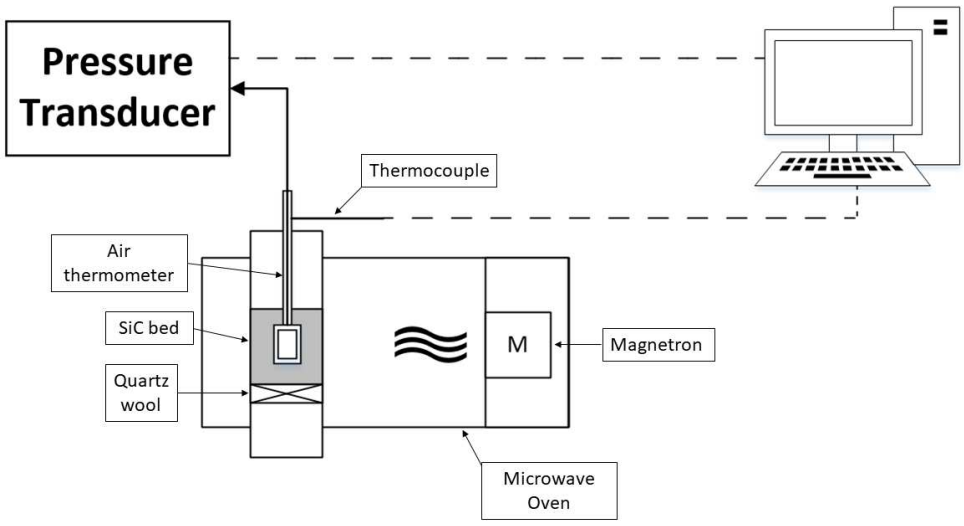

Figure 3.9: Scheme of the test used to determine the influence of heating rates.

In this test the air thermometer melted, even if both the thermometer and the thermocouple indicated a temperature much lower of 500°C, as shown by Figure 3.10. The melted probe is shown in Figure 3.11. The oven was controlled by the Air thermometer. This was interpreted as a direct effect of the uneven tempera-

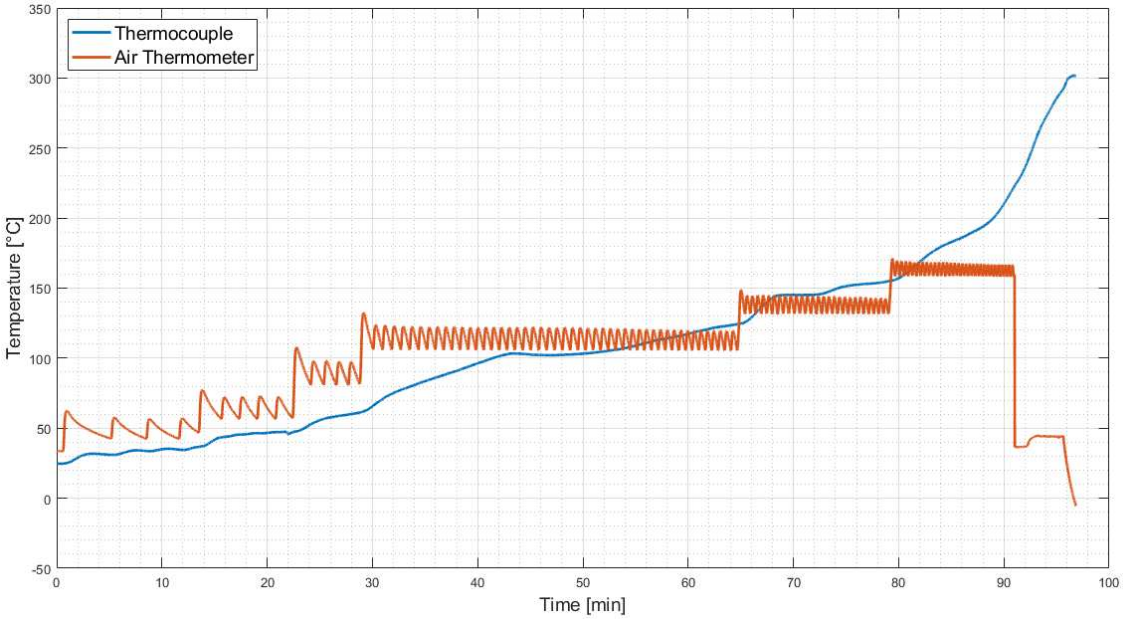

Figure 3.10: Temperature profiles of the thermocouple and air thermometer.

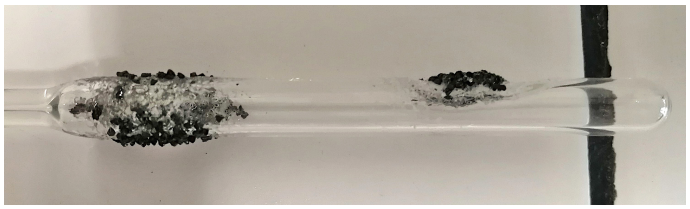

Figure 3.11: Melted probe; In the points where glass melted, SiC granules were included in the structure..

ture distribution in the bed under multi-mode dielectric heating; depending on the instantaneous field distribution, local temperature may vary from point to point. In addition, large overshoots were present in the signal of the air thermometer; this is due to the thermal inertia of glass. When the bed temperature reach the set point, the air temperature of the thermometer is lower, due to its thermal inertia; during this period, the MW oven continue to deliver MW to the bed, whose temperature increase above the set point. As a consequence, overshoots are observed, which may lead to melting, if hot-spots are present in the bed, as the test suggested.
Another test was performed with a similar configuration, now with the thermocouple immersed into the SiC bed. The test's scheme is reported in Figure 3.12; the purpose of the test was to compare the measure performed by the thermometer with the one of the thermocouple, as to determine the effect of heat losses. To reduce interferences between MW and the metallic thermocouple, the thermocouple was

completely immersed in SiC, from the oven's base, as shown by the scheme. Results of the test are shown in Figure 3.13. The two temperature probes report very

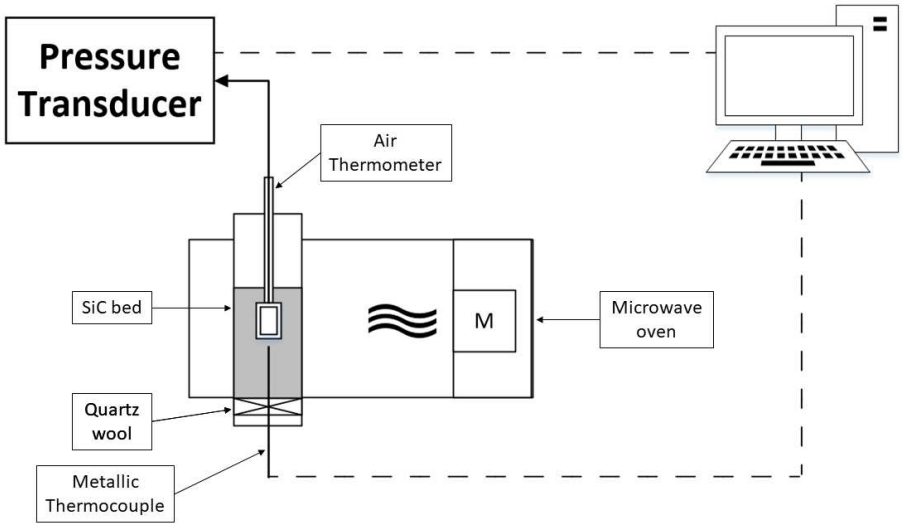

Figure 3.12: Scheme of the test used to compare the temperature measured by the air thermometer and the metallic thermocouple.

different temperatures; in particular, the air thermometer seems to underestimate the temperature measure, even with a 300°C error with respect to the thermocouple, assuming that the latter was shielded by the SiC layers.

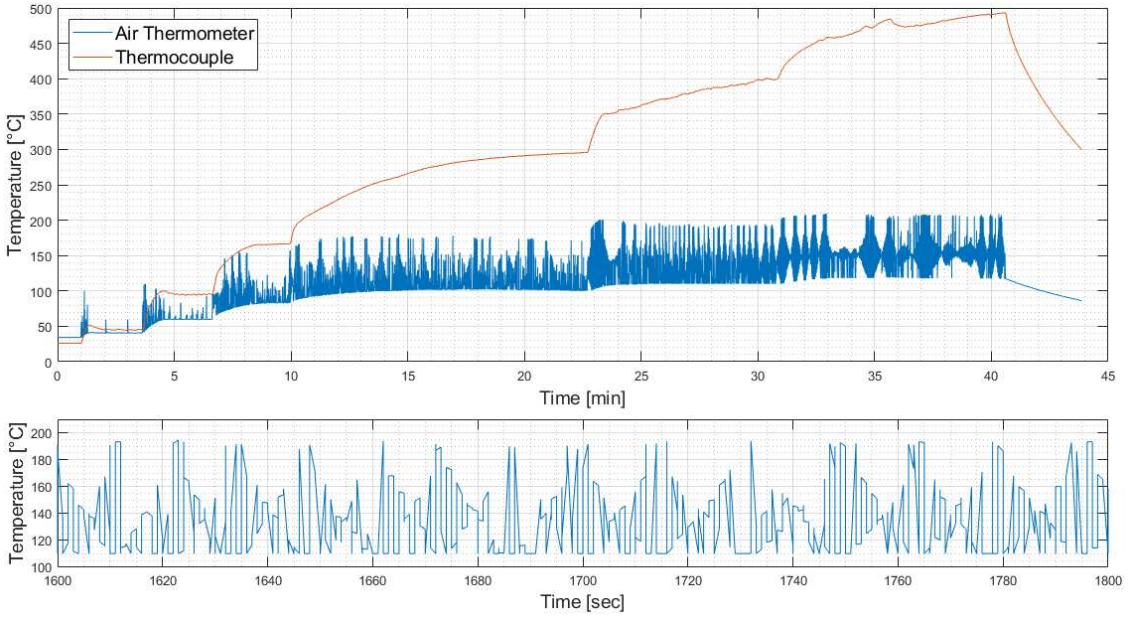

Figure 3.13: Temperature profiles of the air thermometer and the metallic thermocouple (top). Zoom of the air thermometer's temperature profile (bottom).

This effect was traced back to the inability of the temperature calibration to accurately represent the real temperature of the system. In addition, the pressure transducer seems to show interferences with the EM field, as the large overshoots

suggest. Instantaneous overshoots (of 100°C circa) are not compatible with the phenomenon of dielectric heating of SiC, since the thermal inertia of glass would not allow for such improvise temperature increases. Interference may be caused by the effects that MW have on electric components inside the pressure transducer (that is the component closer to the MW cavity).

Final considerations on the air thermometer

The previous two paragraphs analysed in depth the problems of heat losses and rapid heating. Heat losses may be reduced by insulating the stem (which however must pass through the reactor junction), or by increasing the ratio between bulb to capillary volumes. Maximization of such a ratio leads to a very short and thin capillary, or to a very large bulb. Both configurations are not feasible; a large bulb would imply a reduction of the space available for the catalytic bed into the reactor, with consequences on the fluid dynamics of gasses into the bed (the cross section where the gas could flow would be reduced, thus increasing the gas velocity, reducing the contact time between the gas and solid phases). Instead, a very short capillary would not allow for the passage of the capillary into the joints, and would increase the probability of interferences between MW and electric components of the pressure transducer. It is concluded that temperature measurement under MW radiation using air thermometers is not the optimal solution.

3.1.2 Non-contact methods

The most popular and widely used method to measure the reaction temperature in MW applicators is infrared (IR) pyrometry [17], a technique based on detection of IR radiation emitted by the material. Infrared radiation refer to the fraction of EM spectrum that is comprised between wavelengths of $0.78 - 1000\ \mu m$, corresponding to frequencies in the range of $0.3 - 430\ THz$. However, several factors makes the measurement technique not adapt to our experimental setup. IR pyrometry is based on measurements of wavelengths in the mid-IR spectrum; in this wavelength range, Quartz is not completely transparent to IR radiation, thus a part of the emitted radiation would be blocked, distorting the temperature measure. Anyway, even in presence of transparent materials, the technique only allows to measure the superficial temperature of the external layers of the catalytic bed. It would be impossible to measure temperature at the reactor's centre.
In addition, the pyrometer available in our laboratories do not allow for data recording. It works by analysing emitted wavelengths in the range $6 - 14\ \mu m$; in this range quartz is opaque, as can be seen from Figure 3.14; By means of IR pyrometry it is possible to measure the sample temperature without perturbing the EM field inside the oven cavity. The measure is not affected by the thermal properties of the probe, like its thermal capacity and resistance.

Assuming SiC can be described as a black body, it can be seen that, for temperatures around 1000 K, a fraction of emitted power is in the range of 6-14 μm (as shown by Figure 3.15) where Quartz is opaque; part of the emitted radiation would be blocked, thereby distorting the temperature measure. Apart from this objection,

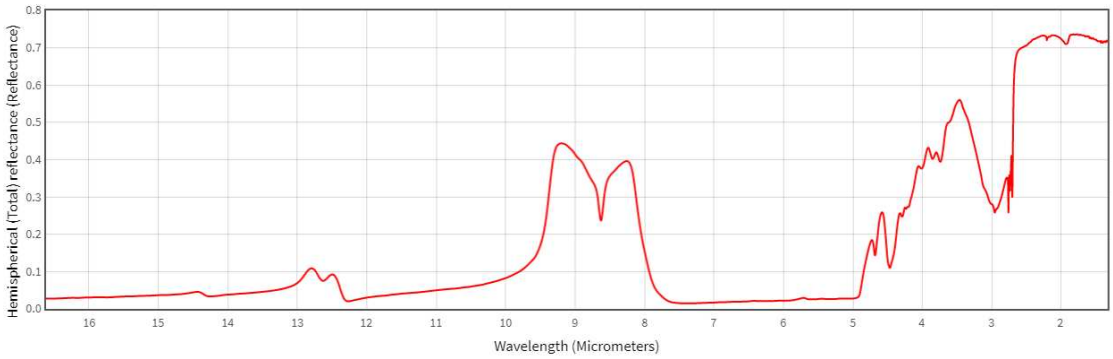

Figure 3.14: IR reflectance spectrum of Quartz.

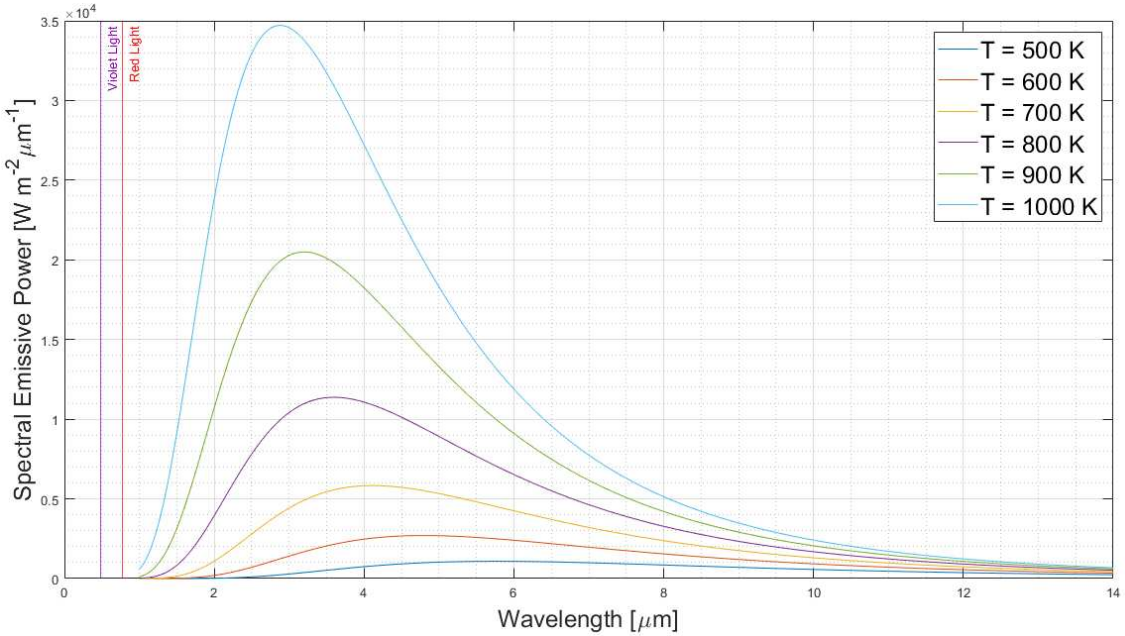

Figure 3.15: Spectral emissive Power of a black body.

it was decided to study the behaviour of the pyrometer under MW heating anyway by drilling a hole in the oven cavity, as to allow for a direct measure of the reactor temperature. A scheme of the test is reported in Figure 3.16; the IR pyrometer is located at 7 cm circa from the reactor. With this arrangement, interference was noted between the measure provided by the pyrometer and the EM field; this interference manifested as instantaneous oscillations of the temperature measured of 15-20°C, corresponding to the magnetron activation, thus, with emitted MW radiation. Interference cannot be explained by the rapid heating of SiC under MW radiation, since the latter take place within minutes, and it is not instantaneous as the pyrometer measure imply. The measurement error may be explained by the interference between the EM field generated by the magnetron and the electrical components into the pyrometer.
Apart from the interference phenomenon, usage of IR pyrometers is hindered by the presence of insulation around the quartz reactor. Insulation is necessary to avoid radiative and convective heat losses from the catalytic bed to the air inside the oven

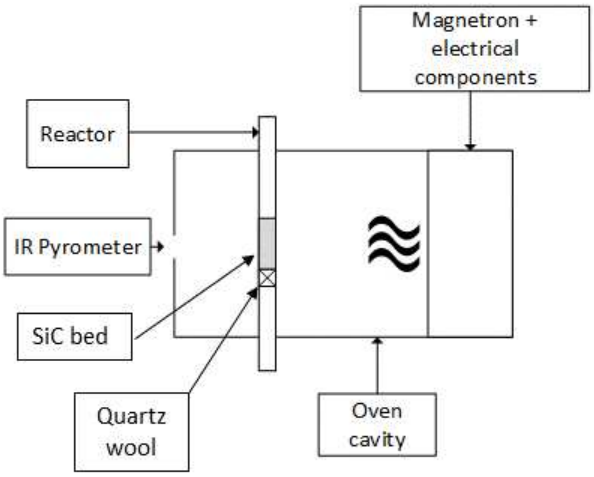

Figure 3.16: Schematic diagram of temperature measurement arrangement using the IR pyrometer.

cavity. Radiative heat losses are particularly relevant at high temperatures, typical of the MDR reaction; such heat losses can be estimated from a simple model, using the Stefan-Boltzmann law (Eq. 2.5), under the assumptions of (i) SiC treated as a black body, (ii) adiabatic system (no heat transfer between the oven and the external environment takes place), (iii) negligible conduction and convection heat transfer, (iv) uniform air temperature inside the oven cavity, and (v) air is the only component capable of absorbing radiative heat. With a bed height of 2 cm, at 800°C, the calculated emitted power is

$$P = J_B \cdot A = \sigma T^4 A = 90\ W \tag{3.12}$$

where A is the external area of the catalytic bed. This power is sufficient to heat air inside the oven cavity up to 183°C in half a minute, starting from ambient temperature. This calculation is based on a emitting area of SiC of 11.8 cm^2, which radiates a volume of air of 14458 cm^3, corresponding to the oven dimensions. The air temperature after 60 s of exposition to radiation is determined as

$$T_{air}(t) = T^0_{air} + \frac{P \cdot \Delta t}{m_{air} c_{P,air}} \tag{3.13}$$

Clearly, this simple model overestimate the final air temperature, since it do not account for convective and conductive heat losses, and for the fact that the oven walls are subject to radiative heat from the bed, thus air is not the only one component susceptible to radiation.

Another non-contact temperature measurement method consist of fibre-optics (FO) thermometry, a temperature measurement technique based on the light absorption/transmission properties of semiconductors; when temperature change, the transmission spectrum of the semiconductor is shifted to higher wavelengths. This shift is determined by variations in the semiconductor's energy band gap, which tends to narrow at higher temperatures (since electrons have higher kinetic energy,

less energy from photons is needed to excite the electrons). The typical FO structure is reported in Figure 3.17; the semiconductor crystal, in contact with the material whose temperature has to be measured, is enclosed into a PTFE pipe. A FO (made of silicon-based material) allow light transmission from the inside of the environment to the spectrometer, where light is analysed to reveal the sample temperature.

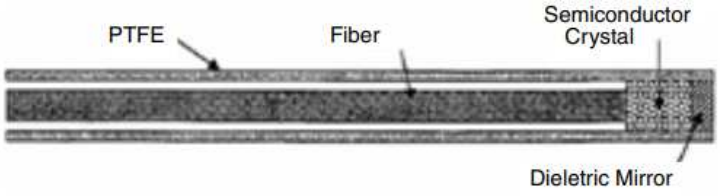

Figure 3.17: Structure of a FO temperature sensor.

FO thermometry cannot be implemented in our experimental setup; in fact, the fibre cannot withstand high temperatures required for MSR, due to the physical properties of its construction materials. In addition, the probe would measure only the temperature of the external surface of the reactor, making impossible to investigate the thermal behaviour of the catalytic bed's inner strata.

Final considerations on non-contact methods

Non contact methods are used extensively in literature. However, they are suitable only for measurements of thin catalytic beds, since they only senses the superficial temperature, while MWs are characterized by volumetric heating. In addition, the reactor material is not completely transparent to IR radiation, making it impossible to obtain a reasonable measurement. Other non-contact methods like FO cannot be implemented due to the high temperatures typical of the reforming reaction.
It is concluded that non-contact methods are not suitable for measuring the bed temperature under MW heating of interest in this study.

3.1.3 Thermocouples

Thermocouples are metallic devices, which cannot be placed in the MW cavity due to their interaction with the EM field. The effects of placing a thermocouple into the oven cavity described by *Pert et al.* [47] (section 1.1.10) are:

1. Field enhancement at the thermocouple tip
2. Dielectric breakdown
3. Ohmic losses
4. Thermal conduction

In the following paragraphs, these effects will be discussed in detail.

Thermal conduction

As discussed in the article, thermal conduction is relevant only if the sample's thermal conductivity is much lower than the one of the thermocouple sheath. As can be seen from table 3.1, the thermal conductivity of SiC is much higher than the one of the thermocouple's sheath; thus, the thermal conduction away from the sample can be neglected.

Dielectric breakdown

Dielectric breakdown refer to the physical phenomenon in which an insulator, exposed to a sufficiently high voltage, suddenly transform into a conductor, allowing for the passage of electrons. It is described by the Paschen's law, an empirical relation expressed in Eq. 3.14:

$$\Delta V_b = \frac{B \cdot P \cdot d}{\ln(A \cdot P \cdot d) - \ln[\ln(1 + \gamma_{se}^{-1})]} \tag{3.14}$$

where ΔV_b is the voltage breakdown value (the minimum voltage necessary to determine dielectric breakdown in the material), P is pressure, d the gap distance, γ_{se} is the secondary-electron-emission coefficient, A is the saturation ionization in the gas at a particular $|\boldsymbol{E}|/P$ value, B is related to the excitation and ionization energies. Retrieving all these data for the reacting mixture used in the experiments is not a simple task; literature data concerning the secondary electron coefficients is particularly scarce, making it impossible to analytically determine the breakdown voltage. In addition, the granular nature of the SiC bed may imply the presence of sharp edges on the granules, on which the electric field may be intensified. It is not possible to analytically determine whether electric discharge take place in the bed; the only way to determine its presence is by visually inspecting the catalytic bed, but also with this approach it would only be possible to observe discharges taking place in the internal part of the bed.

Ohmic losses

Another potential problem underlined in the article is the presence of Ohmic losses in the thermocouple sheath. When metallic materials are exposed to MW radiation, free electrons in the metallic tends to flow on the outer part of the material, in a layer called *Skin Depth*, thereby producing electric currents. This is particularly important for good conductors, in which $\sigma >> \omega\varepsilon'$ (or, equivalently, $\varepsilon'' >> \varepsilon'$). For good conductors, the skin depth may be evaluated as

$$\delta_s = \sqrt{\frac{2}{\omega\mu\sigma}} \tag{3.15}$$

This skin depth is a very thin layer; values of δ_s for some metallic materials are listed in Table 3.2. The presence of electric currents lead to heating due to the presence of Ohmic losses; the electric current density vector depends on the imposed electric field, which in multi-mode MW oven is not a constant in both space and time. For isotropic materials the current density vector is [39]:

$$\boldsymbol{J} = \sigma \cdot \boldsymbol{E} = j\omega\varepsilon_0\varepsilon^* \boldsymbol{E} \tag{3.16}$$

Table 3.2: Skin depth of some metallic materials [48].

Material	**Skin depth** $[\mu m]$
Aluminium	0.814
Copper	0.66
Silver	0.64

By knowing $\boldsymbol{J}$ it would be possible to determine the electric current in the skin depth, thus, the amount of heat produced by Joule effect, since

$$Q_{joule} = P\Delta t = \Delta t R I^2 \tag{3.17}$$

where R is the electrical resistance of the sheath material. Analytical predictions of $\boldsymbol{J}(\boldsymbol{x}, t)$ requires the knowledge of $\boldsymbol{E}(\boldsymbol{x}, t)$ on the thermocouple surface, which are not available in our case. Thus, it was preferred to determine the influence of Ohmic losses experimentally. The test was performed by inserting two thermocouples, one with a metallic sheath, the other with a ceramic sheath (composed by a refractory oxide recrystallised, Alumina Impervious), as shown in Figure 3.18.

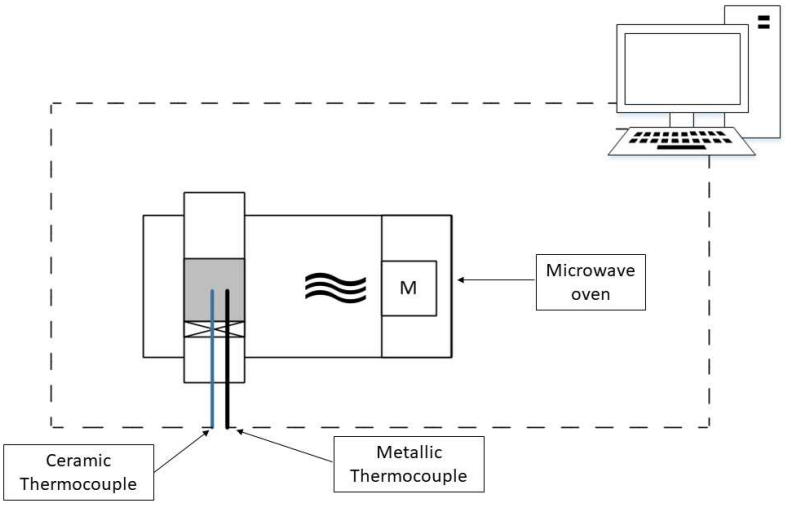

Figure 3.18: Scheme of the test with a metallic and a ceramic thermocouple.

Results of the test are shown in Figure 3.19.

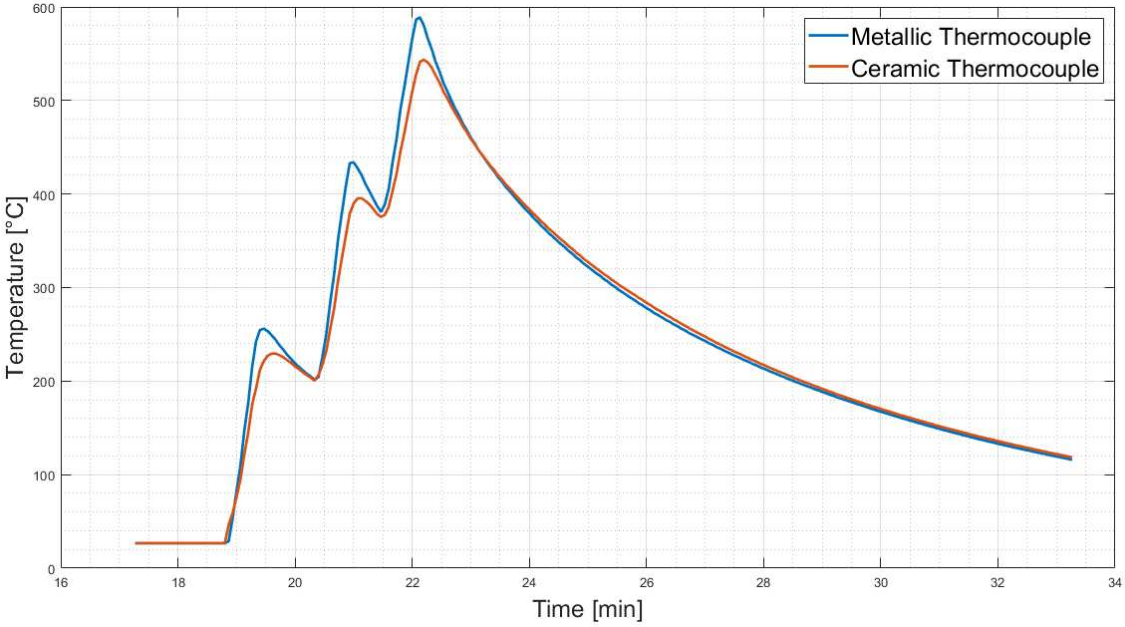

Figure 3.19: Results of the test with two thermocouples of different sheath materials.

A minimum temperature difference between the two thermocouples during the heating ramp is recorded; however, this temperature difference may be traced back to the higher thermal inertia of the ceramic material, or to the fact that thermocouple tips are placed in slightly different positions, and in presence of a highly inhomogeneous temperature field this may lead to the observed differences. It was concluded that, even if Ohmic losses may be present in the metallic thermocouple, their influence is not dramatic.

Field enhancement at the thermocouple's tip

The final effect related to the presence of metallic objects into the oven cavity is related to the field enhancement at the thermocouple tip. Such effect is determined by two factors: (i) the presence of pronounced curvatures at the thermocouple tip, and (ii) intensity of the EM field at the tip. The former effect is related to the accumulation of charged particles where the surface is curved. On flat surfaces, the repulsive force acting between two charged particles is described by the Coulomb's law:

$$F = k_e \frac{e_1^- e_2^-}{d^2} = k_e \left(\frac{e^-}{d} \right)^2 \tag{3.18}$$

where k_e is the Coulomb's constant, e^- the electron charge, and d the distance between the two particles. This force act parallel to the surface, on flat surfaces, and is responsible for electron repulsion and for even charge distributions. However, on curved surfaces the parallel component the net repulsive force between two electrons is characterized by a lower parallel component (responsible for particle repulsion), as is shown by Figure 3.20, due to the orientation of forces. The parallel component of the force can be written as

$$F_{//} = F \cos(\theta) \tag{3.19}$$

Where θ is the angle between the component of force parallel to the surface, and the force acting on the line passing between the two electrons.

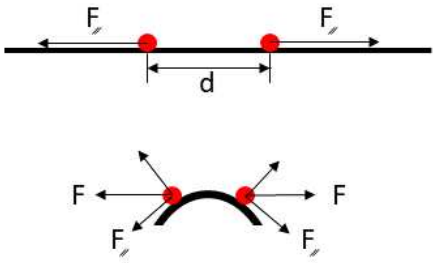

Figure 3.20: Scheme of the forces acting on electrons (red dots) on flat (top) and curved (bottom) surfaces.

.

Since the parallel component of force is lower, particles are less repulsed, thus higher particle densities are obtained on flat surfaces. As a consequence, electric fields in correspondence of the tip are higher. This effect can be mitigated by using thermocouples of larger diameter, due to the curvature reduction at the tip.

Concerning the EM field intensity at the thermocouple tip, this information is not easy to be determined, due to the complications induced by (i) the presence of a large number of resonant modes into the multi-mode cavity, which implies an electric field $\boldsymbol{E}$ that changes both in time and space, and (ii) the variation of dielectric properties of SiC with temperature. To get an estimation of the intensity of the electric field at the thermocouple tip, a simple model was developed. This model is based on some fundamental assumptions, namely:

- MW radiation is considered as a plane wave
- The reactor is considered as a homogeneous, semi-infinite plane
- Reflection phenomena are neglected (all the incident radiation is absorbed by SiC)
- The incident wave frequency is 2.45 GHz
- Variations of dielectric properties of SiC with temperature are described by the experimental data of *Sugawara et al.* [56]
- Wave propagate in a 1D space

The behaviour of dielectric properties for SiC, as determined by *Sugawara et al.*, is reported in Figure 3.21. Under those restrictive assumptions, the wave propagation into the material is described by Eq. 1.9, which for 1D problems become

$$E(z,t) = E_0 e^{-\alpha z} e^{j(\omega t - \beta z)} \tag{3.20}$$

Coefficients α and β are the Attenuation factor and the Phase factor, respectively. These coefficients can be calculated using equations 1.11 and 1.12. In particular, α

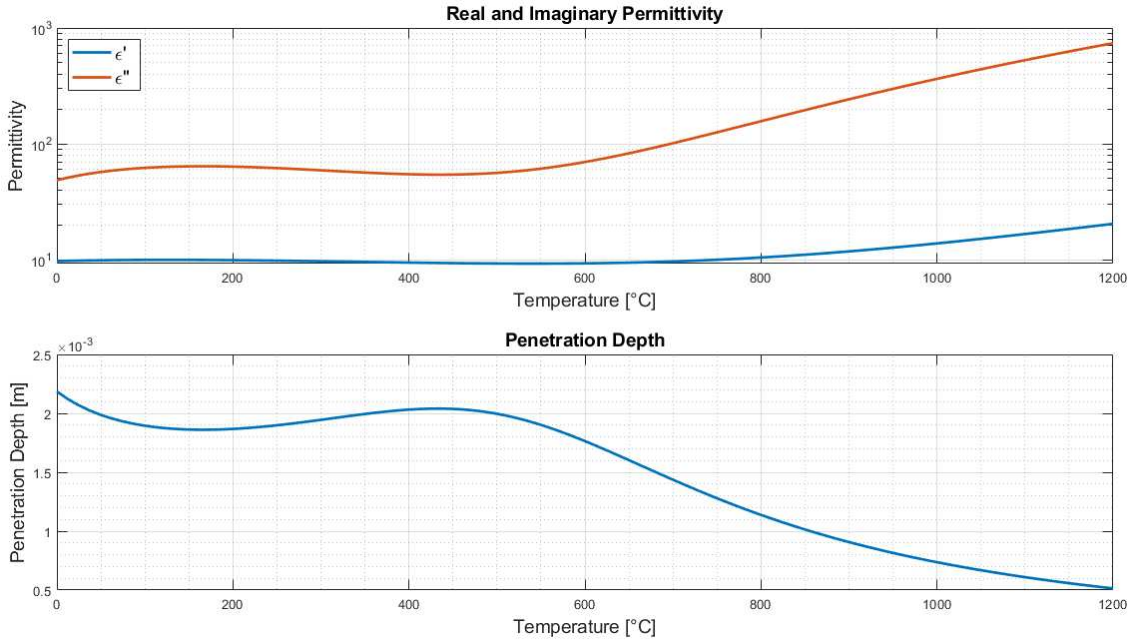

Figure 3.21: Behaviour of dielectric properties (top) and Penetration depth (bottom) for *SiC* as function of temperature. Data from *Sugawara et al.* [56]

.

is related to the attenuation of the wave as it moves deeper into the material, while β is related to the phase difference between the incident wave and the one travelling into the material. Wave attenuation is related to the real part of Eq. 1.10.
As the wave travel into the material, the electric field decays exponentially. Coupling this information with the one defined by the penetration depth (Eq. 3.20), some important conclusions can be drawn. In fact, D_p defines the distance from the surface where the electric field reduces to e^{-1} of its incident value:

$$E = e^{-1}E_0 \sim 36.79\%E_0 \tag{3.21}$$

At the material surface, this ratio is equal to 1. Thus, the ratio E/E_0 is known in two different points, as reported in Table 3.3.

Table 3.3: Evolution of the EM field with depth

EM field intensity ratio E/E_0	**Depth from the surface** $[m]$
100%	0
∼36.79%	D_p

By knowing these two points, and the shape of the exponential decay of the EM field through the material, it is possible to infer the behaviour of the normalized function E/E_0 through a fitting procedure. The exponential decay function exploited for this purpose is

$$f(z,T) = \exp(-k(T)\cdot z) \tag{3.22}$$

where k is the coefficient to be optimized, as to minimize the distance between curve and the points reported in Table 3.3, where the ratio E/E_0 is known. In correspondence of the optimum conditions for this fitting procedure, the coefficient k will be equal to α. The behaviour of $k(T)$ is reported in Figure 3.22; as it can be seen, its value increases with temperature, thus, the EM wave is attenuated at high temperatures. The behaviour of the fitted function $f(z,T)$ is plotted in Figure 3.23, for various temperatures, in terms of normalised variables (E/E_0 as function of z/R, where R is the reactor radius). It can be seen that, under the assumptions listed above, the strength of the EM field in the centre of the catalytic bed is almost zero. This result is in agreement with the temperature profiles obtained in the tests under MW heating, since no dielectric breakdown is observed in the temperature profile of the thermocouple (which would be displayed as abrupt temperature increases, due to plasma formation). As the model shows, little to no EM radiation reach the thermocouple's tip at all temperatures. This result, along with the previous results and with the regular temperature profiles obtained during the tests, allow to exclude the effects reported by *Pert et al.* [47], leading to the conclusion that thermocouples are the best temperature monitoring device in MW heating. However, several important simplifications were used to develop the model. First of all, data concerning the behaviour of $\varepsilon', \varepsilon''$ for SiC at different temperatures are of fundamental importance, and needs to be measured for the Silicon Carbide used in the tests. In the multimode MW oven, the incident radiation is not a plane wave; instead, a large set of standing waves are generated in the complex geometry, each of them characterized by a defined frequency. Reflections of the bed were not considered, and the material was assumed to be a continuous, homogeneous material, as to neglect any reflection phenomena. Clearly, all these aspects cannot be used to validate the experimental results in absolute terms. Additional experimental proofs are needed to confirm the usage of thermocouples into the MW oven.

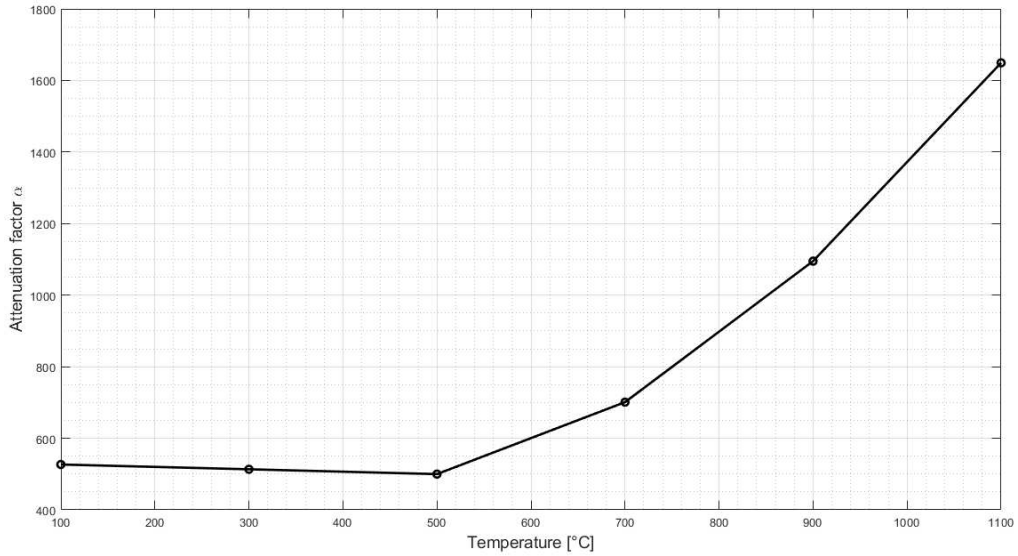

Figure 3.22: Calculated attenuation factor for SiC as function of temperature.

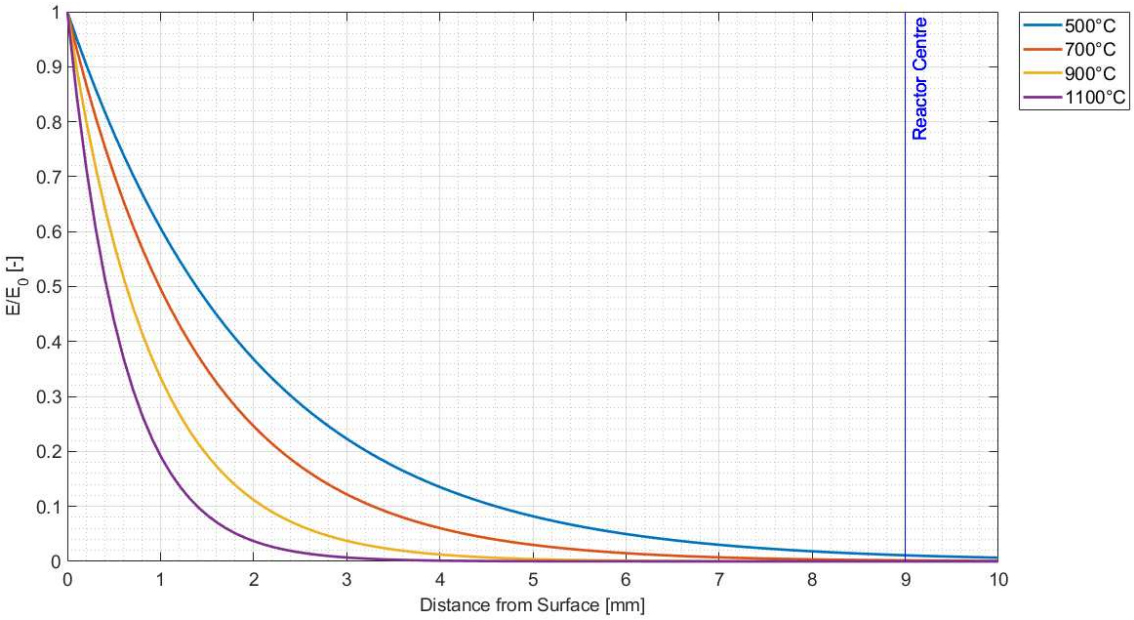

Figure 3.23: Normalised electric field intensity for various temperatures, obtained from the fitting procedure.

Adiabatic energy balance

Due to the uncertainties in the measure provided by the metallic thermocouple, it was decided to set up a test to compare the temperature measured by a thermocouple subjected to MW radiation, with a calculated temperature obtained from an adiabatic energy balance between air and SiC. The scheme of such test is reported in Figure 3.24.

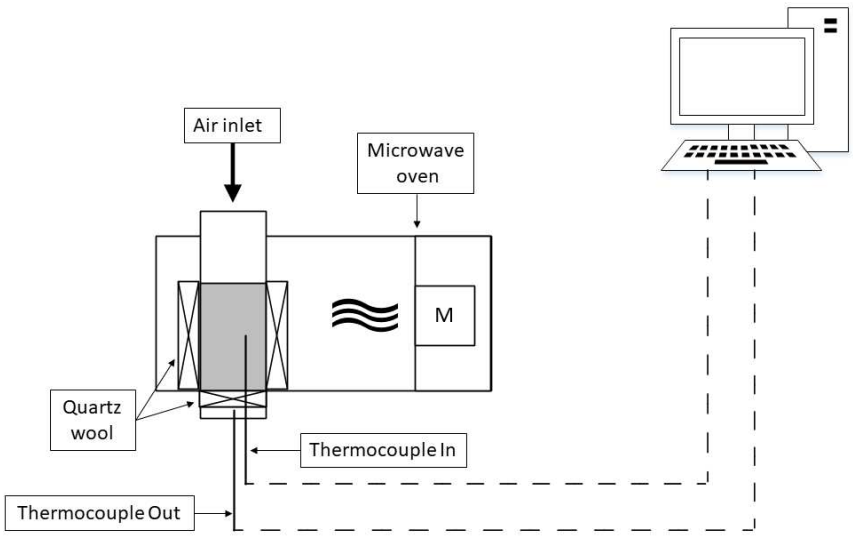

Figure 3.24: Scheme of the test.

It consist of two thermocouples, one placed inside the catalytic bed (subject to MW radiation), the other placed outside of the cavity oven. Air is fluxed on the bed;

the latter is maintained in position by a thin layer of quartz whool. In this layer, the air temperature drops, thus its height is kept low to ensure low temperature drops; the drop can be estimated in ± 16°C at steady state. If the internal thermocouple properly works when MW are absent, the temperature measured during the cooling phase is the exact temperature of the bed. The only doubt temperature is the one recorded under MW radiation, in the instant before the MW oven is shut down. To verify that the temperature measured by the thermocouple under MW heating is not affected by interference errors, an adiabatic energy balance is performed between air and SiC. The model used to derive the energy balance assumes (i) a uniform temperature distribution inside the catalytic bed, (ii) negligible heat losses form the reactor toward the environment, and (iii) thermal equilibrium between air and SiC at the reactor outlet. By knowing the temperature drops of air, and the final SiC temperature (in the cooling phase), the initial temperature of SiC can be determined; comparison of the calculated temperature with the measured one (under MW radiation, right before switching off the oven) indicate if the thermocouple is subject to interferences. The adiabatic energy balance, written in terms of power, is

$$P_{SiC} = P_{air} \tag{3.23}$$

$$\left(mC_p\frac{\Delta T}{\Delta t}\right)_{SiC} = \left(\dot{m}C_P\Delta T\right)_{air} \tag{3.24}$$

If the outlet air temperature measured by the thermocouple is not affected by MW, then the initial SiC temperature (measured under MW radiation, before the oven is turned off) can be evaluated as

$$T^0_{SiC} = T^{end}_{SiC} + \frac{\dot{m}_{air}C_{P,air}\Delta T_{air}}{m_{SiC}C_{P,SiC}}\Delta t \tag{3.25}$$

Results of the test are reported in Figure 3.25; data used to calculate the SiC temperature are referred to the cooling phase, after the magnetron is turned off, while the temperature to be calculated (and compared with the experimental value) is referred to the last heating cycle (minute 29 on Figure 3.25). The calculated temperature is in almost perfect agreement with the measured SiC temperature, with a difference between the calculated and measured temperatures lower than the thermocouple sensibility, as can be seen by Table 3.4.

Table 3.4: Comparison of the calculated and measured temperature of the thermocouple inside the bed.

Measured T [°C]	**Calculated T [°C]**	**Difference [°C]**
70.01	69.391	0.619

Final considerations about thermocouples

Tests performed allowed to conclude that the effects described by *Pert et al.* ([47]), listed in Section 3.1.3, are not present, or negligible. The most relevant effect is probably related to the presence of Ohmic losses in the metallic thermocouple sheath.

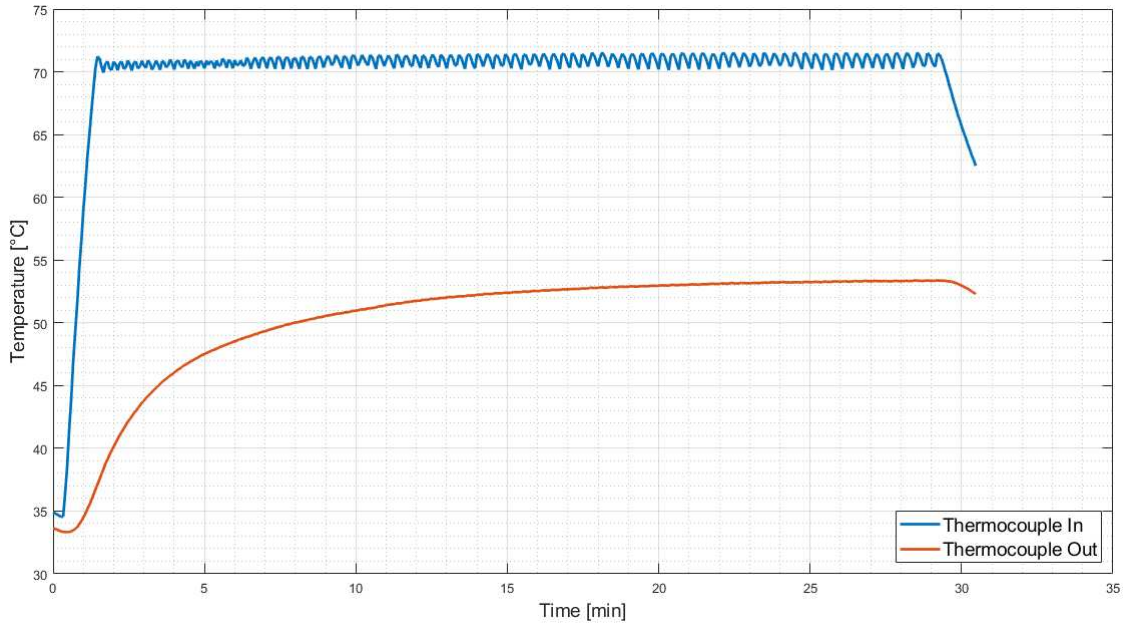

Figure 3.25: Results of the test.

However, since the MDR reaction takes place at high temperatures, the thermocouple tip inside the catalytic bed would be at higher temperatures than the ones reached as consequences of Ohmic losses in the sheath, thereby reducing the temperature distorting effect. The adiabatic energy balance allowed to confirm the measurement accuracy; however, further tests may be needed to confirm the result, specially for higher temperatures. The penetration depth analysis suggest that the amount of radiation reaching the reactor core is low, challenging the idea of volumetric heating, characteristic of MW dielectric heating; however, this result has to be carefully weighted, due to the impact of the number of assumptions required for the calculation. In particular, the incident radiation cannot be treated as a plane wave; many different resonant modes are present in the cavity oven, which cannot be neglected in a more detailed analysis. From the penetration depth analysis, the minimum SiC thickness required to dampen the radiation intensity down to 10% of its incident value was evaluaed in 4.5 cm at 500°C; since the thermocouple is positioned at the reactor centre, at a depth of 9 mm form the surface, the interference between radiation and thermocouple can be neglected. Another problem is related to the presence of a highly inhomogeneous temperature field in the bed; thermocouples measure only a single-point temperature, which may not be representative of the overall temperature distribution. Temperature gradients may be contained by implementing a low bed height; however, the bed height determines also the capability of SiC to act as a MW radiation sink, reducing the fraction of incident wave that is reflected back to the magnetron, leading to hazardous overheating of the MW generator. Finally, thermocouple grounding is necessary to avoid charge accumulation in the bed and thermocouple sheath. Results of both theoretical calculations and experiments are promising; it was decided to implement a metallic thermocouple in the setup to measure temperature, even if the problem related to this measurement strategy, listed in this paragraph, are well known.

3.2 Experimental setup

Once the best temperature measurement strategy was determined, it was necessary to define the experimental setup to be used for the tests under MW heating. Several factors were considered; in the following paragraphs, the most important ones are discussed in detail.

3.2.1 Thermocouple diameter

Type-K thermocouples available in our laboratories are characterised by different sheath external diameters, namely 1/8, 1/16 and 1/32 of inch (corresponding to 3.175, 1.5875 and 0.793 mm). Usage of the 1/32 *in* diameter thermocouple was excluded, due to the lack of rigidity. It was chosen to used the type-K due to its high measurement range, which span from -200°C to +1100°C; moreover, the only available thermocouples were of the "grounded" type, due to their fast response to temperature changes (since the hot junction is in contact with the thermocouple tip). The thermocouple diameter plays a fundamental role under MW heating, due to the effect of field enhancement at the tip; lower diameters implies higher curvatures at the tip, where the hot junction is located, thus, higher risks of dielectric breakdown (i.e. sparks). The presence of breakdown phenomena were analysed with a series of tests, where the thermocouples were immersed in the SiC bed; under the presence of dielectric breakdown, the resulting temperature profiles should be characterized by irregular behaviours, with sudden peaks of large magnitude (several hundreds of °C) associated with plasma formation. In a first test, three 1/16 *in* thermocouples were placed inside the SiC bed as shown by Figure 3.26. The bed extended down to the cavity basement, as to maximise the shielding effect of SiC; the thermocouples were placed ad different heights (2, 4 and 8 cm from the cavity bottom), to study the axial thermal profile of the bed. SiC having particle size higher than 1 mm were used.

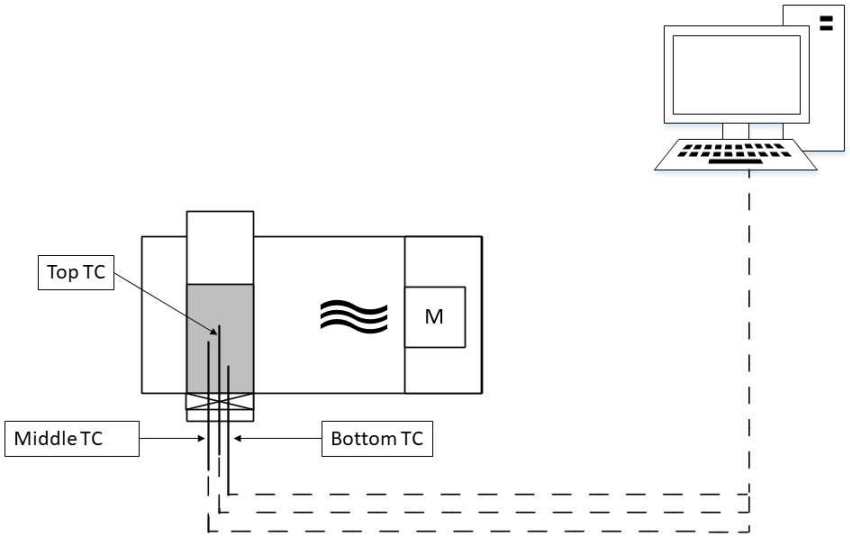

Figure 3.26: Scheme of the test, with three thermocouples located at 2, 4, 8 cm from the cavity bottom.

Two tests in sequence were performed, as reported in Figure 3.27. The MW oven was manually turned on and off, since no control was yet implemented. This test was performed in absence of air fluxes through the bed, as to emphasize the temperature gradients formed in different positions of the bed.

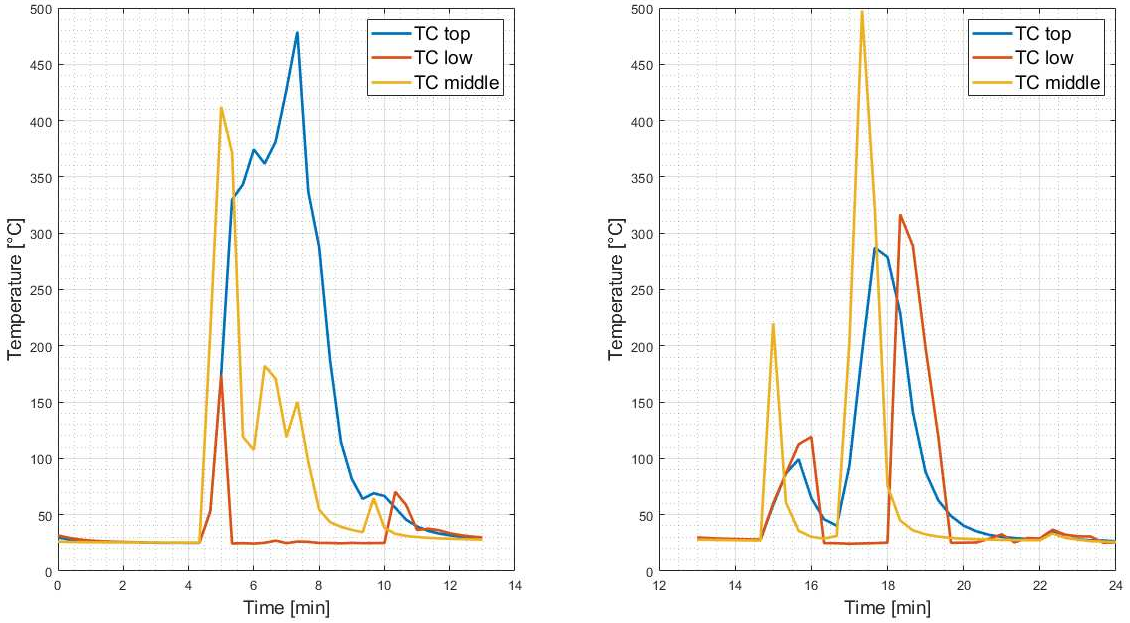

Figure 3.27: Result of the two tests performed with type-K thermocouples with 1/16 *in* diameter.

.

Profiles are highly irregular, with sudden temperature peaks which cannot be related to the rapid dielectric heating of SiC, but may be attributed to plasma formation at the thermocouple tip, due to field enhancement. This aspect is further suggested by the rapid decline of temperature, which can be attributed to the conduction of heat away from the point where plasma formed.
Profiles change between successive tests, indicating a highly irregular distribution of the temperature field inside the bed. The thermocouple placed in the lowest point (2 *cm* from the cavity bottom) sensed a low temperature in the first test; however, in the second test there was a peak up to 320°C. This behaviour was interpreted as direct consequence of the highly variable distribution of the electric field in the cavity. This typical feature of multi-mode MW ovens is further emphasized by the fact that dielectric properties of SiC are highly dependent of temperature; when part of the bed changes temperature, its ability to absorb or reflect the incident radiation may change, influencing the distribution of the electric field in the cavity. This effect has an impact on the thermal field of the bed; a loop is created, where the thermal field influence the electric field, and vice-versa. This aspect makes particularly challenging the prediction of the thermal field in the bed.
An additional observation is concerned with the thermocouple positioning. If the thermocouple is not centred, it is exposed to a stronger electric field, which may lead to strong Ohmic losses on the surface. This effect was visually confirmed, since a thermocouple became incandescent; the thermocouple was the one placed in the

middle of the bed in the second test; incandescence can be observed on the plot, since this thermocouple passed in less than a minute from 25°C to 500°C.
This test underlined the need of using thermocouples characterized by low curvatures at the tip (as to lower the effect of field intensification at the thermocouple tip), coupled with the need of using thermocouples rigid enough to be placed at the reactor centre without being curved in the assembly process; usage of external diameters of 1/16 *in* was therefore excluded, in favour of 1/8 *in* thermocouples.

A second test was performed, now with with a temperature control loop, implementing thicker thermocouples (1/8 *in*). The test's scheme is the same of Figure 3.27, with the only differences being the bed and thermocouples height. In Table 3.5 are reported the characteristics of both tests.

Table 3.5: Features of the tests where three thermocouples were immersed in the *SiC* bed. Granulometric class of *SiC* used is >1 mm.

# **Test**	**Bed height** [*cm*]	**TC height** [*cm*]	**TC diameter** [*in*]
1	10	2, 4, 8	1/16
2	6.5	3, 4, 5	1/8

Results of this second test are reported in Figure 3.28.

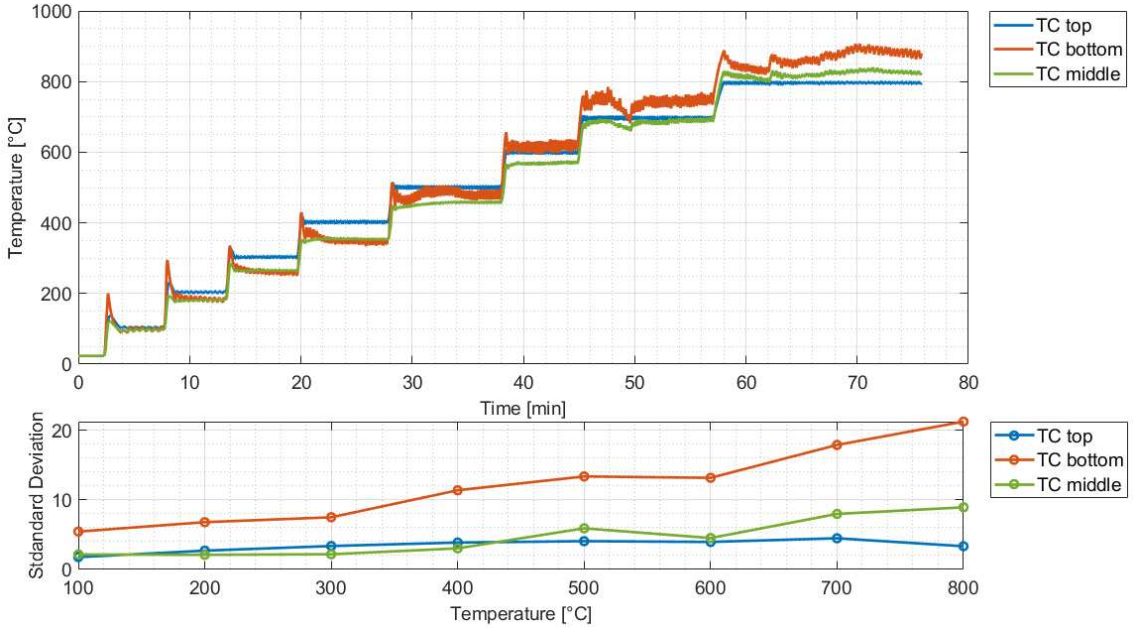

Figure 3.28: Result of the two tests performed with type-K thermocouples with 1/8 *in* diameter.

As it can be seen, large temperature spikes are absent in this case; profiles are much more regular if compared with the test performed with thermocouples of 1/16 *in* diameter. This effect may be interpreted as direct consequence of larger curvatures of the thermocouple tip, which implies lower field enhancements at the junction, with consequent lower possibility of dielectric breakdown; alternatively,

it may de traced back to the shielding effect of Silicon Carbide, related to the thermocouple's radial position, thus its exposition to intense electric fields. However, the uneven axial distribution of the thermal field within the bed remained; this effect is further amplified passing from low to high temperatures. Another aspect to be underlined is the oscillation magnitude, which seems to be particularly relevant for the lower thermocouple, reaching 40°C. The controlling thermocouple (placed at the top) do not show these oscillations, because they are limited by the control loop. In the figure, standard deviation of the three thermocouples at different temperatures is also reported.

3.2.2 Particle size

Particle size is another important factor to be considered in the setup. In fact, absorption and reflection of MW radiation depends not only on the material's nature, temperature and the radiation frequency, but also on the particle size distribution. This effect was reported in literature [61], and was attributed to the enhanced influence of the interfacial (Maxwell-Wagner) polarization phenomenon. In the article [61] it is underlined the relation between particle size (thus, ratio between the external area and the volume of the particle) and loss tangent. In particular, lower particle sizes are associated with enhanced heterogeneous interfacial polarization phenomena, which resulted in increased loss tangent, thus, increased capabilities of absorbing microwaves.

To determine how the granulometric class influenced the absorption of MW radiation in SiC, a test was set as shown in figure 3.29.

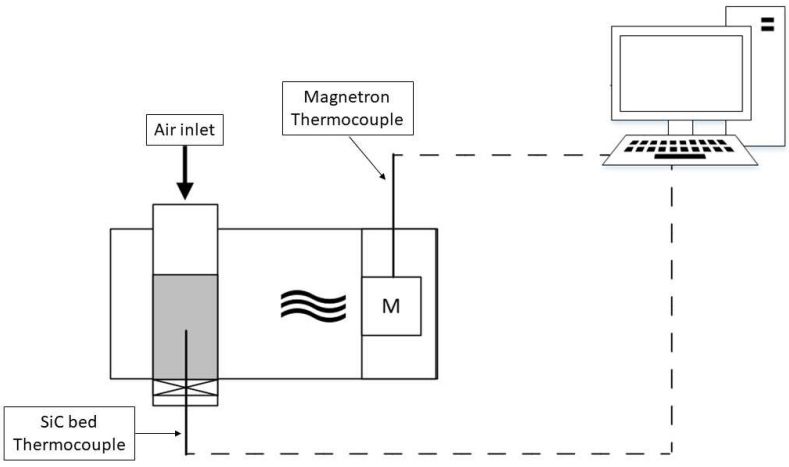

Figure 3.29: Scheme of the test performed to determine influence of the SiC granulometric class.

Due to the lack of instrumentation needed to measure the reflected radiation from the bed, this information was indirectly inferred. MW radiation, if not absorbed by SiC or lost in the environment (or in other type of losses not related with the catalytic bed), may be reflected back to the magnetron antenna. The antenna is coated with a metallic layer, which may be subject to Ohmic losses. As a result,

the magnetron temperature would increase; this temperature increase can then be monitored by the magnetron thermocouple, thus reflections may be studied with such monitoring system. Two tests were performed to determine this effect; in the first test, SiC having particle size of $0.85-1\ mm$ was used as absorber material, while in the second test the granulometric class was decreased down to $0.085 - 0.1\ mm$. Results of the test are shown in Figure 3.30.

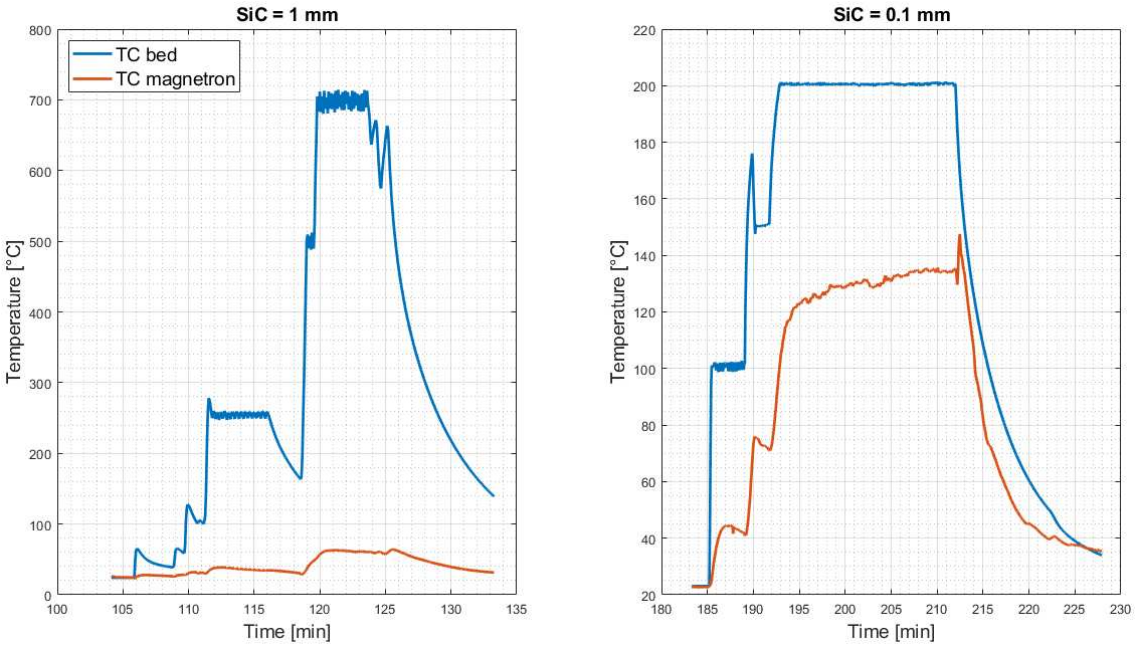

Figure 3.30: Temperature profiles of the tests performed with SiC of granulometric class of 1 mm (left) and 0.1 mm (right)

Larger SiC particles results in enhanced MW absorption, since the catalyst temperature easily reached 700°C, while the magnetron temperature remained lower than 100°C. However, larger oscillations in the bed temperature profiles were recorded. In contrast, in the test where 0.1 mm SiC was used, the bed temperature could not be raised over 200°C, since the magnetron temperature rapidly increased over 140°C, the limiting temperature beyond which the safety thermal switch activates.

This fact was interpreted as an inability of Silicon Carbide to efficiently absorb MW radiation when particle size is small. The observed behaviour is in contrast with the literature data (which, however, is not referred to SiC); from this fact it may be concluded that the Maxwell-Wagner polarization phenomenon is not important in SiC, thus other mechanisms of polarization must be involved. The effect was also observed in the test described in Figure 3.18, performed with a granulometric class of 1 mm (whose results were shown in Figure 3.19) and 0.1 mm, whose results are shown in Figure 3.31 and compared with these of Figure 3.18 at 1 mm. By using finer SiC particles the bed temperature do not raise above 300°C, while when coarser particles are used the temperature easily reach 600°C.

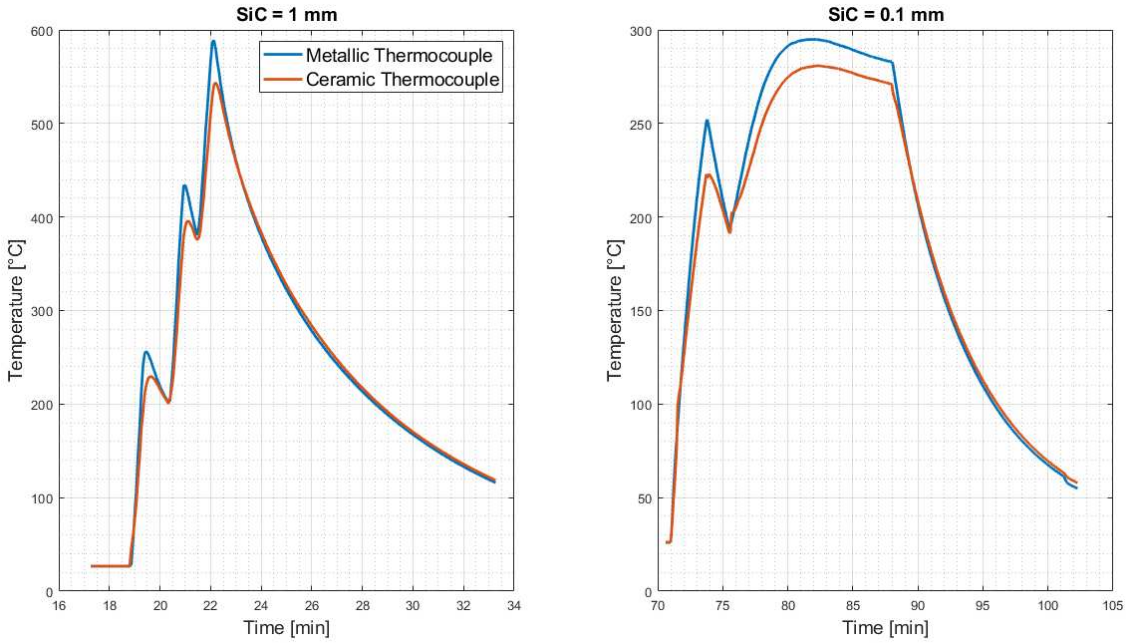

Figure 3.31: Temperature profiles of the tests performed with SiC of granulometric class of 1 mm (left) and 0.1 mm (right), with metallic and ceramic thermocouples.

To preserve the magnetron integrity, it was decided to implement larger particles size of SiC in the setup, as to maximise the fraction of absorbed radiation. In particular, since the Katalco 25-4^{TM} catalyst was available as granules of $1-0.85\ mm$, it was decided to grind and screen SiC down to this granulometric class.

3.2.3 Catalyst loading

The catalyst used to perform the MDR reaction is Katalco 25-4^{TM}, whose composition has been reported in Table 2.3. It consist in a support of low-dielectric $CaAl_2O_4$, with small concentrations of K_2O promoters (which ensure fine dispersion of active sites), with a consistent fraction of active NiO catalyst. The latter, when reduced to metallic Ni, is a metal; under MW radiation, it is expected to free electrons of the metallic bond, generating electric currents. It is desirable to lower as much as possible these electric currents, as to minimise the possibility of dielectric breaking at the thermocouple's tip; however, this effect must be balanced with the need of achieving high catalytic activities during the reforming reaction. The electric currents generated into the catalytic bed were determined by inserting the metallic thermocouple into the bed at various catalyst loadings; the thermocouple was then grounded via an electric wire, connected to the ground of the MW oven. The scheme of such test is reported in Figure 3.32. The voltage measured at various catalyst loadings was then read from the multimeter, and the relation between catalyst loading and voltage recorded was determined. The tests were performed by using similar amounts of catalyst, varying the dilution by adding SiC; results are shown in Table 3.6 and Figure 3.33. As it can be seen, the recorded voltage increases with increasing catalyst loadings, meaning that the metallic sites in the catalyst actively contribute to generation of electric currents. This is particularly evident when the total cata-

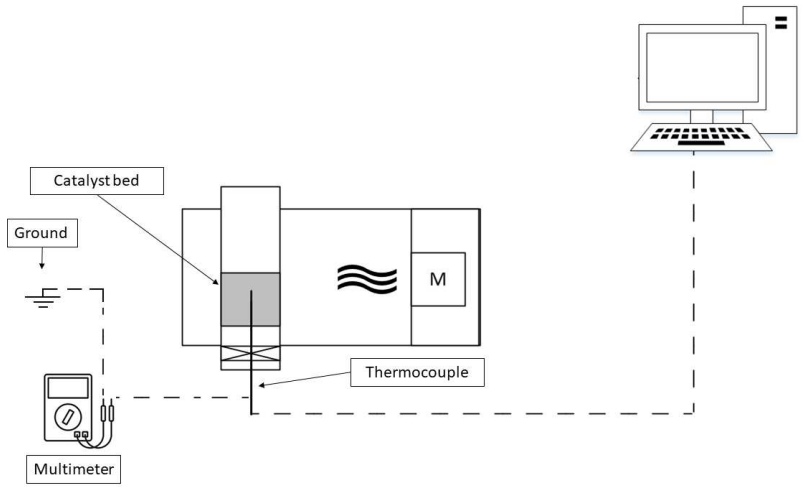

Figure 3.32: Scheme of the test used to determine the relation between catalyst loading and voltage.

lyst mass is changed, because the recorded voltage reached 3 V with 12.3 grams of catalyst, while it reduced to only 0.013 V with 1.61 grams. However, catalyst mass and loadings are not the only factors to be considered, since the amount of radiation absorbed depends on the volume exposed. In addition, when SiC is present in the bed, space between the catalyst particles is increased; thus, the distance d in the Paschen's law (Eq. 3.14) is larger, resulting in a higher ΔV required for dielectric breakage to take place.

Table 3.6: Voltage recorded at various catalyst loadings.

Catalyst mass $[g]$	**SiC mass** $[g]$	**Catalyst mass fraction** $[-]$	**Voltage** $[mV]$
12.32	0	1	3000
1.61	0	1	13
1.61	1.38	0.46	4.5
1.61	0.46	0.77	8

A satisfactory balance between catalytic activity, voltage recorded, and catalytic bed volume was found by implementing a catalyst mass fraction of $\omega_{SiC} = 0.2$. This resulted in a bed height of 2 cm circa, while the overall mass of catalyst and SiC was about 6 g. This configuration was implemented in both tests performed. To avoid excessive electric currents in the catalytic bed, which could produce unwanted electric discharges harmful for the thermocouple, the thermocouple was grounded in the following tests with the MDR reaction, as suggested also by literature ([23]). The main driver used to determine the optimal catalyst loading was also identified in operation safety, due to the presence in the catalytic bed of a gaseous fuel mixture which, in presence of oxygen infiltration from atmosphere (due to imperfect sealing of the reactor's junctions), could generate a flammable mixture, which may be ignited by the electric discharges in the catalytic bed.
To avoid undesired electric discharges in the bed, it was decided to ground the metallic thermocouple. Grounding allows to convey electric currents generated in

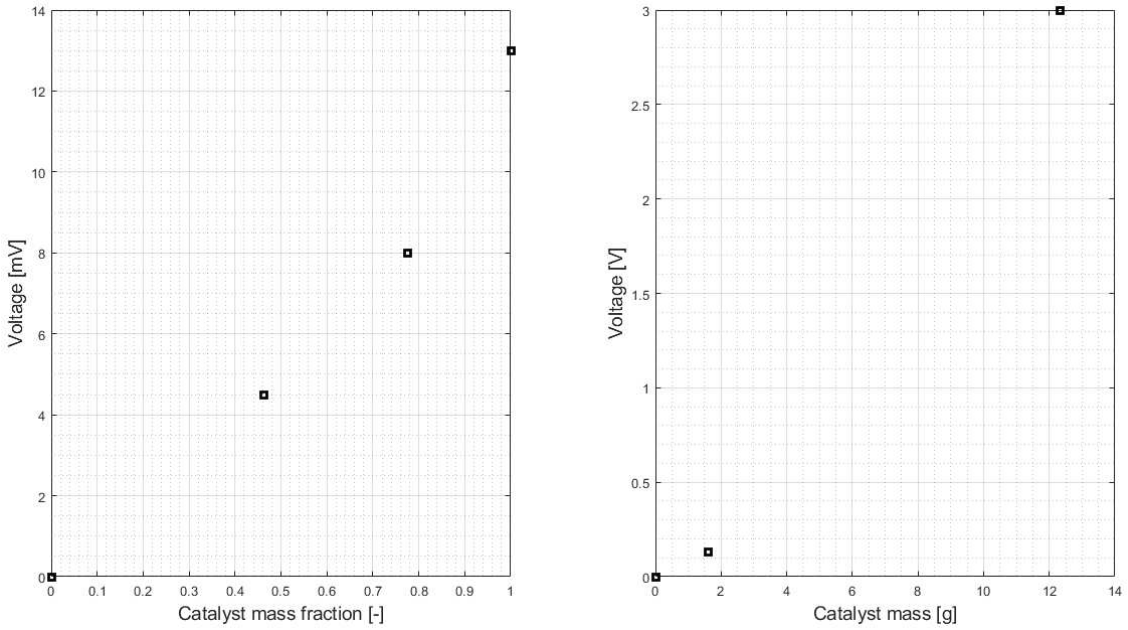

Figure 3.33: Relation between catalyst loading and voltage recorded by the multimeter (left); total catalyst mass is 1.61 g. Relation between catalyst mass and voltage (right).

the bed (or in the thermocouple sheath) toward a point at zero potential; by doing so, excessive charge accumulations in the bed was prevented, thereby reducing the risk of dielectric breakage. It must be noted that the presence of electric currents in the thermocouple sheath generate Ohmic losses, which may interact with the measure at the thermocouple tip. However, this effect was considered of minor importance.

3.2.4 Temperature distribution in the bed

An inherent problem of MW dielectric heating is related to the highly inhomogeneous temperature distribution in the load [39]. This problem cannot be completely avoided, unless the heating MW applicator is changed from multi-mode to single-mode or travelling-wave; however, it may be mitigated by implementing a rationalized design of the experimental setup. The load (reactor) thermal conductivity has a primary importance, since it allow a rapid relaxation of temperature gradients; Silicon Carbide is, in this context, one of the most suitable materials, due to the remarkable thermal properties, associated with chemical and mechanical resistances. Redistribution of heat inside the bed is enhanced by the presence of a convective flow, which contributes to lower the temperature of hot-spots. The gas phase flowing through the bed is heated by convection and radiation from the SiC particles, and these two heat transfer mechanisms allows to reduce the possibility of observing very large temperature gradients. To determine the thermal field inhomogeneity in SiC under MW heating, a series of tests were performed implementing three metallic thermocouples inserted in the bed as shown by Figure 3.26, under different conditions of bed heights and thermocouple position. Such conditions are reported

in Table 3.7; the thermocouple height is measured from the cavity bottom, while the controlling thermocouple is highlighted in bold character.

Table 3.7: Conditions of the tests; the controlling thermocouple is highlighted in bold character. The bed is composed of only SiC.

# Test	**Bed height** $[cm]$	**Thermocouple position** $[cm]$
1	6.3	3, 4, **5**
2	2.5	0, **1**, 1.5
3	2.5	0, **1**, 1.5

Test results are shown in Figures 3.28, 3.34 and 3.35. In the first test (already presented in Section 3.2.1), the controlling temperature is the top one. Temperature profiles between different thermocouples are similar at low temperatures; however, increasing the controlling thermocouple's set point lead to a change in the temperature distribution. In test #1, If the lowest thermocouple initially measured temperatures much lower than the controlling one, at high temperatures it measure the highest temperature of all the thermocouples. Changes of the temperature field as function of the temperature set point imposed to the controlling thermocouple are evident. This behaviour may be explained by considering how much the MW-absorption capability of SiC changes with temperature. Higher temperatures generally lead to higher MW absorptions, as Figure 3.21 shows; the fraction of reflected power will decrease, thereby influencing the electric field distribution in the oven cavity. With large bed heights, this may lead to unexpected behaviours like the profile inversion shown in the plot between two thermocouples. However, this effect is of small relevance when smaller bed heights are implemented, as Figures 3.34 and 3.35 shows. In these two tests, the controlling thermocouple is the middle one. In tests #2 and #3, the higher the thermocouple position, the higher the temperature measured. This can be traced back to the electric field distribution in the oven cavity, which simulations [18] shows to be very low in correspondence of the cavity bottom. The higher magnitude of the EM field at higher heights is underlined by the presence of peaks of the higher thermocouple, for low temperatures. Oscillations are, however, always present (except for the lowest thermocouple, which doesn't seem to be affected at all by the EM field). Another aspect to be stressed is the lower magnitude of oscillations for the controlling thermocouple. Temperature differences between the controlling thermocouple and the other ones is reported in Figure 3.36. As literature suggest, high axial temperature gradients are indeed present, thus the heating is highly inhomogeneous. Temperature gradients may be as high as 300°C, depending on the thermocouple position and bed location inside the cavity.

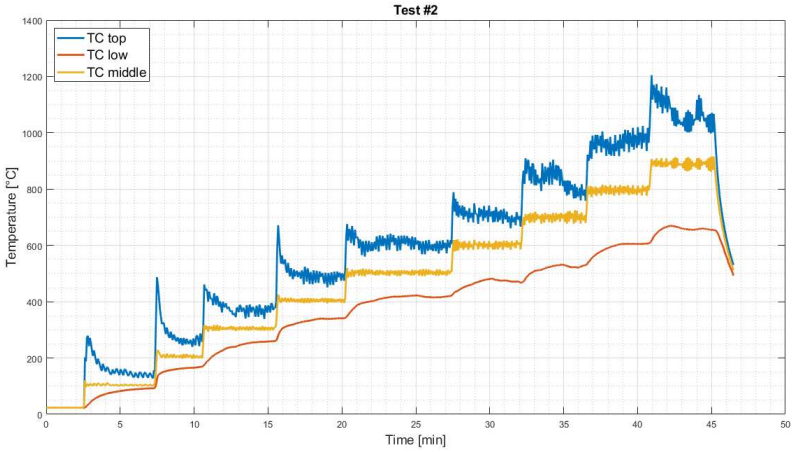

Figure 3.34: Temperature profiles of test #2.

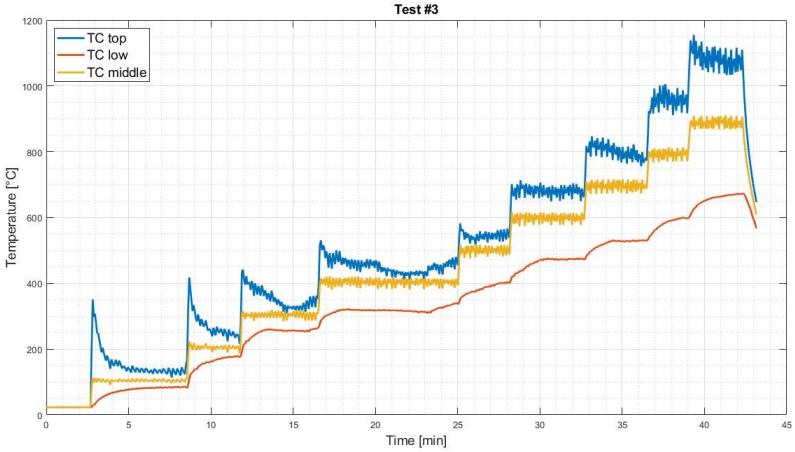

Figure 3.35: Temperature profiles of test #3.

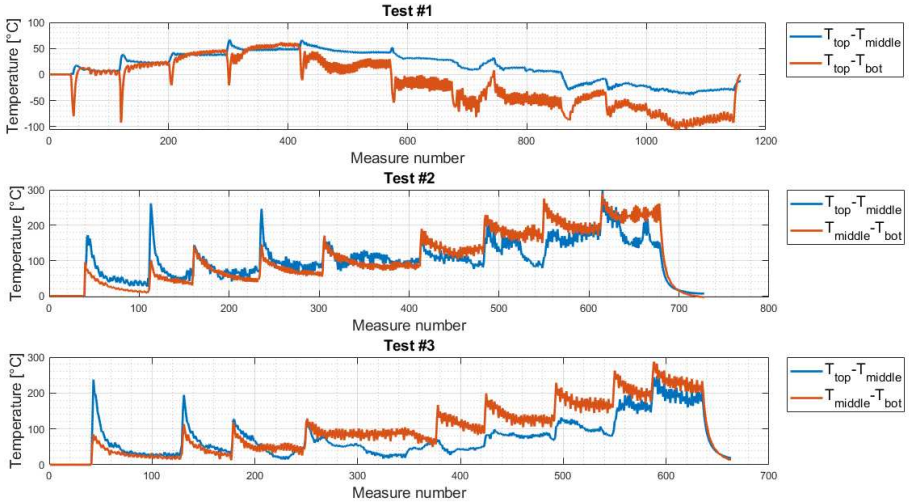

Figure 3.36: Temperature differences between the controlling thermocouple and the other two.

To determine how the temperature field in the bed evolved in time, a longer test was performed with the same experimental setup of Figure 3.26. The controlling thermocouple set point was imposed at 700°C and maintained for a long time (2 hours); thermocouples were placed in the same position of test #2, with the same bed height of 2.5 *cm*. Results of the test are shown in Figure 3.37; it is possible to see that here the temperature distribution is more stable than the case of different isotherms, even though the profiles of the non-controlling thermocouples are not very stable. Large temperature differences are found ($100 - 150$°C), despite the use of a small bed to limit the axial gradients.

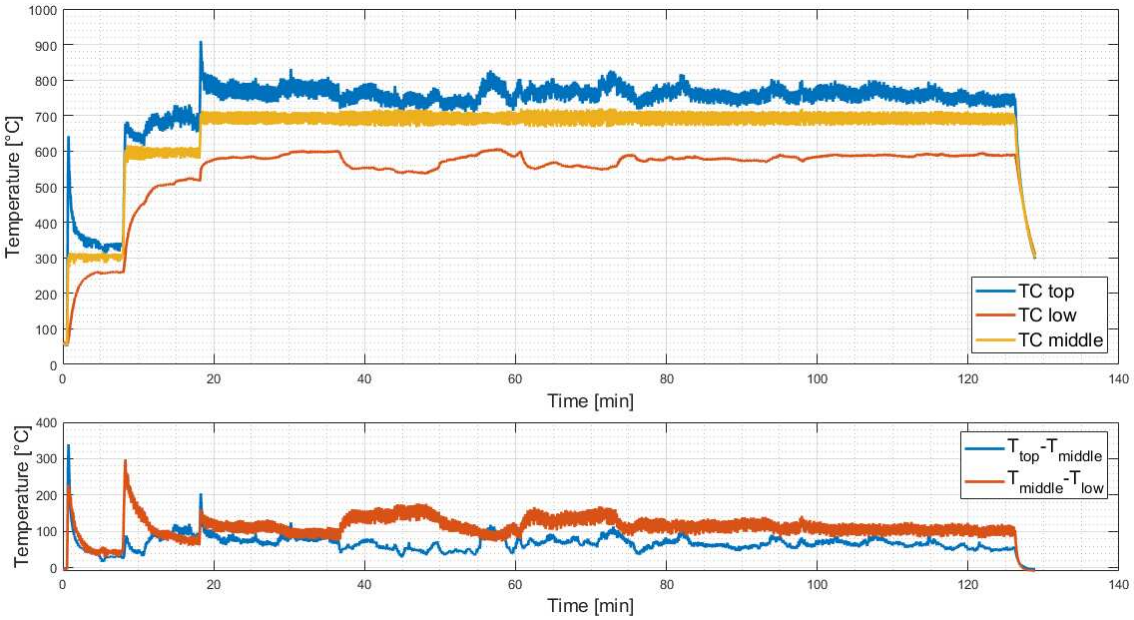

Figure 3.37: Temperature profiles of the test at 700°C for 2 hours (top); temperature differences between the controlling thermocouple (middle) and the other two.

3.2.5 Power drops on the electric line

When magnetron turns on, the MW oven absorb roughly 1100 W from the electric grid. This absorption is almost instantaneous, and generate an imbalance on the electric grid. As a result, all the electronic instruments connected to the grid are subjected to an instantaneous power drop. This fact is particularly relevant for the mass flow meters, whose set point instantaneously change of $\pm 2\%$ as result of the power drop on the electric line. As a result, the instantaneous mixture sent to the reactor is not the expected one, with an evident impact on the reaction performances. This problem may be solved by implementing two different strategies: by (i) connecting the MW oven to an electric line different from the one of the mass flow meters, or (ii) by adding a compensation volume before the reactor inlet. The first strategy could not be implemented, since every electric plug present in the laboratory was connected to the same electric grid. Thus, the second strategy was implemented.

3.2.6 Position of the catalytic bed in the cavity

Distribution of the EM field is strictly dependent on the presence of objects in the oven cavity. Wave reflections phenomena generates the multi-mode resonant configuration typical of common household oven. However, during the experimental campaign it was noted that the part of catalytic bed more prone to get red hot under MW heating was the part facing the waveguide outlet. This fact was exploited to achieve rapid dielectric heating, as to maximise the amount of radiation absorbed by the catalytic bed. Together with the considerations already exposed on the impact of Ohmic losses on the metallic thermocouple (section 3.1.3), on the importance of the bed height (section 3.2.4) and on the informations coming from the distribution of the EM field ([18]), it was decided to exploit a catalytic bed having an axial extension of $\sim 2.5\ cm$, located in correspondence of the waveguide outlet; with such configuration (reported in Figure 3.38), the thermocouple sheath results exposed to MW radiation; however, the tip is still shielded by the SiC layer.

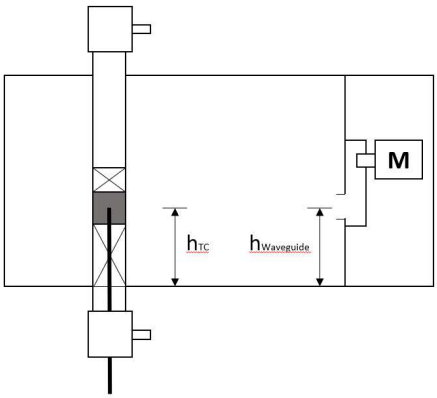

Figure 3.38: Relative position of the catalytic bed and waveguide.

3.2.7 Gas Hourly Space Velocity (GHSV)

The volumetric flowrate is an important factor in determining the performances of the catalytic reactor, due to its impact on (i) the convective heat transfer into the fixed bed, (ii) the residence time of gaseous phase inside the bed, and (iii) the amount of catalyst required. The gas-hourly space velocity is defined as

$$GHSV = \frac{\dot{V}_{tot}}{V_{cat}} = \frac{\dot{V}_{tot}}{A_r \cdot h_{bed}} \tag{3.26}$$

where $\dot{V}_{tot}$ is the total volumetric flowrate, A_r the reactor cross-size area, and h_{bed} the catalyst bed height. Values of GHSV were not randomly chosen; instead, a parametric study was performed to calculate it, by varying both the height of catalytic bed and the total flowrate. The resulting flowrates were then tested to determine the corresponding pressure drops in reactor, as to determine the maximum pressure drops that the quartz tube could handle. Pressure drops were measured in a series of tests; it resulted that junctions were able to withstand up to 1 bar of pressure drops across the bed, before leaks were observed.

The need for large catalytic bed surface areas (to maximise exposition to the EM field, thus MW absorption), low pressure drops (to avoid leakages from junctions), absence of dielectric breakdown in the bed (due to the presence of metallic catalyst), and homogeneous temperature distributions are all factors to be considered. To minimise the voltage generated in the catalytic bed, it was chosen to fix the catalyst mass at $\sim 6\ g$; thanks to the high SiC dilution ($\omega_{SiC} = 0.8$), the voltage measured (by implementing the setup shown in Figure 3.32) was limited to few mV, which was not considered sufficient to generate dielectric breakdown. Finally, it was decided to keep the bed height at 2.5 cm circa, as to lower as much as possible the temperature gradients in the bed (which cannot be eliminated). All these considerations lead to using a catalyst bed height of $3 - 5\ cm$, and a total flowrate of 300 mL/min circa, which resulted in a GHSV equal to 20000 h^{-1}.

3.3 Comparative study of Methane Dry reforming

In the following section, the main results of the MDR reaction carried under conventional heating and MW heating are exposed. First, results of the thermodynamic equilibrium study are discussed, to give a perspective of the equilibrium conditions. Then, the temperature policies of the MW-heating and conventional heating MDR reactions are presented; particular emphasis is posed on the MW heating temperature policy. The temperature policies are not the same, due to the inherent differences in the transients required for the catalytic bed to reach the isotherms. By means of the temperature policy comparison, results of both tests can be framed into the respective test conditions. MW heating is characterised by very short transients to reach the temperature set point; instead, under conventional heating this transient take few minutes. Carbon deposition over the bed during this transient cannot be neglected; to minimise this deposition, it was decided to switch off the reactant flowrates during the thermal transients, while feeding the reactor with only inert. Once the temperature set point was reached, the reactant flowrates were turned on again; clearly, this caused a temporary instability in the reactor temperature. In both heating policies, the reaction was studied in different isotherms ($500 - 600 - 700 - 800 - 900$°C); the isotherm was maintained until stabilization of GC measures, where possible. To determine the total amount of carbon deposited over the whole test, a TPO was performed after both tests.

3.3.1 Thermodynamic equilibrium study

Preliminary to the tests, the thermodynamic equilibrium of the MDR reaction was analysed. Equilibrium calculations were performed with two different software, namely *NASA-CEA* and *Cantera*. Both are based on a Gibb's free energy minimization algorithm; from the mathematical point of view, this is a constrained minimization (optimization) problem. The constraint is given by the atomic mass conservation law. Initial conditions specified in both software are listed in Table 3.8.

Table 3.8: Conditions used to determine the equilibrium concentration with *NASA-CEA* and *Cantera*. Cut-off species concentration is only present in *NASA-CEA*.

Variable	**Value**	**Units**
Pressure	1	bar
Temperature	200-1000	°C
$N^{in}_{CH_4}$	0.475	mol
$N^{in}_{CO_2}$	0.475	mol
N^{in}_{Ar}	0.05	mol
Cut-off concentration	10	ppm

The initial mixture studied is an equimolar mixture of Methane and Carbon Dioxide; Argon was added to the calculation, as to simulate the real mixture used in the experiments. The temperature range was divided in 50°C intervals, as to scan with significant resolution the entire temperature range. In *NASA-CEA* it is possible to specify some additional parameters preliminary to the calculation: those are (i) the species present at equilibrium, and (ii) the cut-off concentration value (below which the species is assumed to be absent at equilibrium). All the species suggested by the software were included. Several calculations were performed, to verify that the parameters listed above do not influence the results. Cases considered for equilibrium calculations in *NASA-CEA* are listed in Table 3.9.

Table 3.9: Conditions of the equilibrium calculations with *NASA-CEA*.

# Case	**Trace species** [*ppm*]
1	*Not specified*
2	100
3	10
4	1

Results of the calculations are shown in Figure 3.39; no differences were found among the different cases, neither between different software. The calculation algorithm is clearly not affected by the software used, or the conditions imposed. The Hydrogen radical was found to be present in case #4; however, its concentrations were slightly higher than the threshold, and was not comparable with the concentrations of other species. Thus, it was not included in the figure. Results of the equilibrium calculations were then compared with the ones of *Niko et al.* ([41]). For the case of equimolar mixture of CO_2, CH_4 at atmospheric pressure, perfect agreement with literature results was found, as can be seen from Figure 3.40.

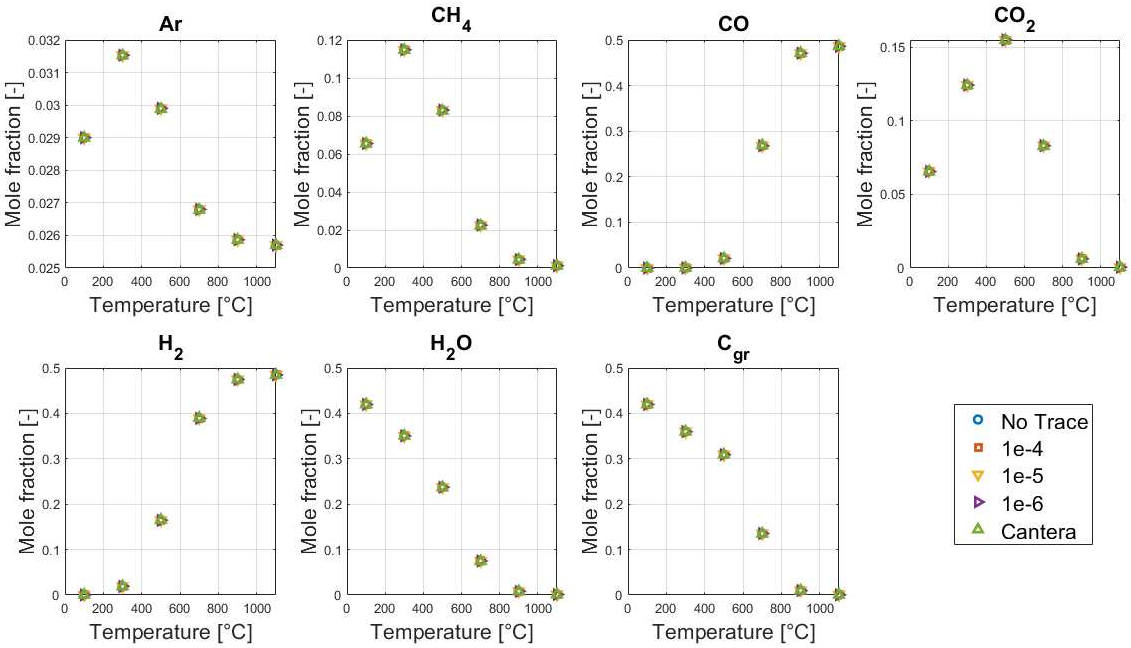

Figure 3.39: Comparison between equilibrium calculations of different software and different conditions.

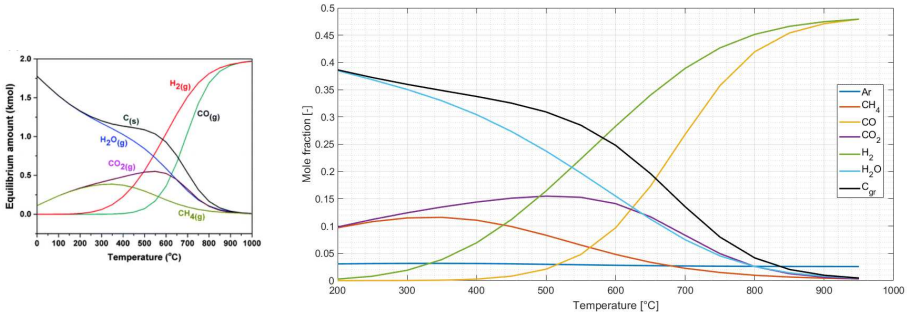

Figure 3.40: Comparison between equilibrium calculations from literature ([41], left) and the one calculated for this thesis work (right). The equilibrium composition includes all the species, including water and solid Carbon.

These calculations confirmed that both Carbon and Water formations is thermodynamically favoured at low temperatures; the right plot of Figure 3.40 show the equilibrium mole fractions of the entire mixture (included the solid carbon, belonging to a different phase); the equilibrium composition of the only gaseous species is instead reported in Figure 3.41.

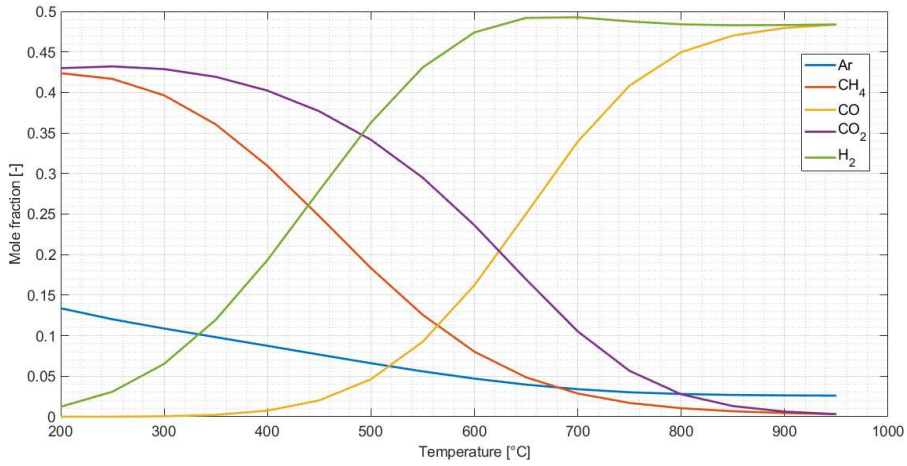

Figure 3.41: Equilibrium compositions of all the gaseous non-condensible species.

the mole fraction of the mixture in absence of Water and Carbon was evaluated as follows:

$$y_i^* = \frac{y_i}{1 - y_W - y_C} \tag{3.27}$$

where y_i is the equilibrium mole fraction of the whole mixture (including Water and Carbon), while y_i^* is the equilibrium mole fraction of the dry gas. Such results are in accord with the ones reported in literature ([41], section 1.2.1). The equilibrium conversions of both Methane and Carbon Dioxide were also evaluated. To perform this operation, the total number of moles at equilibrium was first calculated exploiting the Ar balance:

$$N_{tot}^{eq} = N_{tot}^{in} \cdot \frac{y_{Ar}^{in}}{y_{Ar}^{eq}} \tag{3.28}$$

Then, the number of moles of each species at equilibrium was evaluated as

$$N_i^{eq} = N_{tot}^{eq} \cdot y_i^{eq} \tag{3.29}$$

From the equilibrium moles of Methane and Carbon Dioxide, conversions was evaluated. Result of the calculation is reported in Figure 3.42.

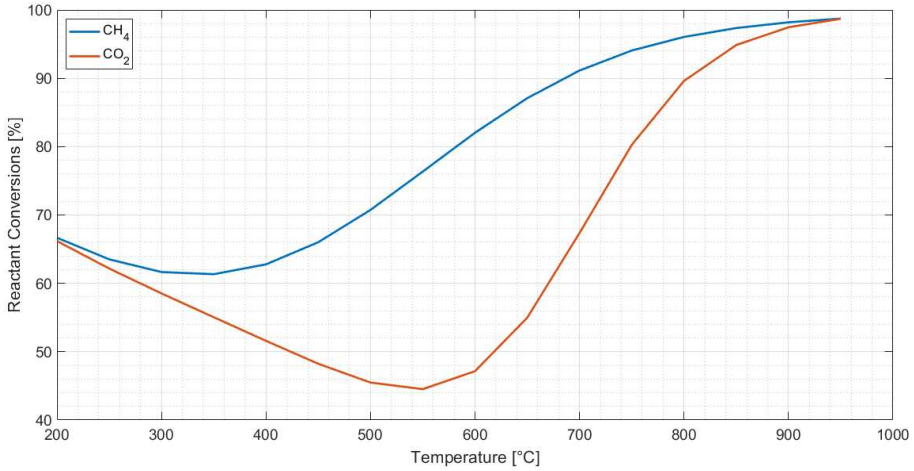

Figure 3.42: Equilibrium conversion of Methane and Carbon Dioxide.

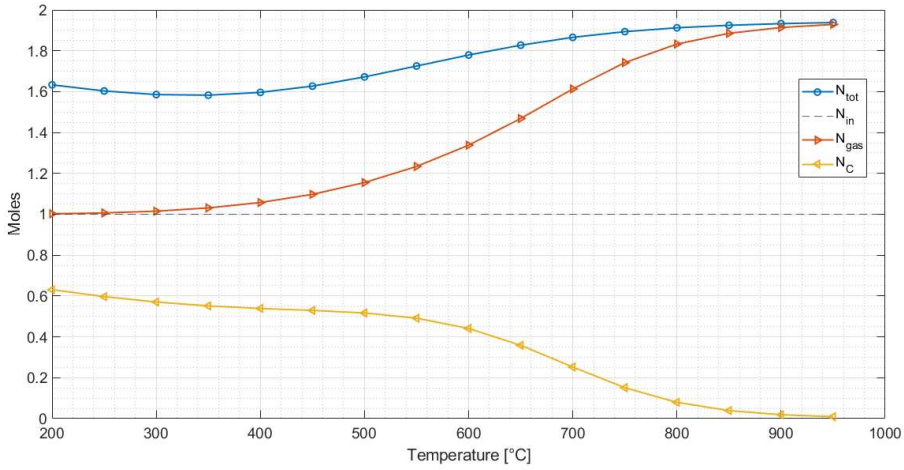

Figure 3.43: Number of moles of the gas and solid phases as function of temperature. The initial number of moles is reported as dashed line..

Figure 3.43 shows how abundant is the solid phase at low temperature in equilibrium conditions. In the figure the number of moles of the total mixture, gas phase and solid phase are shown; the solid phase is abundant at low temperatures, while decreases at high temperatures. Operating at high temperatures seems to be fundamental for (i) ensuring high product purity, due to the presence of only the MDR reaction, and (ii) preserving the catalyst activity, which is deactivated by the deposition of Carbon on active sites.

3.3.2 Temperature policy

In the following paragraph the temperature policies exploited in both tests are reported.

Microwave heating system

The temperature policy exploited for the MW heating system is reported in Figure 3.44. Test conditions are reported in Table 3.10; the overall duration of the test was about 8 hours. Temperature oscillations around the set point value are unavoidable, due to the on/off control logic implemented in the temperature control system. In addition, magnitude of oscillations increases passing from low to high temperatures; this fact can be traced back to the faster cooling of the bed, due to the larger temperature gradient between gas and solid phases. The last isotherm is characterised by a duration much lower than the other isotherms; this is caused by the loss of thermal control on the bed, as shown by Figure 3.45. Loss of control was attributed to the deposition of Carbon on the catalyst, which may be related to the fact that carbon is deposited in its crystalline form, graphite, which is a conductor; as result, MW radiation would be reflected (typical behaviour of good electrical conductors) and not absorbed by SiC; this effect was suggested by literature studies ([19]), but experimental validation of the crystalline structure under which Carbon is deposited is missing, due to the TPO performed after the test to evaluate the amount of carbon deposited.

Table 3.10: Isotherm durations for the test under MW heating.

Isotherm *[°C]*	500	600	700	800	900
Duration *[min]*	120	100	170	100	8

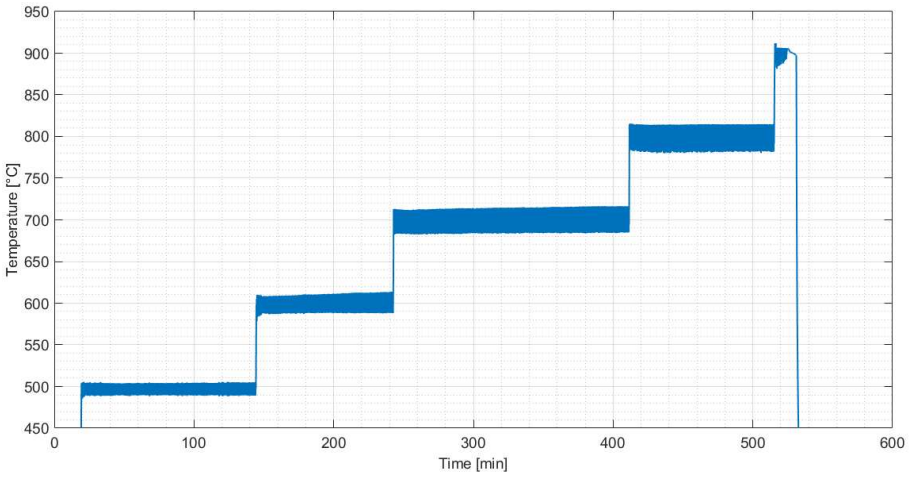

Figure 3.44: Temperature policy of the test under MW heating.

The loss of control is highlighted in Figure 3.45, where a zoom of the 900°C isotherm is reported.

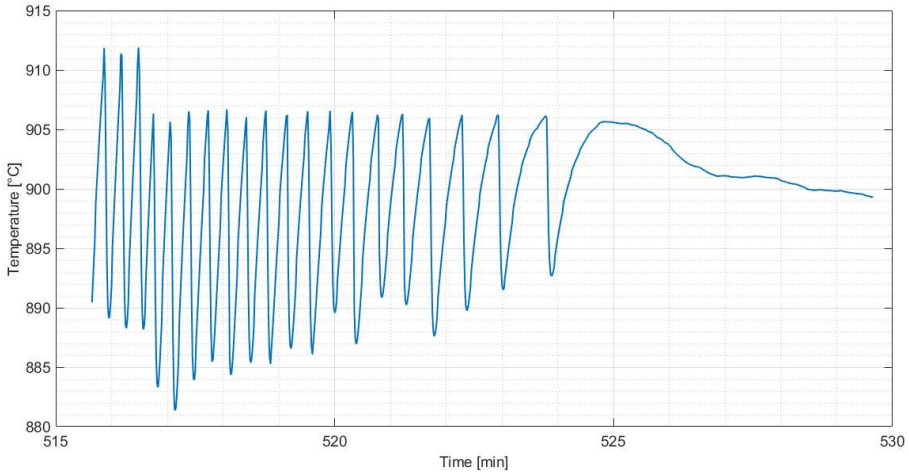

Figure 3.45: Zoom of the 900°C isotherm.

Temperature plays a central role in the crystalline form in which Carbon is deposited. For $T < 900$°C it may be possible that carbon is deposited in its amorphous form, enhancing the MW-absorption capabilities of the bed; however, over 900°C deposition may take place in crystalline form, leading to MW reflection, thus, the impossibility of controlling the bed temperature. This possibility is further confirmed by the fact that oscillations at 900°C are stable at the beginning, where only amorphous carbon exist, while are more and more spaced as the graphitic carbon is gradually deposited. MW reflection imply a modification of the EM field distribution

in the cavity oven, which may also result in a lower field intensity in correspondence of the bed. The test was interrupted, due to the sudden increase of the magnetron temperature after the loss of control. In addition, at 800°C hotspots were noticed in correspondence of the deposited Carbon (which was dragged down due to the presence of convective fluxes), which suddenly became red hot for 10 seconds circa. This behaviour was not found to be constant in time, but completely random; it was interpreted as a momentary increase of the EM field strength in that point, which lasted for 10-15 seconds.

Conventional heating system

Temperature control in conventional heating system is operated by the software *CX-Thermo*. The temperature policy exploited for this test is reported in Figure 3.46, while isotherm durations are listed in Table 3.11.

Table 3.11: Isotherm durations for the test under conventional heating.

Isotherm *[°C]*	500	600	700	800	900
Duration *[min]*	60	240	130	90	100

During the temperature ramps, both the Methane and Carbon Dioxide flowrates were turned off, as to minimise Coke deposition.

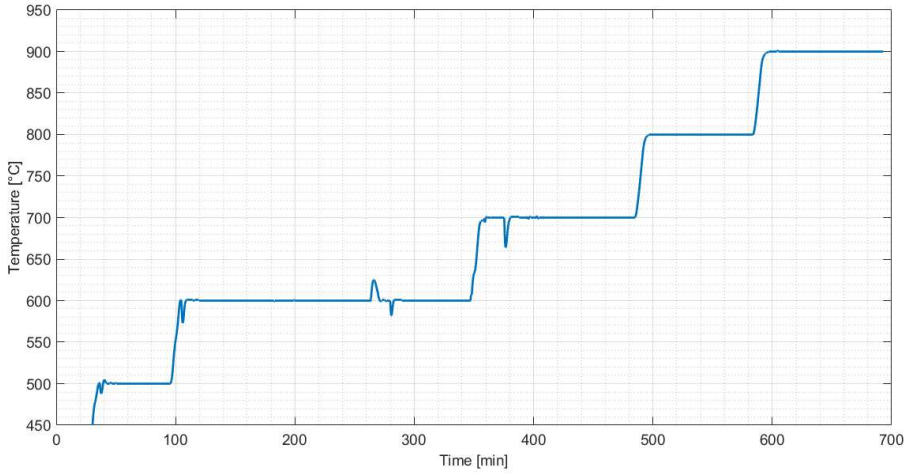

Figure 3.46: Temperature policy of the test under Conventional heating.

3.3.3 Comparison of MDR by heating technologies

In the following paragraph, performances of the two heating systems are compared. Conditions of both tests are reported in Table 3.12. The bed mass is referred to the mixture of *SiC* and catalyst; the GHSV and WHSV are instead calculated on the catalyst mass only.

Table 3.12: Operating parameters used in both tests.

Heating system	Units	Microwave	Conventional
ID reactor	$[mm]$	18	18
GHSV	$[1/h]$	20195	20015
WHSV	$[mL/mg\ h]$	14.88	14.17
Bed mass	$[g]$	6.93	5.39
Bed height	$[cm]$	2	1.7
Catalyst mass fraction	$[-]$	0.2	0.2
SiC mass fraction	$[-]$	0.8	0.8
Volumetric Flowrate	$[mL/min]$	342.60	254.65
Pressure	$[bar]$	1	1
x_{CH_4}	$[-]$	0.477	0.474
x_{CO_2}	$[-]$	0.473	0.475
x_{CAr}	$[-]$	0.049	0.04

It must be noted that, in order to observe discharges taking place under MW heating, the reactor was not insulated during the reaction tests. Thus, heat losses may play a fundamental role in determining the system's performances.

Mole fractions of the dry products

Molar fractions of the dry gas phase in the outlet of both reactors are reported versus temperature, for all the species, in Figure 3.47.

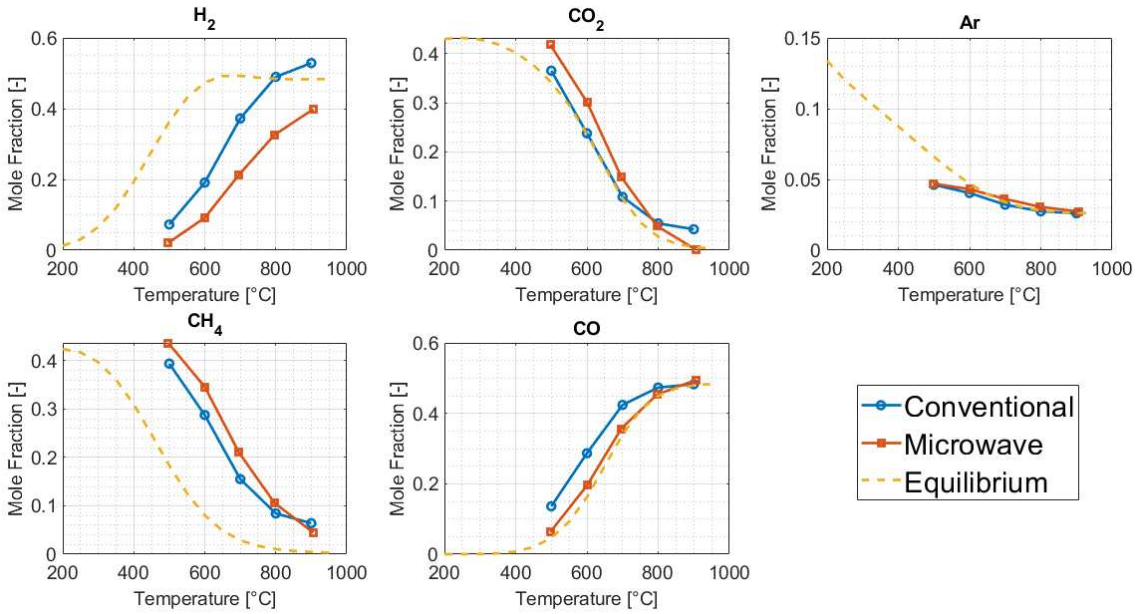

Figure 3.47: Gas-phase compositions as a function of temperature.

As a reference, the equilibrium composition is also reported. Apart from measures performed at 600°C, all the other isotherms are characterized by a fairly stable outlet gas composition; a long transient seems to be present at 600°C, specially under the conventional heating system. The MDR reaction takes place above 500°C,

with an almost complete conversion of Methane and Carbon dioxide at very high temperatures (900°C). Concerning Hydrogen and Methane compositions, their profile is far away from the equilibrium one; Hydrogen concentration is particularly low in the MW-heating system. In addition, Methane is less converted under MW radiation. Carbon Monoxide and Dioxide are much closer to the equilibrium compositions; for CO under MW heating, the outlet compositions perfectly overlap the equilibrium profile. In conventional heating, CO seems to be far from equilibrium at low temperatures, while approaches equilibrium at high temperatures. Carbon dioxide behaviour is instead inverted, if compared to CO; the conventional heating system seems to show higher conversions, for the same measured temperature. It must be noted that the Gas Chromatograph available in the laboratory cannot detect water, due to the presence of Zeolite columns, highly susceptible to water. Thus, water was condensed; this fact implies that it is impossible to determine the amount of water formed during the reaction. However, water in the products was confirmed (in both heating systems) by the presence of condensed droplets at the reactor outlet, as shown by Figure 3.48. The long transient at 600°C can be observed in Figure 3.49; stabilization of composition profiles could not be achieved in roughly 3 hours. The same transient is observed in the conventional oven, as shown by Figure 3.50.

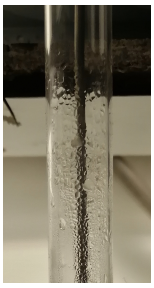

Figure 3.48: Condensed water at the oven outlet in the MW heating system.

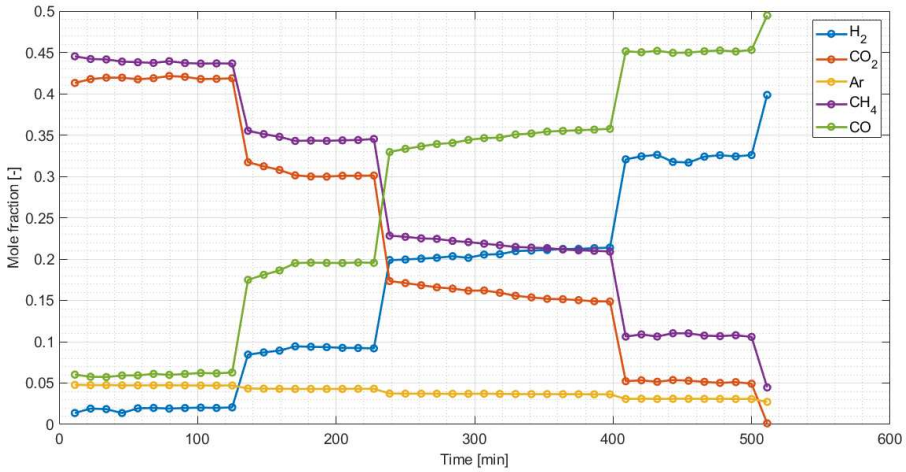

Figure 3.49: Time profiles of the dry gas from the reactor in the MW heating system.

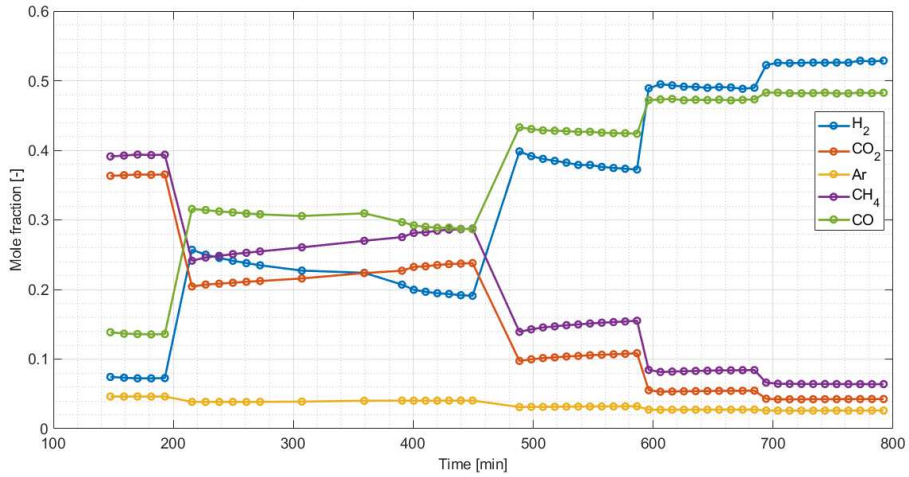

Figure 3.50: Time profiles of the dry gas from the reactor in the Conventional heating system.

Reactant conversions

Figure 3.51 shows the conversions of both reactants (Carbon Dioxide and Methane) for the conventional and MW heating system, compared with the equilibrium conversions. It can be noted that CO_2 conversion is higher than CH_4 conversion at any temperature. Due to the complex set of reactions listed in Table 1.12, many different combinations of reactions may be responsible for this behaviour. However, it is noted that the conventional heating system is characterized by higher performances, except for the measures performed at very high temperatures (800-900°C). At the same time, it is noted the presence of long transients at 600°C for the conventional heating system, which are not present (or highly reduced) for the MW heating system.

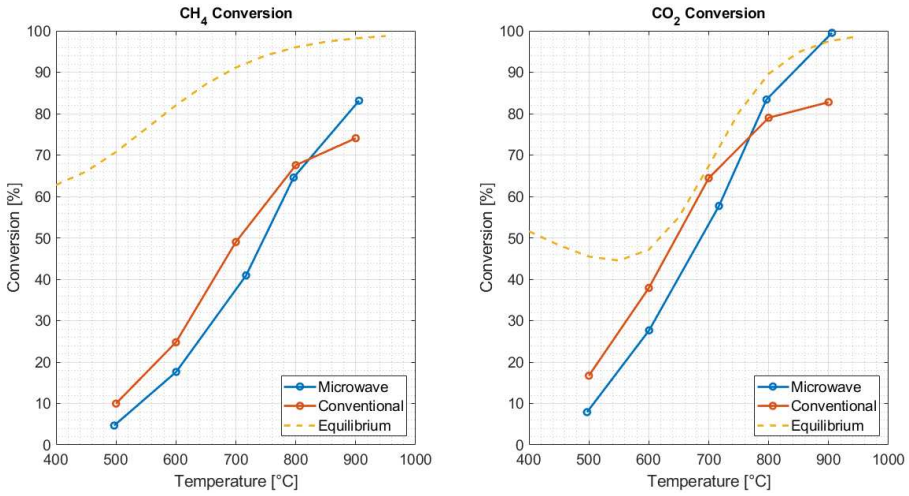

Figure 3.51: Conversions of reactants: CH_4 on the right, CO_2 on the left.

Selectivity

Different definitions for selectivity are used in literature. Here, selectivity of product P with respect to the reactant R is defined as

$$S_{P|R} = \frac{N_P^{out} - N_P^{in}}{N_R^{in} - N_R^{out}} \frac{\nu_P}{|\nu_R|} \tag{3.30}$$

where N is the molar flowrate, and ν the stoichiometric coefficients ($\nu_R = -1$, $\nu_P = +2$).

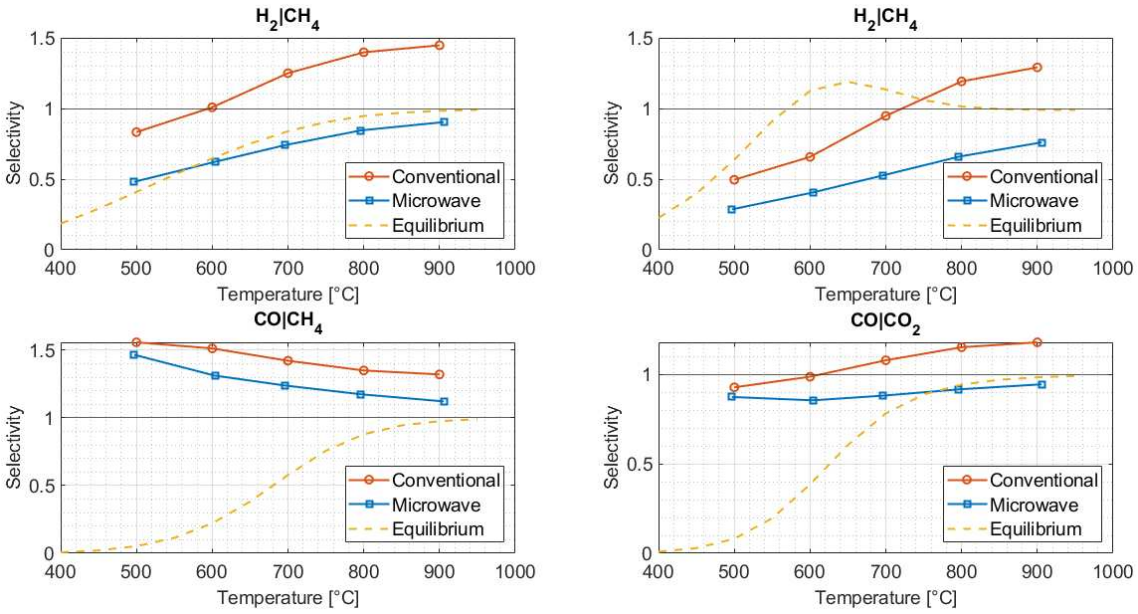

Figure 3.52: Selectivity of Hydrogen and Carbon Monoxide with respect to different reactants.

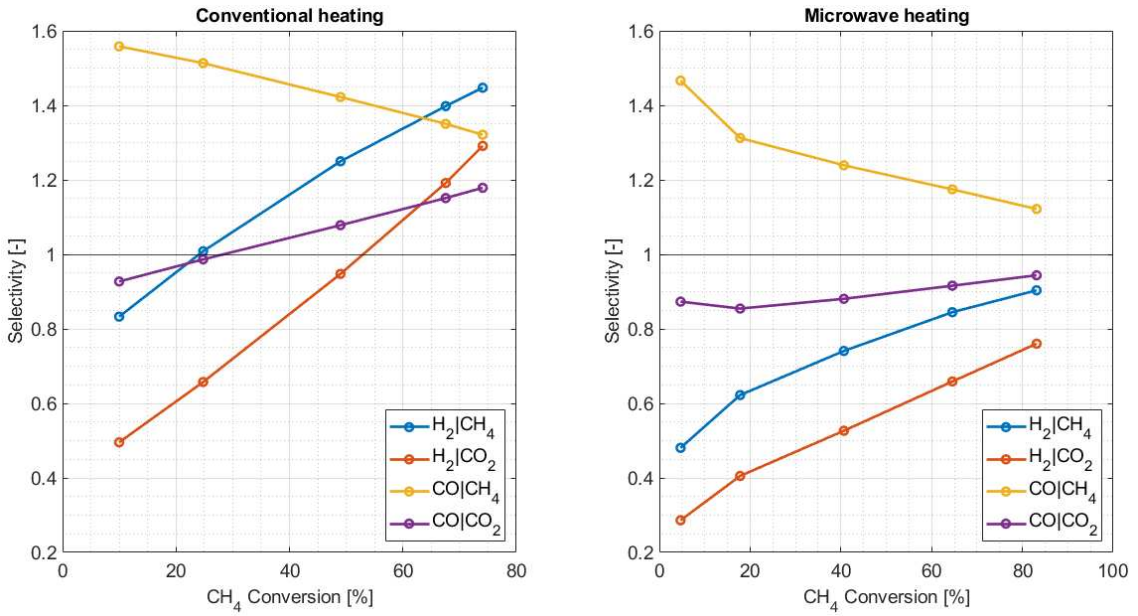

Figure 3.53: Selectivity-Conversion plot.

Selectivity is therefore scaled on the stoichiometric coefficients, which are the ones of MDR. For single reactions, this definition is bounded between 0 and 1 (where 0 indicate that no product is produced from the given reactant, while 1 indicate that all the reactant is converted only in the selected product). However, in complex sets of reactions, as the one involved here, selectivity may exceed unity. As Figures 3.47, 3.51 and 3.52 shows, in any case the conventional heating system shows higher performances than the microwave oven. Figure 3.53 reports the trend of selectivity as function of reactant conversions; it can be seen that in both heating systems, CO selectivity is higher at any conversion. However, H_2 selectivity from methane increase over unity in the conventional heating system, while approach unity in the MW heating system. Generally, selectivity increases at higher Methane conversions; at high temperatures, only MDR takes place, while secondary reactions are reduced. The differences in product selectivity between the two heating systems may be induced by a purely thermal effect; however, this effect may also be determined by the presence of interactions between the MW radiation and the reaction taking place on the catalyst, which may activate different sets of reactions.

Product Ratio

The ratio H_2/CO is reported in Figure 3.54. It can be seen that this ratio is higher in the conventional heating system than in the MW heating system; more Hydrogen is produced under conventional heating. This effect may be determined by the inhomogeneous Temperature distribution in the catalytic bed under MW heating, or by the interaction between microwaves and the chemical reaction.

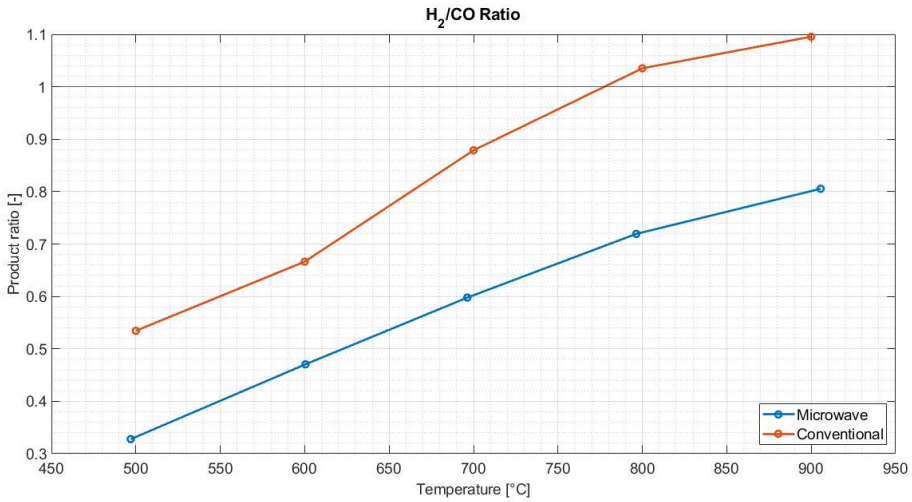

Figure 3.54: Ratio of Hydrogen to Carbon Monoxide at different temperatures, for both heating systems.

In presence of only Methane Dry reforming, the product ratio is equal to one, due to the reaction stoichiometry:

$$CH_4 + CO_2 \leftrightarrows 2CO + 2H_2 \tag{3.31}$$

Ratios lower than one indicate either that (i) H_2 produced is lower than the expected one, and (ii) CO produced is higher than expected. Such reactions has to be sought among the ones listed in Table 1.2.

Deposited Carbon

Carbon deposition is a known problem in the MDR reaction. As the thermodynamic equilibrium shows, its formation is expected at low temperatures; thus, it is fundamental to operate the process at high temperature to limit its production rate, as to ensure a long catalytic activity. The amount of carbon deposited was determined by means of a TPO, performed in both cases in the conventionally heated system. Conditions of both TPO are reported in Table 3.13, while the profiles of CO, CO_2 in time are reported in Figure 3.55.

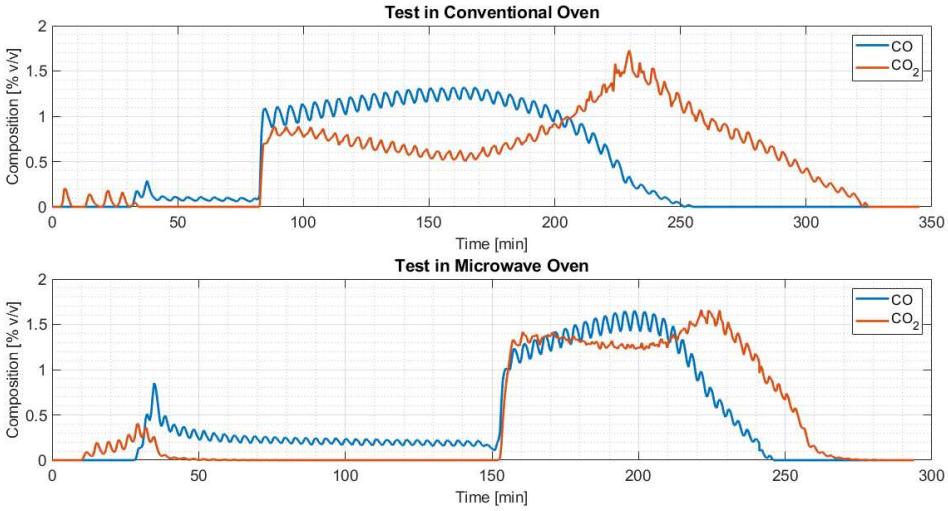

Figure 3.55: Time profiles of CO, CO_1 for the TPO tests for both heating systems (top: conventional heating test; bottom: microwave heating test).

The amount of carbon formed in both tests is reported in Table 3.14. The total reaction test duration, as well as the isotherm test duration, have huge effects on Carbon deposition; the longer the isotherms at low temperatures, the higher the amount of Carbon deposited. From the TPO it was concluded that more carbon is formed under the conventional heating system.

Table 3.13: Operating parameters used for both TPO.

Parameter	Microwave	Conventional
Total flowrate $[mL/min]$	199.23	199.78
Oxygen Flowrate $[mL/min]$	4.005	3.91
Inert Flowrate $[mL/min]$	195.22	195.86

Table 3.14: Total amount of carbon, as determined by the TPO.

Microwave heating system	**Conventional heating system**
$m_C = 222.95\ g$	$m_C = 334.88\ g$

Dividing the amount of Carbon obtained by the mass of catalyst and test duration, it is possible to define a parameter that is not affected by these two variables. However, the duration of each isotherm is a critical variable that influences carbon deposition.

$$Par = \frac{m_C}{m_{cat} \cdot \Delta t_{test}} \tag{3.32}$$

Table 3.15: Total amount of carbon, scaled on test duration and catalyst mass.

	Microwave	**Conventional**
Par $[mg/g_{cat}h]$	14.5	36.4

Values of such parameter for both tests are reported in Table 3.15; it is possible to observe that the rate of Carbon formation is formed under conventional heating is more than twice the MW one.

Carbon balance

During the MDR reaction, carbon is thus deposited on the catalytic bed. As a consequence, part of the C entering in the system will not be found in the C-bearing species at the reactor outlet. The Carbon balance may provide indications on the amount of carbon that is instantaneously deposited on the catalytic bed, under the assumptions that (i) carbon entering is converted into CO only, thus no other product is generated, (ii) carbon is the only form under which the inlet C atoms can deposit. In both tests, the carbon balance was calculated as described by Eq. 3.33; results of the calculation are shown in Figure 3.56.

$$\epsilon_{C,\%} = \frac{\dot{N}_C^{in} - \dot{N}_C^{out}}{\dot{N}_C^{in}} \cdot 100 \tag{3.33}$$

Positive errors indicates that there's accumulation of Carbon in the fixed bed, which is reasonable; instead, negative errors implies that Carbon is being removed from the catalytic bed. Under conventional heating, the Carbon error is reduced passing from low to high temperatures. This effect is in agreement with the equilibrium calculations, since at high temperatures carbon formation is hindered. At 900°C in particular, error is zero, meaning that no carbon is being deposited on the catalyst; at low temperatures instead, the calculated unbalance approaches 10%. Concerning the result obtained for the MW heating system, negative errors may be determined by two reasons: (i) measurements errors or (ii) involvement of the SiC bed in the reaction. The latter hypothesis is unlikely, due to the characteristic chemical inertness of Silicon Carbide, even in presence of hot spots into the bed. More likely, negative errors can be attributed to errors in the methane measurement into the gas chromatograph (by TCD).

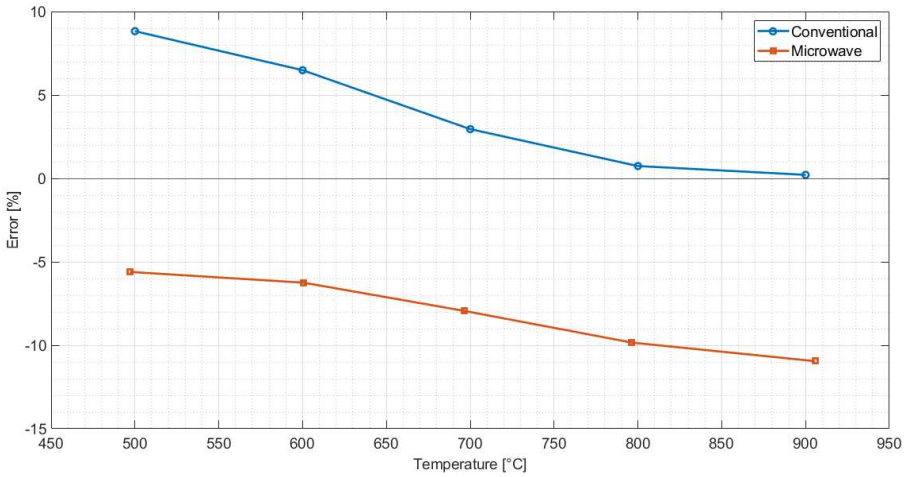

Figure 3.56: Error on Carbon as function of temperature.

Integrating the Carbon error, it is possible to alternatively estimate the amount of C deposited during the test. This estimation was performed though the TPO; results of both calculation techniques are reported in Table 3.16. For the conventional heating system, the results are in very good agreement (with a difference of 4.4% between the two values).

Table 3.16: Comparison of Carbon deposited from the TPO and from the Error balances, for both heating systems. Results expressed in mg.

Method	**Microwave**	**Conventional**
ϵ_C	-598.69	350.24
TPO	222.95	334.88

Pressure drops

Pressure drops plays a fundamental role in ensuring the operational safety. In fact, when excessive pressure drops in the reactor takes place, joints may not seal the reactor, producing a leak of a flammable gaseous mixture, which may be ignited by the contact with the hot oven. However, due to the fact that a large granulometric class is implemented, and the reactor height is low, pressure drops are small. In Figure 3.57 the typical pressure drop profile for both tests is reported; it is possible to observe that the maximum pressure drops are equal to 0.13 bar, which is an order of magnitude lower than the maximum pressure drops allowed in the reactor. On an isotherm, the increase of ΔP is related to the deposition of carbon on the catalyst, which clog the channel through which the gas can flow. As a result, the gas phase velocity is increased, and the pressure drops increases too. In fact, pressure drops in a packed bed reactor of spheres may be described by the Ergun's equation:

$$\frac{\Delta P}{\Delta L} = \left(\frac{150\mu(1-\varepsilon_{bed})^2}{\varepsilon_{bed}^2 D_p^2}\right)u + \left(\frac{1.75\rho(1-\varepsilon_{bed})}{\varepsilon_{bed}^2 D_p}\right)u^2 \tag{3.34}$$

where μ is the gas-phase viscosity, ε_{bed} the bed voidage, and D_p the particle diameter (assumed as a spherical particle) and u the gas phase velocity through the bed. In a

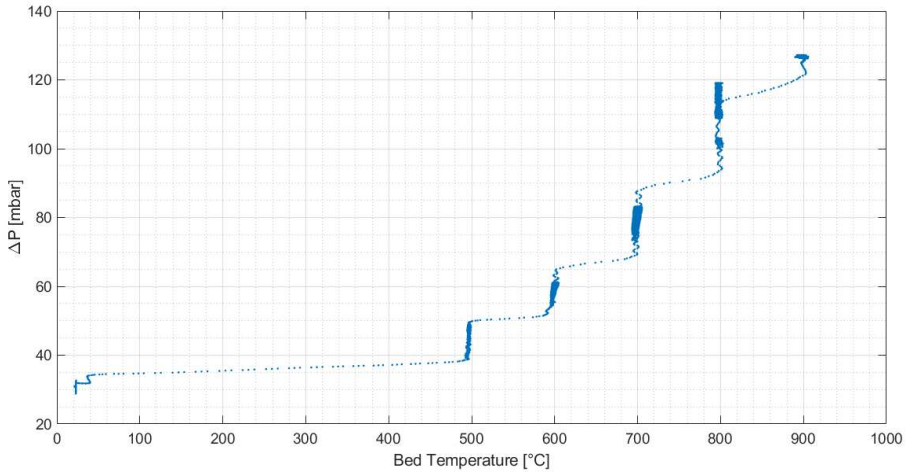

Figure 3.57: Typical profile of pressure drops for both heating systems.

turbulent system, pressure drops per unit length increase quadratically with velocity; thus, channel clogging result in higher velocities, and larger pressure drops, as well as lower contact time between catalyst and gas. Due to the similarity of flowrates and bed height, the profiles are basically equal in both tests. Thus, it was reported only the profile of pressure drops in the microwave heating system.

Power and Cumulative Energy required by the systems

In the conventional heating system, electric power is required to heat the resistances in the oven; in the MW heating system, instead, power is required to feed the magnetron and the other electrical components required to make it work. The maximum power required by both heating systems is reported in Table 3.17.

Table 3.17: Power required by both heating systems.

	Microwave	**Conventional**
Maximum Power $[W]$	1100	400

By knowing the profile of the instantaneous power used by the systems, it is possible to determine the total amount of energy required to perform the MDR reaction. In the MW heating system, instantaneous power is measured by the Wattmeter; the instrument is able to perform roughly one sample per second. The oven absorb 1100 W circa (at ambient temperature) from the electric grid. Energy consumption of the other electrical components of the MW oven is negligible, as shown by Table 3.18.

Table 3.18: Power required by the accessory components of the MW oven.

Component	**Power consumption** $[W]$
Magnetron fan	16
Temperature controller	1.7
Oven (Magnetron off)	39.7

All together, these components consume less than 5% of the power required when the magnetron is on. In the conventional heating system instead, power is measured by the software *CX-Thermo*, used to control the oven; power is modulated via the PID logic control embedded in the software. Power measured in the sampling interval is defined as

$$P(\Delta t) = \frac{E(\Delta t)}{\Delta t} \tag{3.35}$$

where Δt represents the measurement interval. Energy can be calculated by performing an integration of power, as shown by Equation 3.36:

$$E_{tot} = \int_{t_0}^{t_{end}} P(t)dt \simeq \sum_{t_0}^{t_{end}} P(t)\Delta t \tag{3.36}$$

It must be noted here that a representative measure of the overall energy for the MW oven would require (i) a continuous measure of power, which allows to perform measurements at a higher sampling rate, and (ii) a measure of the reflected and lost radiation power. Due to the lack of instrument required to perform such measurements, energy calculations for the MW oven will be referred to the power subtracted from the grid, not the one delivered to the catalytic bed. Due to the much higher power requirements of the MW oven with respect to the conventional oven, it is expected that energy required by the MW oven is much higher than in the case of conventional heating. Profiles of both instantaneous power and cumulated energy are reported in Figure 3.58. The overall energy consumption of the MW oven is around 20.2 MJ, which is 2.47 times higher than the conventional oven energy consumption. However, this value do not account for the different test durations, and for the presence of radiation losses in the MW oven.

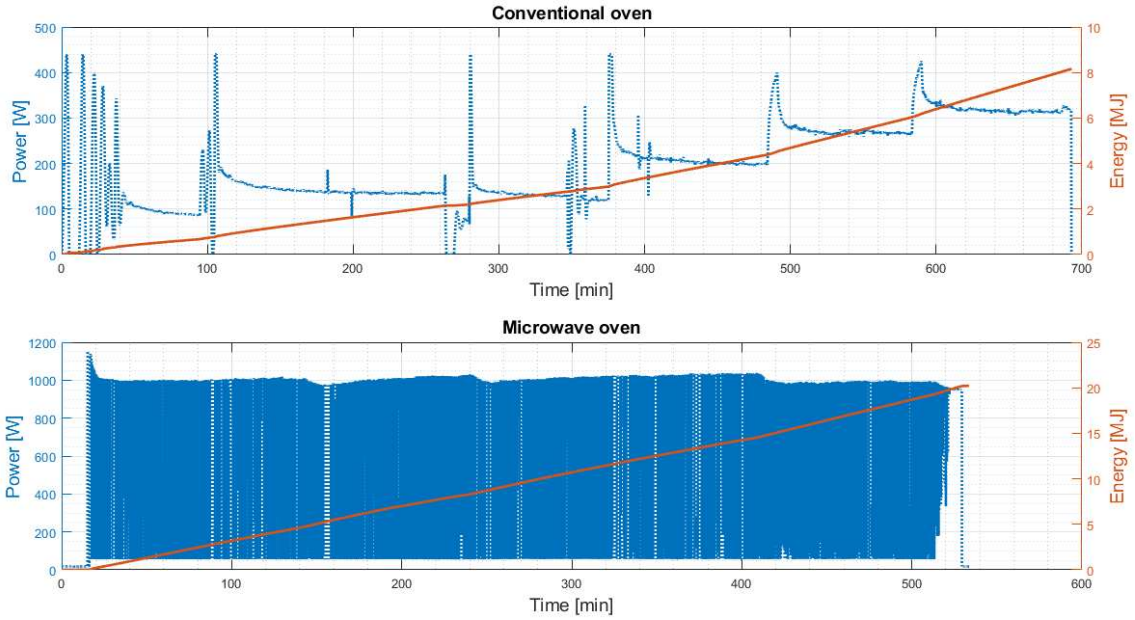

Figure 3.58: Instantaneous power and cumulated energy profiles of both tests.

From Figure 3.58 it can be noted that the instantaneous power subtracted from the grid by the microwave oven is not constant. In particular, it decreases at each set

point change, when the magnetron turns on for a longer period. As a consequence, the magnetron temperature increase; electrons colliding with the resonant cavity transform their kinetic energy in thermal energy, which increase the magnetron temperature. It is necessary to accurately control the magnetron temperature during the test, as to avoid the activation of the safety thermal switch, which would result in a interruption of the test. As the magnetron temperature increases, the instantaneous power subtracted by the oven from the electric grid increases, as shown by Figure 3.59.

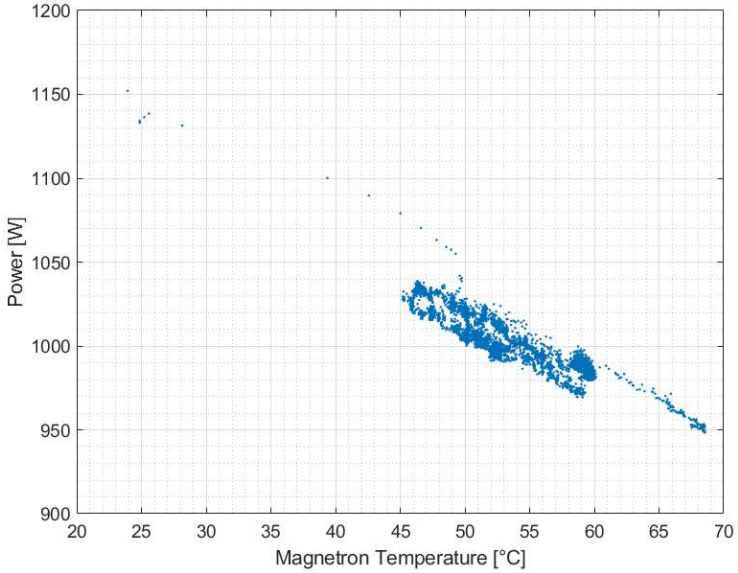

Figure 3.59: Relation between magnetron temperature and instantaneous power.

Final considerations on the system's performances

From the results exposed in the previous paragraphs, it is clear that the conventional heating system shows better performances in terms nearly all aspects: reactant conversions, products selectivity, Hydrogen production, and power consumption. However, it must be noted that the MW heating system was not insulated, thus, heat losses may play a central role in the temperature distribution of the bed, resulting in inhomogeneous reaction rates. Moreover, the uncertainty related to the theorised presence of non-thermal MW effects may play a role in the systems performances. The effect that MW radiation have on chemical reactions is still not well understood, due to the uncertainties related to temperature monitoring. The conventional heating system is characterised by a well defined temperature distribution, which lead to lower temperatures at the reactor's centre; the problem of inhomogeneous temperature distribution is however more relevant under MW heating, where the temperature profile of the bed change both axially and radially, and is not constant through time.

Conclusions

This thesis work was focused on the implementation of MW heating technology for a highly endothermic reaction, the Methane Dry Reforming; by means of this reaction, Methane and Carbon Dioxide (two of the most important greenhouse gasses) are converted into Syngas. The actual Syngas production processes are based on conventional heating systems, that is, heating is achieved through combustion of fossil fuels. Microwave heating, instead, is based on usage of electrical energy, which does not require fossil fuels, and may be integrated with more sustainable energy sources. This thesis work explored three main aspects of microwave heating; a reliable method for temperature measurements and control, the development of a suitable MW reactor for achieving heating in the MDR reaction, and the MDR performance analysis of the developed MW heating system compared to the conventional heating system.

Temperature measurement under MW radiation represents a fundamental obstacle to obtain a large-scale implementation of the MW heating technology. Three temperature measurement strategies were analysed: the use of air thermometers, non-contact methods and thermocouples. The possibility of using air thermometers and non-contact methods was discarded, due to the limitation related to heat losses and thermal inertia in the first case, and the impossibility of measuring the reactor internal temperature, since only the external temperature of the reactor can be measured with optical methods. Thermocouples resulted the most reliable temperature measurement method, given that a series of precautions are taken. The presence of metallic thermocouples may give rise to different physical phenomena which results in wrong temperature measurements. In particular, the effects are related to intensification of the electric field at the thermocouple tip, thermal conduction away from the sample, dielectric breakdown of the atmosphere and heating of the thermocouple due to the Joule effect. The impact of all these effects was investigated in this work; it was concluded that, for the setup in use, their effect could be negligible or minimised. Thus, it was determined that metallic thermocouples may be implemented under MW heating, provided that (i) the thermocouple tip is positioned into an highly dielectric lossy medium, to minimise interactions between the internal thermocouple circuit and the external electromagnetic field, (ii) the thermocouple is grounded, to avoid accumulation of charges in the bed, which may result in a voltage build-up that induces electric discharges in the bed. It must be underlined, however, that a huge impact on this analysis is given by the dielectric characteristics of the absorber material (SiC); in absence of precise estimations of the variations of the dielectric properties with both temperature and frequency, analyses will be

based on labile foundation.

Concerning the development of the experimental setup, different aspects were considered. First, the thermocouple diameter plays a central role, due to the possibility of avoiding electric discharges in the fixed bed; charge accumulation in the thermocouple tip, where the probe curvature is lower, may lead to significant electric field enhancement, which may results in dielectric breakage, that is, electric discharges. Implementing thermocouples having large diameters (1/8 in) contributes to reducing this effect, reducing the possibility of generating electric discharges in the catalytic bed. The particle size of the MW absorber implemented in the setup (*Silicon Carbide*) also determines the heating capabilities of the system, and an inverse relation between particle size and heating capability was experimentally found during the tests. In particular, smaller SiC particles are less efficient in absorbing the incident MW radiation, leading to reflections of larger fractions of the incident radiation. The reflected radiation may be absorbed by the magnetron, overheating it. If a limit temperature is reached, heating may be interrupted by safety devices, leading to heating interruption or, if heating is not controlled, magnetron breakage. An inherent problem of multi-mode MW applicators is the inhomogeneous temperature distribution in the bed, which determine the presence of axial temperature gradients. The temperature distribution in the catalytic bed changes both in space and time, depending on the instantaneous distribution of the electric field. Due to the variation of the SiC dielectric properties with temperature, depending on the local SiC temperature inside the bed, the fraction of absorbed radiation changes. This lead to variations in the material capabilities of reflecting MW, which in turn affects the instantaneous distribution of the electric field in the cavity, contributing to the randomness of electric field distribution. This lead to instability of the temperature profiles in the bed, which changes in space, time and in relation to the average bed temperature. A fundamental improvement required to achieve industrial application of the MW heating technology with multimode applicators is related to the homogenization of the temperature field, by concentrating the EM field in a lower volume than the one of the cavity. Impedance matching calculations must be developed to optimize the power transmission from the magnetron to the load, thereby reducing the reflected waves; in fact, efficiency of power transmission between magnetron and the catalytic bed is determined by the amount of dielectric material present into the cavity oven. The catalyst used in this work is an industrial one, characterised by high resistance to deterioration phenomena. However, the effect of MW heating on those type of catalyst has to be investigated in depth, due to the possible presence of localised temperature increments related to the formation of hot spots in the catalytic bed. An effect that has to be carefully examined under MW heating is the generation of electric currents in the bed; those may lead to electric discharge between the metallic particles, thereby generating plasma, which may lead to unforeseen consequences on the reaction performances, the catalyst integrity and the apparatus safety. This effect is related to the amount of metallic catalyst present in the catalytic bed. To reduce the possibility of excessive charge accumulation, which may result in dielectric breakage (formation of electric discharges), the catalyst was diluted with SiC in a mixture containing 80% of Silicon Carbide (not susceptible

to this phenomenon). This dilution resulted in generation of a low voltage, thus low possibility of observing electric discharges. Another issue that must be considered is related to the instantaneous power drops related to the magnetron activation, which may affect the electrical instrument's performances, if those are connected to the same electric grid. In particular, this effect influences the set point value of mass flowmeters, which are connected to the same electrical line. This result in variations of the set point of the flowmeters, thus the mixture delivered by the instruments is subject to instantaneous variations, which takes place at each on/off magnetron cycle. To avoid this issue, a free volume was added before the reactor inlet. The reactor position has to be optimised in order to place it in the position of maximum intensity of the EM field, with the developed configuration. To maximise power transmission, the catalytic bed was placed at the same height of the waveguide, since experiments showed that in this position the bed is rapidly heated. However, the electric field distribution changes with the position of the load in the cavity (and with its temperature); thus, an in-depth study has to be performed to determine the most suitable position of the catalytic bed in the oven cavity, also in relation with the catalyst load.

The conventional heating system seems to perform better in MDR, if compared to the MW heating system. All the performance indices indicate that the MW oven has to be optimised to become competitive with conventional heating methods. Methane conversion at 500°C, 600°C, 700°C and 800°C is 10% higher under conventional heating than MW heating; at 900°C instead, under MW heating it is higher, reaching 83% while in the conventional oven it approaches 75%. Carbon Dioxide conversion is also higher under conventional heating at 500°C, 600°C and 700°C, while for 800°C conversion in MW heating is higher, approaching nearly 100% at 900°C, a value above the equilibrium value.
Selectivity toward Hydrogen is higher in conventional heating, implying that more Hydrogen is produced than in the MW heating system. Values of selectivity different from unity indicate the presence of secondary reactions; these reactions are reduced at higher temperatures, where selectivity approaches one. Under MW heating, selectivity approaches unity at high methane conversions. Differences in selectivity between the two heating systems may be determined by a purely thermal effect, which may be traced back to the highly inhomogeneous temperature distribution in the catalytic be under MW heating. However, different selectivity may be determined by the effect that the electromagnetic field have on reactions; this subject is still unclear. Heat losses from the catalytic bed under MW heating may have played a fundamental role in lowering the MW heating system performances; in this case, insulation was not applied to visually inspect for electric discharges inside the bed; clearly, this fact determined an important dissipation of heat from the catalytic bed to the oven cavity. This effect is not present in the conventional heating system, where 5 cm of ceramic insulation were present. In addition, it must be noted that a systematic optimization performed on all the parameters may lead to huge improvements in its performances.

Bibliography

[1] Ammonia plant performance - world class catalysts, absorbents and services for ammonia production.

[2] Microwave oven radiation, https://www.fda.gov/radiation-emitting-products/resources-you-radiation-emitting-products/microwave-oven-radiation.

[3] R.J. Meredith A.C. Metaxas. *Industrial Microwave Heating*.

[4] Nabil Majd Alawi, Gia Hung Pham, Ahmed Barifcani, Minh Hoang Nguyen, and Shaomin Liu. Syngas formation by dry and steam reforming of methane using microwave plasma technology. In *IOP Conference Series: Materials Science and Engineering*, volume 579, page 012022. IOP Publishing, 2019.

[5] Suresh C Ameta, Pinki B Punjabi, Rakshit Ameta, and Chetna Ameta. *Microwave-assisted organic synthesis: a green chemical approach*. CRC Press, 2014.

[6] Thoria A Baeraky. Microwave measurements of the dielectric properties of silicon carbide at high temperature. *Egypt. J. Sol*, 25(2):263–273, 2002.

[7] Xian-jun Bi, Pin-jie Hong, Xiao-guang Xie, and Shu-shan Dai. Microwave effect on partial oxidation of methane to syngas. *Reaction Kinetics and Catalysis Letters*, 66(2):381–386, 1999.

[8] Sujith Bobba, Z Leman, ES Zainudin, and SM Sapuan. Hoop tensile strength behaviour between different thicknesses e-glass and s-glass frp rings. *AIMS Materials Science*, 6(3):315–327, 2019.

[9] G Bond, RB Moyes, SD Pollington, and DA Whan. Measurement of temperature during microwave heating (chemical reactions enhancement). *Measurement Science and Technology*, 2(6):571, 1991.

[10] Gro Harlem Brundtland. Our common future—call for action. *Environmental Conservation*, 14(4):291–294, 1987.

[11] James H Clark and Duncan J Macquarrie. *Handbook of green chemistry and technology*. John Wiley & Sons, 2008.

[12] Wm Curtis Conner and Geoffrey A Tompsett. How could and do microwaves influence chemistry at interfaces? *The Journal of Physical Chemistry B*, 112(7):2110–2118, 2008.

[13] Dariusz Czylkowski, Bartosz Hrycak, Mariusz Jasiński, Mirosław Dors, and Jerzy Mizeraczyk. Microwave plasma-based method of hydrogen production via combined steam reforming of methane. *Energy*, 113:653–661, 2016.

[14] Ignacio de Dios García, Andrzej Stankiewicz, and Hakan Nigar. Syngas production via microwave-assisted dry reforming of methane. *Catalysis Today*, 362:72–80, 2021.

[15] Antonio de la Hoz, Angel Diaz-Ortiz, and Andres Moreno. Microwaves in organic synthesis. thermal and non-thermal microwave effects. *Chemical Society Reviews*, 34(2):164–178, 2005.

[16] Tomasz Durka, Georgios D Stefanidis, Tom Van Gerven, and Andrzej I Stankiewicz. Microwave-activated methanol steam reforming for hydrogen production. *International Journal of Hydrogen Energy*, 36(20):12843–12852, 2011.

[17] Tomasz Durka, Tom Van Gerven, and Andrzej Stankiewicz. Microwaves in heterogeneous gas-phase catalysis: experimental and numerical approaches. *Chemical Engineering & Technology: Industrial Chemistry-Plant Equipment-Process Engineering-Biotechnology*, 32(9):1301–1312, 2009.

[18] Paccanaro F. *Simulazione di un reattore a microonde per reforming di Gas Naturale con vapore*. Tesi di laurea in Ingegneria chimica e dei Processi Industriali, DII, Università di Padova, 2015-2016.

[19] Beatriz Fidalgo, A Domínguez, JJ Pis, and JA Menéndez. Microwave-assisted dry reforming of methane. *International Journal of Hydrogen Energy*, 33(16):4337–4344, 2008.

[20] Gabriella Garbarino, Federico Pugliese, Tullio Cavattoni, Paola Costamagna, et al. A study on co2 methanation and steam methane reforming over commercial ni/calcium aluminate catalysts. *Energies*, 13(11):2792, 2020.

[21] Manoj Gupta and Eugene Wong Wai Leong. *Microwaves and metals*. John Wiley & Sons, 2008.

[22] Sepehr Hamzehlouia. Development of microwave heating-assisted catalytic reaction process: Application for dry reforming of methane optimization. 2017.

[23] Sepehr Hamzehlouia, Shaffiq A Jaffer, and Jamal Chaouki. Microwave heating-assisted catalytic dry reforming of methane to syngas. *Scientific reports*, 8(1):1–7, 2018.

[24] Sepehr Hamzehlouia, Jaber Shabanian, Mohammad Latifi, and Jamal Chaouki. Effect of microwave heating on the performance of catalytic oxidation of n-butane in a gas-solid fluidized bed reactor. *Chemical Engineering Science*, 192:1177–1188, 2018.

[25] William M Haynes. *CRC handbook of chemistry and physics*. CRC press, 2014.

[26] Satoshi Horikoshi, Robert F Schiffmann, Jun Fukushima, and Nick Serpone. Microwave chemical and materials processing. *Springer*, 2018.

[27] RM Hutcheon, MS De Jong, FP Adams, PG Lucuta, JE McGregor, and L Bahen. Rf and microwave dielectric measurements to 1400° c and dielectric loss mechanisms. *MRS Online Proceedings Library (OPL)*, 269, 1992.

[28] Frank P Incropera, David P DeWitt, Theodore L Bergman, Adrienne S Lavine, et al. *Fundamentals of heat and mass transfer*, volume 6. Wiley New York, 1996.

[29] J Jacob, LHL Chia, and FYC Boey. Thermal and non-thermal interaction of microwave radiation with materials. *Journal of materials science*, 30(21):5321–5327, 1995.

[30] Zirui Jia, Kejun Lin, Guanglei Wu, Hui Xing, and Hongjing Wu. Recent progresses of high-temperature microwave-absorbing materials. *Nano*, 13(06):1830005, 2018.

[31] C Oliver Kappe, Alexander Stadler, and Doris Dallinger. *Microwaves in organic and medicinal chemistry*, volume 52. John Wiley & Sons, 2012.

[32] HN Kritikos, KR Poster, and HP Schwan. Temperature profiles in spheres due to electromagnetic heating. *Journal of Microwave power*, 16(3):327–344, 1981.

[33] Antonio de la Hoz, Angel Díaz-Ortiz, and Andres Moreno. Review on non-thermal effects of microwave irradiation in organic synthesis. *Journal of Microwave Power and Electromagnetic Energy*, 41(1):45–66, 2006.

[34] Alessandra Lorenzetti. *Slide del corso "Processi Chimici Innovativi"*. DII, Università di Padova, 2019.

[35] Guiotto M. *Studi cinetici su catalizzatori three-ways commerciali e alternativi per emissioni da motori a combustione interna*. Tesi di laurea in Ingegneria chimica e dei Processi Industriali, DII, Università di Padova, 2014.

[36] James O Maloney. *Perry Chemical Engineers Handbook*. The McGraw-Hill Companies, Inc, 2008.

[37] Eugenio Meloni, Marco Martino, Antonio Ricca, and Vincenzo Palma. Ultracompact methane steam reforming reactor based on microwaves susceptible structured catalysts for distributed hydrogen production. *International Journal of Hydrogen Energy*, 46(26):13729–13747, 2021.

[38] Roger J Meredith. *Engineers' handbook of industrial microwave heating*. Number 25. Iet, 1998.

[39] AC Metaxas, , and Roger J Meredith. *Industrial microwave heating*. Number 4. IET, 1983.

[40] Hoang M Nguyen, Jaka Sunarso, Claudia Li, Gia Hung Pham, Chi Phan, and Shaomin Liu. Microwave-assisted catalytic methane reforming: a review. *Applied Catalysis A: General*, 599:117620, 2020.

[41] M Khoshtinat Nikoo and NAS Amin. Thermodynamic analysis of carbon dioxide reforming of methane in view of solid carbon formation. *Fuel Processing Technology*, 92(3):678–691, 2011.

[42] Mohammad Ostadi, Erling Rytter, and Magne Hillestad. Boosting carbon efficiency of the biomass to liquid process with hydrogen from power: The effect of h2/co ratio to the fischer-tropsch reactors on the production and power consumption. *Biomass and Bioenergy*, 127:105282, 2019.

[43] Bonato P. *Reforming di metano con vapore in reattore a microonde: progettazione, realizzazione e prove preliminari*. Tesi di laurea in Ingegneria chimica e dei Processi Industriali, DII, Università di Padova, 2015.

[44] Vincenzo Palma, Daniela Barba, Marta Cortese, Marco Martino, Simona Renda, and Eugenio Meloni. Microwaves and heterogeneous catalysis: A review on selected catalytic processes. *Catalysts*, 10(2):246, 2020.

[45] Zhiwei Peng, Jiann-Yang Hwang, and Matthew Andriese. Design of double-layer ceramic absorbers for microwave heating. *Ceramics International*, 39(6):6721–6725, 2013.

[46] Robert H Perry, Don W Green, and JO Maloney. Perry's chemical engineers' handbook (ed.). *Seventh, International edition*, 1997.

[47] Evan Pert, Yuval Carmel, Amikam Birnboim, Tayo Olorunyolemi, David Gershon, Jeff Calame, Isabel K Lloyd, and Otto C Wilson. Temperature measurements during microwave processing: the significance of thermocouple effects. *Journal of the American Ceramic Society*, 84(9):1981–1986, 2001.

[48] David M Pozar. *Microwave engineering*. John wiley & sons, 2011.

[49] Adrian Ramirez, José L Hueso, M Abian, MU Alzueta, Reyes Mallada, and Jesús Santamaría. Escaping undesired gas-phase chemistry: Microwave-driven selectivity enhancement in heterogeneous catalytic reactors. *Science advances*, 5(3):eaau9000, 2019.

[50] Koichi Sato, Hongyan Luo, Masato Miyakawa, and Masateru Nishioka. Reforming of methane using single-mode microwave irradiation heating in a cylindrical cavity. *Journal of the Japan Petroleum Institute*, 63(5):315–321, 2020.

[51] Seyyedmajid Sharifvaghefi, Babak Shirani, Mladen Eic, and Ying Zheng. Application of microwave in hydrogen production from methane dry reforming: comparison between the conventional and microwave-assisted catalytic reforming on improving the energy efficiency. *Catalysts*, 9(7):618, 2019.

[52] Andrzej Stankiewicz, Farnaz Eghbal Sarabi, Abdul Baubaid, Peng Yan, and Hakan Nigar. Perspectives of microwaves-enhanced heterogeneous catalytic gas-phase processes in flow systems. *The Chemical Record*, 19(1):40–50, 2019.

[53] Georgios D Stefanidis, Alexander Navarrete Munoz, Guido SJ Sturm, and Andrzej Stankiewicz. A helicopter view of microwave application to chemical processes: reactions, separations, and equipment concepts. *Reviews in Chemical Engineering*, 30(3):233–259, 2014.

[54] Julius Adams Stratton. *Electromagnetic theory*, volume 33. John Wiley & Sons, 2007.

[55] DAC Stuerga and P Gaillard. Microwave athermal effects in chemistry: A myth's autopsy: Part i: Historical background and fundamentals of wave-matter interaction. *Journal of microwave power and electromagnetic energy*, 31(2):87–100, 1996.

[56] H Sugawara, K Kashimura, M Hayashi, S Ishihara, T Mitani, and N Shinohara. Behavior of microwave-heated silicon carbide particles at frequencies of 2.0–13.5 ghz. *Applied Physics Letters*, 105(3):034103, 2014.

[57] C Thies. Kirk-othmer encyclopedia of chemical technology, vol. 16, 1995.

[58] Tom Van Gerven and Andrzej Stankiewicz. Structure, energy, synergy, time. the fundamentals of process intensification. *Industrial & engineering chemistry research*, 48(5):2465–2474, 2009.

[59] B Vos, J Mosman, Y Zhang, E Poels, and A Bliek. Impregnated carbon as a susceptor material for low loss oxides in dielectric heating. *Journal of materials science*, 38(1):173–182, 2003.

[60] JKS Wan. Microwaves and chemistry: The catalysis of an exciting marriage. *Research on chemical intermediates*, 19(2):147–158, 1993.

[61] Niandu Wu, Xianguo Liu, Chengyun Zhao, Caiyun Cui, and Ailin Xia. Effects of particle size on the magnetic and microwave absorption properties of carbon-coated nickel nanocapsules. *Journal of Alloys and Compounds*, 656:628–634, 2016.

[62] Hui-Jing Yang, Jie Yuan, Yong Li, Zhi-Ling Hou, Hai-Bo Jin, Xiao-Yong Fang, and Mao-Sheng Cao. Silicon carbide powders: temperature-dependent dielectric properties and enhanced microwave absorption at gigahertz range. *Solid state communications*, 163:1–6, 2013.

[63] Xunli Zhang, David O Hayward, Colleen Lee, and D Michael P Mingos. Microwave assisted catalytic reduction of sulfur dioxide with methane over mos2 catalysts. *Applied Catalysis B: Environmental*, 33(2):137–148, 2001.

[64] Xunli Zhang, Colleen S-M Lee, D Michael P Mingos, and David O Hayward. Carbon dioxide reforming of methane with pt catalysts using microwave dielectric heating. *Catalysis letters*, 88(3):129–139, 2003.

Ringraziamenti

Al termine di questo percorso trovo doveroso scrivere alcune semplici righe per ringraziare chi mi ha permesso di raggiungere questo importante traguardo. In cima alla lunga lista, che risulterà sicuramente incompleta, meritano di stare le due figure che più di tutte mi hanno sostenuto in questa avventura, guidandomi con i loro lungimiranti e preziosi consigli, permettendomi di vivere appieno questa esperienza, e non solo dal punto di vista economico: i miei genitori, Roberto e Maria Adele. A loro devo la mia passione per la conoscenza, la curiosità, la tenacia che mi ha sempre contraddistinto ed il carattere testardo; il sostegno loro continuo nei momenti più impegnativi è stato fondamentale per poter arrivare qui. Ringrazio Martina, Matteo e Carlo, perchè senza di loro non avrei avuto i fondamentali sostegni sui quali contare, anche solo per un sorriso o una parola gentile. Li ringrazio perchè se c'è un posto che chiamo "casa", questo posto è dove lì si trovano loro. Ringrazio per la sapiente, cortese e gentile disponibilità il Professor Canu. Come potrei non includere nella lista anche Mattia e Marco, sempre disponibili per un chiarimento, un caffè, o per una chiacchiera, ma anche altrettanto disponibili per una corsa in ospedale. Ringrazio Nicola per il prezioso contributo nello sciogliere alcuni nodi fondamentali incontrati durante la tesi, e più in generale il gruppo di K-INN Tech. Un pensiero lo dedico anche a tutti i miei amici, lontani e vicini, sia nel tempo che nello spazio, per essere stati al mio fianco, incondizionatamente. Ringraziarli uno per uno richiederebbe altre decine di pagine, ma voglio ringraziare in particolare Giorgio, Francesco, Samuele, Alessandro e Stefano, perchè con loro ho condiviso tutti i migliori momenti. Ringrazio Marco, perchè si ostina ad essermi vicino da quando ne ho memoria. Ringrazio Cristiana, per le sue parole sempre gentili: grazie per avermi fatto conoscere più a fondo, ti devo tanto. Ringrazio Zia Annalisa e Zio Mauro, perchè senza di loro non potrei essere la persona che sono diventato. Grazie anche a Zia Bianca e Zio Benedetto, perchè anche da loro una parola gentile, una carezza o una battuta non sono mai mancate. Un pensiero va anche a tutte le persone con i quali ho condiviso casa e che mi hanno fatto sentire a casa, anche quando la mia casa era a centinaia di chilometri di distanza. Infine, ringrazio tutti i compagni di corso, per aver reso più leggero e divertente imparare insieme.